The Flow of Poynting Flux into the Terrestrial Cusp and Auroral Zone and Its Role in Powering Energy Intensive Collisionless Acceleration Mechanisms

A DISSERTATION
SUBMITTED TO THE FACULTY OF THE GRADUATE SCHOOL
OF THE UNIVERSITY OF MINNESOTA
BY

Sheng Tian

IN PARTIAL FULFILLMENT OF THE REQUIREMENTS
FOR THE DEGREE OF
Doctor of Philosophy

John Wygant

December, 2017

Acknowledgments

I want to thank my wife Qianhui Shi. The years in Minnesota with her accompany are filled with precious moments. I appreciated the moment we met during the TA training program, the times when we took advanced physics courses, and discussions that were actually contributing to this thesis. Our love history is so entangled with our lives as graduate students that she is not only my wife, but also my friend, soul mate and physics colleague/teacher.

I also want to thank my parents. There is a Chinese proverb: Give a man a fish and you feed him for a day; teach a man to fish and you feed him for a lifetime. My parents are experts in teaching fishing. Under their influence, curiosity grows in me and I self taught myself a lot of things: fine art, programming, web page design, just to name a few. I started to develop a broad interests in life and in physics. I am grateful on their efforts in my education.

I would like to thank my adviser John Wygant for his excellent guidance on various topics in space physics, and on the data processing of various spacecraft missions, including Polar, FAST, RBSP, Image, THEMIS. He had created a comfort environment that I could explore my research interests and sometimes deviate on technique development. I enjoyed every talk or discussion with him, since he has a broad knowledge on various topics in space physics and he is expert in explaining things in the simplest way.

There are special thanks for Mary Crawford. Thank you for the care and supports when I lived in your house. It was like a family and a very valuable memory in my life.

I am very grateful for the help from my co-workers and professors (in alphabetical order): Aaron Breneman, Cynthia Cattell, Chris Cholpitts, Lei Dai, John Dombeck, Alex Engel, Lindsay Glesener, Keith Goetz, Alex Igl, Thomas Jones, Andreas Keiling, Paul Kellogg, Naiguo Lin, Robert Lysak, Steve Menson, Charles McEachern, Yan Song Xiangwei Tang, Scott Thaller, Evan Tyler. There were many many moments when these talented people provide great comments and suggestions.

This thesis contains data from various instruments on-board several spacecraft missions. I would like to thank the scientists who provided the data and acknowledge the financial support by the various funding agencies.

Abstract

During geomagnetic active times, the earth's magnetosphere experiences boost in the circulation of mass and energy. The ionosphere interacts with the magnetosphere mainly in the high latitude region through the connection of the magnetic field. The dayside cusp and the nightside aurora are the two main regions of ionosphere-magnetosphere coupling. The Poynting flux, carrying the electromagnetic energy, enhances in the two regions (Keiling et al., 2003). Poynting flux may be an important contributor to energy flow in stars and planets and drive collisionless acceleration mechanisms that generate intense particle energy flux along magnetic field lines. Utilizing the abundant in-situ measurements, we study the intense earthward Poynting flux in the earth high-latitude region.

We found that in the dayside cusp, an unexpected energetic wind of ions is driven by the enhanced earthward Poynting flux. The ion outflow originated from a narrow region from the dayside cusp. Based on both case and statistical studies, we showed that the ion energization occurs in the mid-altitude cusp, well above the ionosphere where the ions are driven to upwell. Although many mechanisms on local heating and acceleration have been proposed, the energy circulation related to the energization process was rarely studied. Our findings show that the earthward Poynting flux is the only energy source for the ion energization. More than a quarter of the electromagnetic energy is converted to the kinetic energy of the ion outflow. The remaining Poynting flux continues to flow earthward and partially converted to accelerate electrons downward. The study reveals the existence of an efficiently accelerated wind of ions at the cost of electromagnetic energy, which may be

applicable to the solar wind and the powerful winds in other astrophysical objects. The identification of the free energy source as Poynting flux would place several constraints on the possible mechanisms of ion energization.

For the aurora in the nightside, people generally agree that the poleward portion of the aurora is powered by the earthward Poynting flux within the plasma sheet boundary layer (PSBL). The Alfvénic Poynting flux dissipates its electromagnetic energy at the "aurora acceleration region" to accelerate electrons, which in turn excite the aurora. In the second part of the thesis, we show a case study which, for the first time, demonstrates the direct correlation between the discrete aurora arc and the earthward Poynting flux. The electromagnetic energy carried by the Poynting flux is also partially converted to the simultaneously observed oxygen outflows originated from the nightside ionosphere. The Poynting flux is mainly earthward and carried by MHD waves. Different from the case of the cusp, most of the electromagnetic energy in the nightside is converted to accelerate electrons, only a small portion is converted to power the ion outflow. The event is also the first conjunction between the auroral westward traveling surge (WTS) and high-altitude spacecraft. Given the good correlation between the Poynting flux and aurora, it is likely that the WTS represents the perpendicular propagation of the Alfvén waves in the magnetosphere.

Contents

List of Tables

List of Figures

Chapter 1

Introduction

Poynting flux plays a major role in the energy balance within the coupled system of the ionosphere, magnetosphere and solar wind. The Polar spacecraft has statistically shown that the most intense Poynting fluxes tend to occur during geomagnetic active times and are concentrated around dayside cusp which maps to the magnetopause and the nightside auroral zone (Keiling et al., 2003). It is generally accepted that the most poleward aurora during active times is closely related to the earthward Poynting flux in the nightside. In the dayside, Strangeway et al. (2005) showed that at the ionospheric altitudes, the earthward Poynting flux, along with the precipitating electrons, can drive ion outflows within the cusp in large number flux. However, how the ion outflow is energized at higher altitudes is a different question from the mass flow but of equal importance. In this study, we report that a surprisingly energetically intensive wind can be observed in the mid-altitude cusp, which suggests that there is a second stage of ion energization in the mid-altitude, in addition to the first stage of driving ion outflows at the ionospheric altitudes. The intense wind within the cusp can carry an energy flux of several 10 mW/m^2 in the upward direction, or more than 100 mW/m^2 in extreme cases, which is as powerful as the energy flux causes the brightest aurora and much more powerful than the polar wind in the polar cap. Based on the energy budget analysis, we identify that the ion energization is powered by the earthward Poynting

flux in the mid-altitude. The Poynting flux is largely converted to energize the cusp ion outflows, and the left part flows into the ionosphere. We found an energy conversion ratio of ∼20% on average between the ion outflow and the Poynting flux, which indicates a very efficient ion energization mechanism as compared to the ratio of less 1% in the nightside. The electrons are ruled out as an energy source for the cusp ion energization. Although the electrons are important in driving the ion outflow, they gain instead of supplying energy in ion energization in the mid-altitude cusp. At low-altitude, we found that during the first stage, although the number flux of the ion outflow is high, the net energy flux of the ions are downward or close to 0, which suggests that the main energization occurs in the mid-altitude cusp. Further investigation on the Poynting flux shows that it is transmitted in the form of Alfvén waves, and maybe also the field-aligned currents.

Although the Poynting flux in the dayside is largely converted to the intense wind of ions, the situation is quite different in the nightside, where the second part of the thesis will be focusing on. Wygant et al. (2000) have shown the close connection between the earthward Poynting flux and the most poleward aurora. However, more detailed comparisons are difficult due to the limited temporal and spatial resolution of the instrumentation. In this study, we report a conjunction study between the twin RBSP spacecraft and the THEMIS ground-based aurora imager. With the an-order-of magnitude resolution improvement, we report the first observation on the direct correlation between the earthward Poynting flux and the discrete aurora in both time and location. The good correlation further implies causality since the Poynting flux was predominantly earthward and large enough to power the brightest aurora. Ion outflows of ionospheric origin were observed (though much less energetic than the cusp ion outflows) and can be explained to be powered by the Poynting flux as well. The E/B ratio suggests that the Poynting flux was mostly carried by MHD waves, in the frequency range 10 mHz - 1 Hz in the spacecraft frame. The event is also the first conjunction study on the auroral westward traveling surge (WTS) and high-altitude spacecraft. The speed of the WTS was about 15 km/s at the ionosphere, and was 130 km/s when mapped to the location

of the RBSP spacecraft. Given the good correlation between the Poynting flux and aurora, it is likely that the WTS represents the perpendicular propagation of the Alfvén waves in the magnetosphere. Other observations include a density structure propagated at 25 km/s in the westward azimuthal direction; the Poynting flux and the associated Alfvén waves were concentrated at strong density gradients around the PSBL. The density structures may be carried by a slow plasma flow since it is consistent with typical flow velocities in the inner-magnetosphere. Flow braking may be evidenced by the fact that the density structure was broader at RBSP-B than at RBSP-A. The association between the Poynting flux and the density gradient may imply that the waves are generated through phase mixing/mode conversion from the compressional mode due to the flow braking. However, the validity of these conjectures needs to be checked in further observations.

The thesis is organized into the following chapters. Chapter 2 will list the major spacecraft missions and instrumentation used in the studies. The observational results in the dayside cusp are presented in Chapter 3. We will report two quasi-conjunction events between the Polar spacecraft in the mid-altitude cusp and the FAST spacecraft in low-altitude. A statistical study on 4 years of Polar and FAST cusp crossings is presented afterward and confirms that the results in the case studies are repetitive. Chapter 4 includes a case study on the conjunction between the RBSP spacecraft and the THEMIS ground-based aurora observation. Chapter 5 summarizes the main results and conclusions. In the rest of this chapter, we will briefly introduce the related space plasma regions as a general background knowledge in Section 1.1. Section 1.2 briefly summarizes the basics theories on Alfvén waves and the Poynting's theorem. They are used in determining wave modes and the energy balance analysis in the cusp and auroral zone studies.

1.1 Relevant Space Plasma Regions

We mainly focus on the high-latitude ionosphere and the associated regions that are magnetically conjugate. By high-latitude ionosphere, we refer to the regions around the northern

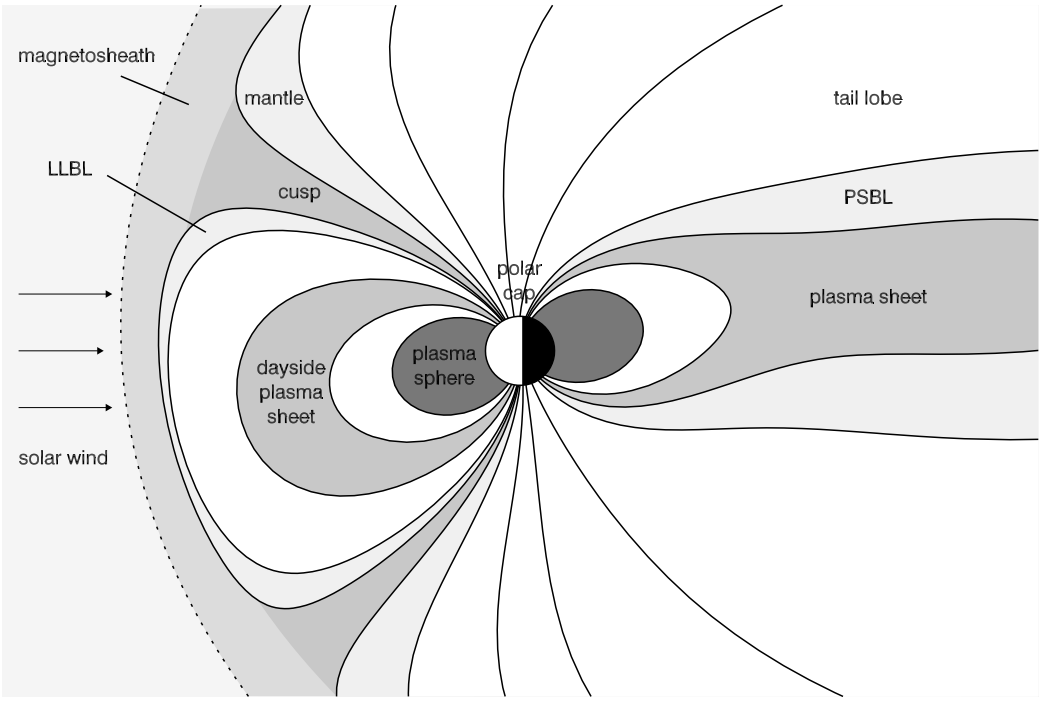

Figure 1.1: A side view of the solar wind and the regions in the magnetosphere.

	Regions	n_e (cm^{-3})	T_e	B (nT)
Nightside (> 8 Re)	Tail lobe	0.01	50 eV	50
	Plasma sheet	1-10	10 keV	0-10
	PSBL	5	1 keV	20
Dayside (> 3 Re)	Cusp	10	1 keV	<500
	LLBL/Mantle	1	500 eV	<500
	Plasma sheet	1	10 keV	50
Outside Magnetosphere	Magnetosheath	10	100 eV	100
	Solar wind	5	10 eV	10

Table 1.1: Plasma regions and the characteristic parameters.

and southern poles above $\sim 60^\circ$ magnetic latitude (Figure 1.1). The related plasma populations/regions are:

- In the dayside: solar wind, magnetosheath, low-latitude boundary layer (LLBL), cusp, and dayside plasma sheet;
- In the nightside: tail lobe, nightside plasma sheet and plasma sheet boundary layer (PSBL).

We will introduce the basic plasma properties of these regions and the observational signatures in ground or in-situ measurements.

A different perspective on these regions is shown in Figure 1.2, where they are mapped to the ionosphere along magnetic field lines. The polar cap serves as a natural separator to the dayside and nightside structures/regions. As shown in Figure 1.1, the ionospheric plasma in the polar cap is "open" to the interplanetary plasma. The convention is to refer to the ionospheric part as the polar cap and the magnetospheric part as the tail lobe.

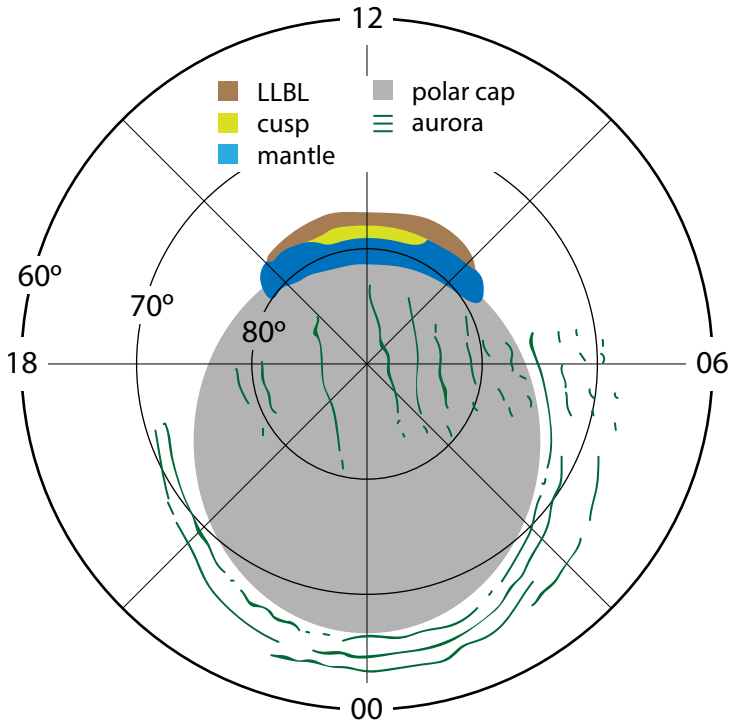

Figure 1.2: Structures/regions mapped to the ionosphere, based on figures for dayside results from Newell and Meng (1994) and nightside aurora from Akasofu (1964).

1.1.1 Solar Wind and Dayside Magnetosphere

The dayside magnetopause is a key region of the magnetosphere. The reconnection around the nose of the magnetosphere efficiently transports energy, momentum and mass to the magnetosphere (Dungey, 1961). As a result of the transport processes, direct entry of the solar wind and magnetosheath plasmas is seen in the cusp (Heikkila and Winningham, 1971; Frank, 1971), and a mixture of plasmas from the magnetosheath and magnetosphere is seen in the low-latitude boundary layer (LLBL) (Eastman et al., 1976). In this paper, we only focus on the cusp region, which maps to the magnetopause. The indirect entry that maps to the LLBL is referred to as cleft (Newell and Meng, 1988) and is not considered. The cusp plasmas are continuously dragged anti-sunward by the solar wind. These plasmas form the mantle, which is an extension of the cusp beyond the cusp/polar cap boundary.

Figure 1.3 shows one classical observation of the cusp and mantle from a low-altitude spacecraft DMSP (Newell and Meng, 1988). The spacecraft moved from high latitude to low latitude, sampling the polar cap, cusp, cleft, and dayside plasma sheet. The common cusp feature is the energy-latitude dispersion due to the velocity filtering effect (e.g. Lockwood et al., 1985b). In the case of magnetopause reconnection (Figure 1.4), low energy ions are carried further into the polar cap by the anti-sunward convection. The cusp is determined through the highest flux in the ion spectrogram. The cleft is equatorward to the cusp and is characterized by the smaller flux in the ion spectrogram, and the higher energy in both the ion and electron spectrograms. Up to the geocentric distance of about 6 Re, the cusp ion dispersions are qualitatively similar to the one shown in Figure 1.3.

However, the dispersion is due to convection but provides no information on the flow direction. In this paper, we show that intense cusp ion outflows between several 100 eV to several keV are observed in the mid-altitude cusp (3-6 Re) during active times. To simplify the discussion, we will consider events during southward IMF (interplanetary magnetic field), when the normal ion dispersion is created due to the magnetopause reconnection and anti-sunward convection 1.4. The location of the cusp is mainly affected by the solar wind

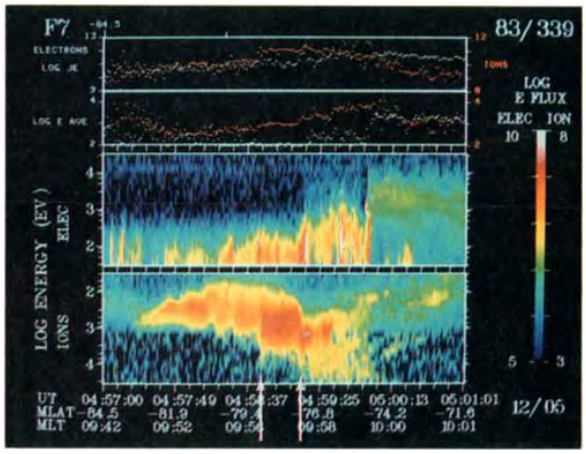

Figure 1.3: Dayside structures observed by DMSP. From Newell and Meng (1988). We will only focus on the last two panels, which are the electron and ion energy-time spectrograms. The ion spectrogram is reversed in energy (y-axis).

condition. The cusp moves to lower latitudes during geomagnetic active periods (Meng, 1982), as low as 60 deg invariant latitude in extreme cases. The cusp can also move in local time, which is controlled by the IMF B_y (Crooker et al., 1987). A positive IMF B_y shifts the reconnection site dawnward and so is the cusp observed to move accordingly. In this study, we will consider events when IMF B_y is smaller than B_z to ensure that the cusp is around the local noon.

1.1.2 Nightside Magnetosphere

The nightside magnetosphere is where the energy stored in the magnetotail is released to the ionosphere and near-earth region. Tracing upward from the aurora oval in the ionosphere are the plasma sheet and the plasma sheet boundary layer (PSBL). As shown in Figure 1.1, the inner boundary of the plasma sheet follows the magnetic field line and is usually located between 6-10 Re at the equatorial plane. And the thickness of the plasma sheet is on the order of 1-2 Re within 10-20 Re geocentric distance. The PSBL is a spatial structure with frequent temporal variations between the plasma sheet and the tail lobe (Eastman et al., 1984). In terms of observation, the tail lobe and the PSBL can be well distinguished by a

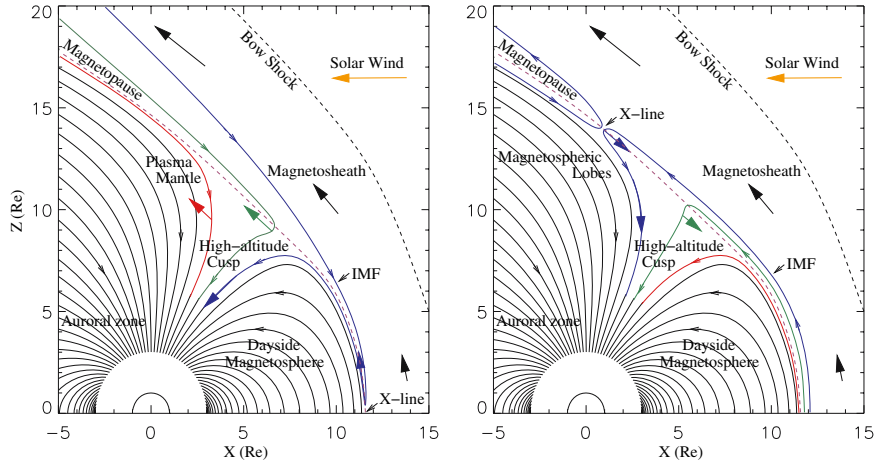

Figure 1.4: A schematic overview of the magnetopause reconnection (left) and the lobe reconnection (right). The arrows marks the plasma flows. The electric field lines are colored to indicate the history: from old to new are red, green, and purple. From Lavraud and Cargill (2005).

sharp jump in density. The plasma sheet contains hotter plasma than the PSBL. Another difference is that PSBL usually contains counter-streaming ions, which are not frequently present in the plasma sheet. The plasma sheet is in general of high β, while the PSBL and tail lobe are of low β. The typical plasma parameters of these regions are listed in Table 1.1.

Energy is poured into the magnetosphere mainly in the dayside magnetosphere and transported/stored in the magnetotail. The stored energy is released quasi-periodically through some instabilities . Such energy releases lead to various phenomena which are summarized by the term "substorms", and manifest themselves in the ionosphere as the "auroral substorms".

1.2 Alfvén Waves and the Poynting's Theorem

The paper mainly focuses on the low frequency waves in the frequency range of 1 mHz to 1 Hz, within which the MHD Alfvén wave propagates. A special property of the MHD waves

is they are efficient in radiating the electromagnetic energy in the form of Poynting flux. Waves at higher frequencies are easily dissipated locally to due to resonances with the local plasma. Waves at lower frequencies usually contain little power in the electric field and therefore do not carry much Poynting flux. In this section, we briefly summarize the theory on the Alfvén wave and the Poynting's theorem, which provides the background knowledge for the observations in later chapters. The main results are based on the notes by Professor Robert L. Lysak for the plasma physics course (2011), as well as books by Jackson (1999); Bellan (2008); Baumjohann and Treumann (1997).

We follow the order from MHD to kinetic theory. In all the sections in this chapter, we assume that the background magnetic field $\boldsymbol{B}$ is along the z direction $\boldsymbol{B} = (0, 0, B)$, and the wave vector $\boldsymbol{k}$ is in the $y - z$ plane $\boldsymbol{k} = \left(0, k_\perp, k_\parallel\right)$. The angle between $\boldsymbol{B}$ and $\boldsymbol{k}$ is θ.

1.2.1 MHD Waves

In the low frequency limit, plasma waves collapse into the MHD waves in either cold or warm plasma. The term cold or warm is related to the plasma $\beta = nkT/\left(B^2/2\mu_0\right)$ but not absolute temperature. A cold plasma is of low β, where the electromagnetic energy is much larger than the plasma's thermal energy. In this case, the background field is rigid and organizes the plasma geometry. On the other hand, a warm plasma has $\beta \gtrsim 1$, when the plasma is energetic enough to drag the field lines around. For the plasma regions of interest in this study, the plasma in the plasma sheet boundary layer within 6 Re is cold due to the high background B. The cusp plasma is also cold bellow 6 Re geocentric distance.

MHD Wave in Cold Plasmas The cold plasma, where the pressure term is assumed to be 0, supports two modes: the shear mode where

$$\omega = v_A k_\parallel = v_A k \cos\theta. \tag{1.1}$$

and the compressional mode (fast mode)

$$\omega = v_A k. \tag{1.2}$$

In these modes, the perpendicular current originates from the ion polarization drift, and the parallel current is simply assumed to follow the time stationary continuity equation $\nabla \cdot \boldsymbol{j} = 0$.

MHD Wave in Warm Plasmas In the warm limit, the pressure term which corresponds to acoustic waves is non-zero. Thus we expect acoustic speed v_a to appear in the dispersion relation. The acoustic wave only affects the compression mode, either constructively or destructively. Therefore the original compressional mode splits into two modes: the fast mode and slow mode. The shear mode is renamed to the intermediate mode. It is unaffected by the sound wave since it contains no compressional motion.

The compressional mode in the cold plasma splits into two modes (the fast and slow modes) in the warm plasma,

$$\frac{\omega^2}{k^2} = \frac{1}{2}\left[(v_a^2 + v_A^2) \pm \sqrt{v_a^4 + v_A^4 - 2v_a^2 v_A^2 \cos 2\theta}\right],$$

where the + for the fast mode and the − for the slow mode. To this point, the parallel dynamics of the compressional mode is fully resolved. The parallel dynamics in the shear mode involves the parallel electric field and parallel current, which are treated in the kinetic theory. In Section 1.2.2, we will see that the shear mode splits into kinetic Alfvén wave in the warm limit and inertial Alfvén wave in the cold limit.

Based on the dispersion relations of the MHD waves, it is clear that they have a phase velocity on the order of the local Alfvén speed v_A. This is used to identify MHD waves, since the phase velocity is the E/B ratio of the measured electric and magnetic fields. In the next section, the kinetic Alfvén waves are dispersed and have a phase velocity of several times of v_A, and therefore can be distinguished from the MHD waves.

1.2.2 Alfvén Waves in the Kinetic Theory

In the kinetic theory, the shear mode in the MHD theory gives the kinetic Alfvén wave in the warm limit and inertial Alfvén wave in the cold limit. In the context of this study, we mainly focus on the kinetic Alfvén wave since high-altitude spacecraft are usually in the warm limit.

The dispersion relation of the kinetic Alfvén wave is

$$\omega^2 = k_\parallel^2 v_A^2 \left(1 + k_\perp^2 \rho_s^2\right),$$

where $\rho_s^2 = c^2\lambda_{De}^2/v_A^2 = v_a^2/\Omega_i^2$ is the "ion acoustic gyro-radius". The Alfvén speed is increased in this case due to the warm electrons, which help the wave propagate due to a finite pressure gradient.

The dispersion relation of the inertial Alfvén wave is

$$\omega^2 = \frac{k_\parallel^2 v_A^2}{1 + k_\perp^2 c^2/\omega_{pe}^2}.$$

The Alfvén speed is decreased in this case due to the cold electrons, which provide the inertia to cancel the parallel electric field and therefore impedes the wave propagation.

1.3 The Poynting's Theorem

This section discusses the Poynting's theorem, which is used in the energy balance analysis in Chapter 3. The Poynting's theorem in medium (Equation (6.105) in Jackson (1999)) describes the wave-particle interaction

$$\boldsymbol{E} \cdot \frac{\partial \boldsymbol{D}}{\partial t} + \boldsymbol{H} \cdot \frac{\partial \boldsymbol{B}}{\partial t} + \nabla \cdot (\boldsymbol{E} \times \boldsymbol{H}) = -\boldsymbol{j}_{\text{ext}} \cdot \boldsymbol{E}.$$

Note that the current $\boldsymbol{j}_{\text{ext}}$ is the free current or external current, which will be assumed to be 0. The response of the plasma to the wave field $\boldsymbol{E}$ and $\boldsymbol{B}$ is enveloped in the dielectric tensor $\boldsymbol{\epsilon}(\omega, \boldsymbol{k})$, i.e., $\boldsymbol{D} = \boldsymbol{\epsilon} \cdot \boldsymbol{E}$. This emphasizes that the plasma is dielectric in nature. The magnetic field response is simply $\boldsymbol{H} = \boldsymbol{B}/\mu_0$ because the plasma is macroscopic so the quantum effects are negligible. In this section, we explore the meaning of the terms in the Poynting's theorem, which is non-trivial for a complex medium like plasma.

The key to understand the Poynting's theorem in a plasma medium is to consider the Joule heating which relates the wave and plasma. It can be shown that the Poynting's theorem can be re-written in the following form

$$\frac{\partial(w_E + w_B)}{\partial t} + \nabla \cdot \boldsymbol{S} = -\boldsymbol{j} \cdot \boldsymbol{E} = -\frac{\partial w_P}{\partial t} - \nabla \cdot \boldsymbol{T} + \frac{i\omega}{2} \boldsymbol{E}^* \cdot \boldsymbol{\epsilon}_A \cdot \boldsymbol{E}, \tag{1.3}$$

where $w_E = \epsilon_0 |E|^2/4$ and $w_B = |B|^2/4\mu_0$ are the electric and electromagnetic energy density, $\boldsymbol{S} = (\boldsymbol{E} \times \boldsymbol{B}^* + \boldsymbol{E}^* \times \boldsymbol{B})/4\mu_0$ is the Poynting vector or the Poynting flux, $\boldsymbol{j} = \boldsymbol{\sigma} \cdot \boldsymbol{E}$ is the internal current driven by the electric field following the conductivity $\boldsymbol{\sigma}$ determined by the dispersion relation. One the right-hand side, $w_P = \frac{1}{4} \boldsymbol{E}^* \cdot \frac{\partial(\omega \boldsymbol{\epsilon}_H)}{\partial \omega} \cdot \boldsymbol{E} - \epsilon_0 |E|^2/4$ is the plasma energy density, $\boldsymbol{T} = -\frac{1}{4} \boldsymbol{E}^* \cdot \omega \frac{\partial \boldsymbol{\epsilon}_H}{\partial \boldsymbol{k}} \cdot \boldsymbol{E}$ is the plasma kinetic energy flux, and the last term is due to the wave-particle interaction. The Hermitian dielectric tenser $\boldsymbol{\epsilon}_H = \left(\boldsymbol{\epsilon} + \boldsymbol{\epsilon}^\dagger\right)/2$ is related to the normal mode, while the anti-Hermitian dielectric tensors $\boldsymbol{\epsilon}_A = \left(\boldsymbol{\epsilon} - \boldsymbol{\epsilon}^\dagger\right)/2$ is related to wave growth or damping and depends on the local shape of $\boldsymbol{\epsilon}$ at certain ω and $\boldsymbol{k}$. For certain generic quantity $\boldsymbol{X}$, it is understood that only the normal mode obeying the dispersion relation is considered. In this case, the generic quantity can be expressed by its Fourier component

$$\boldsymbol{X}_{\omega,\boldsymbol{k}}(t, \boldsymbol{x}) = \frac{1}{2} \left(\boldsymbol{X} e^{i\boldsymbol{k}\cdot\boldsymbol{x} - i\omega t} + \boldsymbol{X}^* e^{-i\boldsymbol{k}\cdot\boldsymbol{x} + i\omega t} \right), \tag{1.4}$$

where $\boldsymbol{X}$ is a constant complex amplitude, carrying the polarization, and can be the electric

field, magnetic field, dielectric tensor, etc.

Equation (1.3) serves as the foundation for in-situ observations to identify the energy sources and sinks. In a time stationary case, the Poynting's theorem reduces to

$$\nabla \cdot \boldsymbol{S} = -\nabla \cdot \boldsymbol{T} + \frac{i\omega}{2} \boldsymbol{E}^* \cdot \boldsymbol{\epsilon}_A \cdot \boldsymbol{E}.$$

Given that the energy fluxes are usually field-aligned in cold plasma, the equation can be further simplified. Consider an integration over an Gaussian volume as in Figure 3.1, only the energy fluxes at the bottom and top cross sections need to be evaluated. The wave-particle interaction term is eliminated if the Gaussian volume is chosen to enclose the resonant interaction. Thus we have

$$\iint_{bottom} S_{\parallel} + T_{ion} + T_{ele} = \iint_{top} S_{\parallel} + T_{ion} + T_{ele}.$$

Single spacecraft crossing can measure the energy fluxes simultaneously to evaluate the relative importance. Conjunction observations at the bottom and top cross sections can identify the energy source and sink, and so do multiple crossings, which can further picture the altitude profiles of the energy fluxes.

Chapter 2

Instrumentation

This chapter briefly introduces the main spacecraft missions that are relevant to the data analysis in later chapters. The Polar and FAST data are used to study the Poynting flux in the dayside cusp region in Chapter 3 and the RBSP data are analyzed to study the Poynting flux in the nightside aurora region in Chapter 4.

2.1 Polar

The Polar spacecraft operated from February 24 1996 to April 2008. The spacecraft had a high inclination orbit of 86 deg inclination. The apogee and perigee were 1.8 and 9 Re in geocentric distance respectively. The spacecraft spun at the period of 6 sec in a cartwheel motion. The orbital period was about 17.5 hour. Such orbit allows the spacecraft to observe the high-latitude region twice per orbit at different altitudes. A full altitude coverage of the cusp from 1.8 to at least 6 Re was obtained, due to its precession (2 hr/month) and long mission duration (>10 yr). Therefore the Polar data is ideal to study the intense ion energization in the mid-altitude cusp. The relevant instruments are described briefly.

The Electric Field Instrument (EFI) (Harvey et al., 1995) measures the 3-D DC electric field at 40 samples/sec through a 20 Hz low-pass filter. The spin plane booms are about 100 m tip-to-tip and the spin axis booms are 13.8 m tip-to-tip. Thus the electric field in

the the parallel and north-south directions are more accurately measured than the east-west direction. The Magnetic Fields Experiment (MFE) (Russell et al., 1995) measures the 3-D DC magnetic field at the sample rate of 8 Hz. To calculate the Poynting flux, the electric field data were down-sampled to match the resolution of the magnetic field. The Hydra (Scudder et al., 1995) instrument measures the hot plasma from 4 eV to 20 keV per charge at a sweep resolution of 1.15 sec or a normal resolution of 13.8 sec. The energy range well covers the typical 100 eV to 1 keV cusp plasma. The instrument does not distinguish the ion species and all ions are assumed to be protons. To get the relative abundance among the ion species, the TIMAS (Toroidal Imaging Mass-Angle Spectrometer) instrument (Shelley et al., 1995)was checked in the study. The instrument covered the ion energy range of 15 eV to 32 keV per charge, which is roughly comparable to Hydra. The time resolution of TIMAS was 3 sec.

2.2 FAST

The FAST spacecraft was launched on August 21 1996 into a high inclination orbit (83 deg). The orbital period was 133 min or 2.2 hr. The apogee and perigee were 4175 x 350 km altitude or 1.65 x 1.05 Re geocentric distance. The spacecraft spun at the period of 5 sec and precessed 3 hr/month. The spacecraft usually only collected data at the high-latitude regions. The common time when both Polar and FAST were collecting electric field data was the 6.2 yr from August 30 1996 to Oct 25 2002. This is the time range over which the cusp study was performed. The FAST EFI (Ergun et al., 2001) measures the 2-D DC electric field in the spin plane, with 3 booms of 28 m long and 1 short boom which was not fully deployed. The spin axis booms are 7.7 m tip-to-tip. The electric data product calculated from the special boom geometry include 2-D fields at the data rate of 512 samples/sec. One component is along the spacecraft velocity and the other is near the background magnetic field. The 3-D DC magnetic field measured by the Magnetic Fields Instrument (MFI) (Elphic et al., 2001) has the data rate of 128 samples/sec. Similar to Polar, the electric

fields are interpolated to the lower of 128 samples/sec when calculating the Poynting flux. The particle data are provided by the Electrostatic Analyzer (ESA) (Carlson et al., 2001). The energy range is very similar to Hydra: 3 eV to 25 keV for electrons and 4 eV to 30 keV per charge for ions. ESA does not distinguish ion species and assume all ions are protons. The time resolution is 2.5 sec for the slow survey and 312 msec for the fast survey. The TEAMS (Time-of-flight Energy Angle Mass Spectrograph) (Klumpar et al., 2001) is used to check ion species information as an implement to ESA. The time resolution and energy range are the same as ESA.

2.3 RBSP/VAP and THEMIS/ASI

In the second part of the thesis, we investigate the role of the Poynting flux in the aurora physics, using the in-situ measure from the RBSP (Radiation Belt Storm Probes) or VAP (Van Allen Probes) mission and the ground aurora images from the ASI (All-Sky Imager) of the THEMIS (Time History of Events and Macroscale Interactions during Substorms) mission. The THEMIS mission included 5 spacecraft and more than 20 ground-based observatories. In this study, we only focus on the ground observations. The all-sky imagers spread over the north America provide aurora images every 3 sec at a spatial resolution of < 100 km (Mende et al., 2008). Appendix C discusses more details related to the all-sky imagers and the related data processing techniques.

The RBSP mission included two spacecraft, A and B, which carried identical instruments. The spacecraft were launched on August 30 2012 and still operating. The spacecraft orbit around the earth in an equatorial orbit (10 deg) for about every 9 hr, between the perigee at 1.1 Re and apogee at 5.8 Re geocentric distance. The spin period is about 11 sec. The spacecraft are oriented so that the spin plane is approximately facing the sun all the time. Such configuration provides a good coverage of the perpendicular electric field when the spacecraft sample the nightside plasma sheet and its boundary layer, where the magnetic field is approximately sunward. This feature is advantageous since the perpendicular fields

correspond to the parallel Poynting flux. For THEMIS (spacecraft) and Polar, only one component of the perpendicular electric field can be directly measured. The RBSP Electric Field and Waves instrument (EFW) (Wygant et al., 2013) provides DC E measurement at 16 samples/sec, with 4 spin-plane 50 m booms and 2 spin-axis 6 m booms. The 3-D DC magnetic field data are from the Electric and Magnetic Field Instrument Suite and Integrated Science (EMFISIS) at 32 samples/sec. The thermal plasma information is obtained by the Helium, Oxygen, Proton, and Electron (HOPE) Mass Spectrometer. The instrument provides moments for the electron and different ion species every 12 sec in the energy range of 1 eV to 50 keV per charge. The ions are assumed to be singly charged.

Chapter 3

First Observation of the Energetic Wind in the Mid-Altitude Cusp and the Poynting Flux as its Energy Source

3.1 Introduction

Ion outflow from the Earth's ionosphere during geomagnetically active times has been extensively studied for several decades. Ion outflow is a significant and at times dominant source of plasma for the earth's magnetosphere (e.g. Chappell et al., 2000). The ion outflow can strongly modulate the dynamical processes in the magnetosphere. Oxygen ions are enhanced in the plasma sheet during storm times (Kistler et al., 2005), and participate/modulate the reconnection in the magnetotail (Wygant et al., 2005). Simulation confirmed that the tail dynamics can be significantly modulated by the present of intense oxygen outflow (Wiltberger et al., 2010). In addition, ion outflow plays an important role in the ring current dynamics (Daglis et al., 1999).

In order to escape, ions must overcome gravity through energization in either the parallel or perpendicular direction. Thus, ion energization is the key to fully understand ion outflow. It is still open question on the energy source for the ion outflow, although tremendous efforts have been made to study the ion energization. Macroscopically, observations suggest that the ion energy increases with altitude in the high latitude region. Abe et al. (1993) examined Akebono data in the polar cap up to 10,000 km altitude (about 2.5 Re geocentric distance). They showed that the parallel velocity of the polar wind increases with altitude for major ion species (H^+, He^+, O^+). Bouhram et al. (2004) found that the mean energy of oxygen increases with altitude in the cusp/cleft region during ion outflow events. They were able to explore the altitude range up to 6 Re, by combining Akebono, Interball-2 and Cluster data. Microscopically, many energization mechanisms have been proposed to explain the observed ion distribution. These energization mechanisms can be categorized into perpendicular and parallel (Moore et al., 1999, and references therein). Miyake et al. (1993) examined the folding of ion conics and showed that the folding is slower than adiabatic, providing evidence for perpendicular heating. BBELF (Broad Band Extremely Low Frequency) waves are commonly observed with perpendicularly heated ions (André et al., 1990). It is suggested that BBELF waves can energize ion at the cyclotron frequencies (Chang et al., 1986) and lower frequencies (Temerin and Roth, 1986; Hultqvist, 1991). Kinetic Alfvén waves, EMIC (Electromagnetic Ion Cyclotron waves), EIC (Electrostatic Ion Cyclotron waves) (Lysak et al., 1980) and lower hybrid waves (Chang, 1993) may also be important since these waves can easily interact with ions and therefore exchange energy with them. Parallel energization is thought to involve in establishing a quasi-static potential drop (e.g. Lundin and Hultqvist, 1989). However, for each mechanism, one needs to identify the free energy for wave growth to complete the theory.

The cusp at low-altitude has been extensively studied by the FAST spacecraft. Strangeway et al. (2005) studied the mass flow of the upwelling ions using FAST data. They found that the ion number flux correlated with enhancements in both the Poynting flux and elec-

tron precipitation. The former increases the ion scale height through Joule heating, while the latter increases the am-bipolar electric field which facilitates ions to escape. A net enhancement in the ion number flux is expected since more ions can reach the ambipolar electric field and that the ambipolar electric field is stronger. They are referred to as type I and type II ion outflows (Wahlund et al., 1992).

This paper investigates the energy flow of the cusp ions, which is a different topic to the mass flow but of equal importance. We report the surprisingly energetic wind of ion outflows in the mid-altitude cusp, which carries an upward kinetic energy of several 10s mW/m^2 to more than 100 mW/m^2 in extreme cases. As a comparison, the ion kinetic energy flux is usually downward and several orders of magnitude smaller at FAST altitudes, even during active times or when strong ion conics were observed (e.g. Pfaff et al., 1998; Strangeway et al., 2005). In this study, we compare measurements between mid-altitude and low-altitude during quasi-conjunction events and show that intense ion energization occurs above FAST altitude and that the earthward Poynting flux in the mid-altitude is only the energy source for the ion energization. Our study suggests that in addition to the first stage at ionospheric altitudes where the ion outflows are driven, there is a second stage in the mid-altitude where the ion outflows are significantly energized and that this energization is powered by Poynting flux.

The region of interest in this study is the cusp between about $2 - 6$ Re. Above this altitude is the exterior cusp or high-altitude cusp (Lavraud et al., 2005; Cargill et al., 2005). The high-altitude cusp is excluded from the study because it contains high-beta plasma affected by the magnetosheath Savin et al. (e.g. 2005). On the order hand, cusp plasmas below ~ 6 Re are low beta. The energy fluxes at various altitudes can be mapped to the ionosphere according to the converging magnetic field lines. In the 2-D plane of MLT and ILat, DMSP statistical study at several 100 km altitude showed that the cusp is a limited region of several degrees wide around 75 ILat and 3-4 hours wide in local time around noon (Newell and Meng, 1988, 1994). To be specific, we distinguish among cusp, cleft and polar

cap and only focus on the cusp events. The cleft maps to the LLBL, whereas the cusp is the direct entry of plasma and energy. The most intense outflows originate from the cusp/cleft region. During active times, the ions upwell from the cusp/cleft ionosphere due to enhanced energy input. The bulk motion of the low energy upwelling ion is referred to as the ion fountain (Lockwood et al., 1985a,b).

In order to identify the energy source and sink, we study a Gaussian volume and monitor the energy fluxes at the lower and upper boundaries using spacecraft observations, as illustrated in Figure 3.1. Although the location of the cusp depends on the dipole tilt angle, solar wind condition and reconnection properties (Newell et al., 1989; Newell and Meng, 1989; Russell, 2000), the cusps under the southward IMF are similar in the sense that they the energy-latitude dispersion, where high energy ions appear at low latitude. This dispersion pattern reflects a spatial structure along the convection direction (Trattner et al., 2002a). Similar dispersion patterns can be tracked for several hours in real time and several hours in local time, as long as the external conditions are stable (Trattner et al., 2002b). Given these results and the orbital constrains from Polar and FAST, we adopt the conjunction criteria of ~ 1 hour separation in MLT and ~ 1 hour in real time. The criteria is such determined to collect enough events for a good coverage of the cusp below 6 Re, yet to ensure that the conjunctions are physically meaningful.

With the Gaussian volume in Figure 3.1, we intend to monitor the ion energization in the cusp above the ionospheric altitudes. Specifically, we track the energy fluxes at the upper and lower boundaries, including the electromagnetic energy carried by the Poynting flux and the ion/electron kinetic energy fluxes. According to our observation, the cusp below 6 Re can be divided into the low- and mid-altitude cusps, where the boundary is around 2-3 Re. The separation is indicated from the energy partition pattern: within the mid-altitude cusp (3-6 Re), large earthward Poynting flux and upward ion kinetic energy flux were observed during the ion outflow events, whereas in the low-altitude cusp, all the energy fluxes are earthward and the major energy fluxes are the Poynting flux and electron kinetic energy

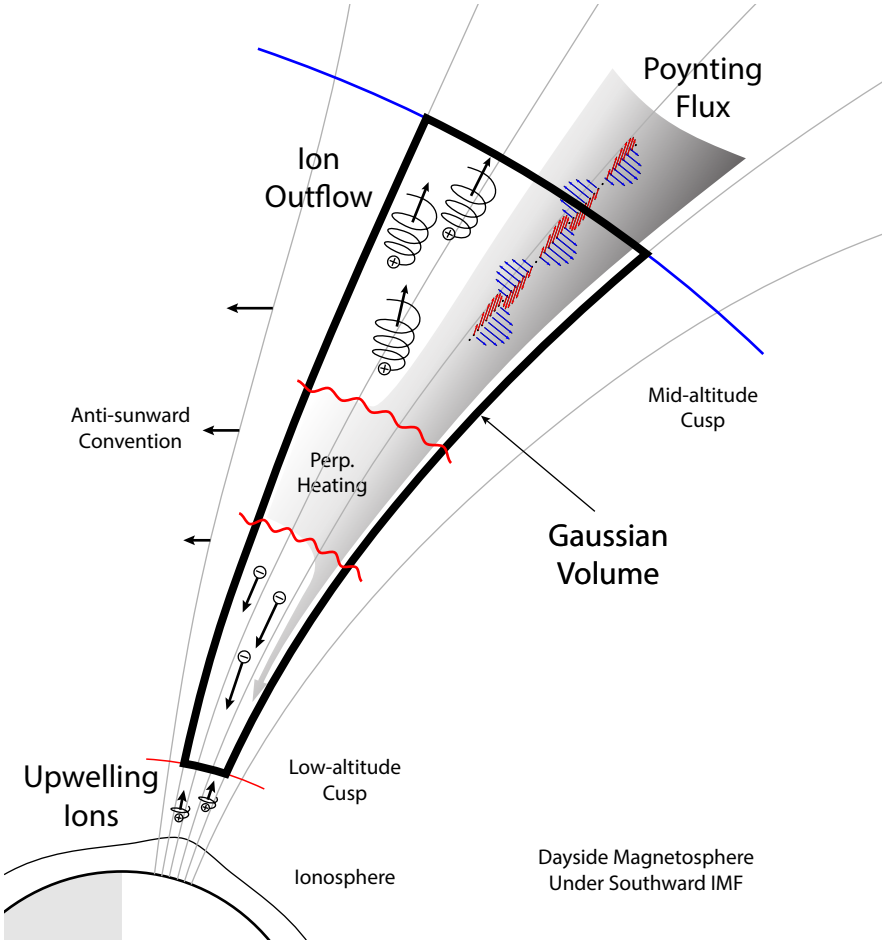

Figure 3.1: A schematic side view of the cusp. The blue and red traces are imaginary spacecraft tracks that sample the Gaussian volume encloses the mid-altitude cusp. The earthward Poynting flux flowing into the Gaussian volume is partially consumed, as inferred from the Poynting flux flowing out. In the mid-altitude cusp, the electromagnetic energy is energetically sufficient to explain the intense ion energization and account for the downward accelerated electrons at low-altitude. The ion outflow flowing out of the Gaussian volume carries a kinetic energy flux that is much larger than at low-altitude. The ion distributions suggest strong perpendicular heating at discrete altitudes in the mid-altitude range. Some of the ion kinetic energy flux may be lost from the side area of the Gaussian volume due to the anti-sunward convection.

flux. Interestingly, the electrons seem to be energized downward in the mid-altitude cusp, since the electron kinetic energy flux is much larger at the low-altitude. The bursty electron precipitations reported at low-altitude Su et al. (2001) are likely to be the result of the downward electron energization in the mid-altitude cusp.

Combining the low-altitude studies and the results in this study, we suggest a 2-step scenario for forming a plasma wind during geomagnetic active times (Figure 3.1). The first step is driving the ion outflow from the ionosphere, where the enhanced Poynting flux first energized electrons downward and then both the Poynting flux and the electron precipitations flow into the ionosphere to drive ion outflows. As ions are continuously upwelling, the energization of the wind occur in the mid-altitude cusp, where the upwelling ions encounter the later earthward Poynting flux.

3.2 Case Studies

In this section, we present two case studies of the cusp conjunctions. Intense earthward Poynting flux and ion outflows from the ionosphere were observed in both events. The first event showcases one of the most intense events (during the main phase of a geomagnetic storm, minimum Dst -207 nT). The second event was during a moderate storm (minimum Dst -58 nT) but featured with a very good conjunction between Polar and FAST.

3.2.1 Cusp conjunction on Sept 25, 1998

Figure 3.2 shows the spacecraft configuration during the conjunction. The footprints of Polar and FAST were close in local time and near noon. The invariant latitude of Polar was higher than FAST, probably because of the deviation from dipole configuration due to the anti-sunward drag of the solar wind. Both spacecraft were well below 70 deg ILat, which is a signature of strong dayside erosion (Burch, 1973). In UT, Polar crossed the cusp about 1 hr later than FAST. Given the large separation in time, the event may be more suitably called a “quasi-conjunction”. A number of factors suggest that the Polar and

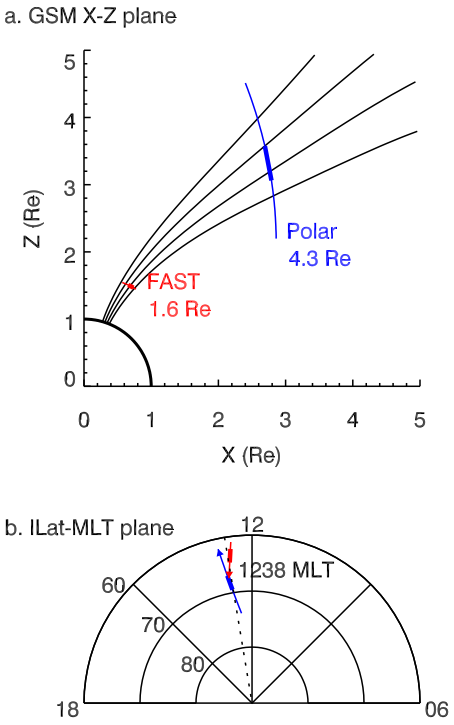

Figure 3.2: Spacecraft configuration during the conjunction event on Sept 25 1998. Panel a shows the spacecraft positions projected to the GSM $x - z$ plane. Also projected to the plane are the field lines modeled by T96. Panel b shows the spacecraft footprints on the ILat-MLT plane. The dotted line marks the averaged local time at 1238 MLT. In both panels, Polar (FAST) track is in blue (red) and the thick bar marks the cusp location. The arrows in panel b indicate the spacecraft direction.

FAST measurements were comparable. The external conditions (solar wind speed, velocity, magnetic fields) were stable during the conjunction (not shown), which favors the steady-state assumption. Indeed, the Sept 25 1998 event was studied by Trattner et al. (2002a) who showed that the Polar and FAST were sampling the same spatial structures in the ions along the cusp flux tubes at different altitudes. The main purpose of collecting FAST cusp crossings in quasi-conjunction with Polar is to monitor the boundary condition at the low-altitude cusp. The most reliable comparisons are those among the energy fluxes at Polar or FAST.

Figure 3.3 shows the overview of the observations from Polar at about 4.3 Re and FAST at 1.6 Re. The data from Polar and FAST are plotted versus invariant latitude (ILat). The cusp was characterized by high ion flux in the energy range from 100 eV to 10 keV. On the low-latitude side of the cusp is the dayside plasma sheet, filled with high energy ions ($>$ 10 keV). On the high-latitude side of the cusp is the plasma mantle due to the anti-sunward convection. The plasma in the cusp and polar cap were mostly in the perpendicular and upward directions, as indicated by the pitch angle spectrograms. For example, in panel b for Polar, the ions were peaked around 100 deg within the cusp and above 150 deg in the polar cap. Similarly, in panel g for FAST, the plasma peaked around 100 deg are perpendicular and slightly upward. This pitch angle distribution suggests local heating slightly below FAST. The loss cone is clear around 180 deg.

The particle kinetic energy fluxes are plotted in panel c and d for Polar, and panel h and i for FAST. They are mapped to the common altitude at 100 km to be inter-comparable. The mapped Poynting fluxes for Polar and FAST are shown in panel e and j respectively. The most striking feature is the large upward ion kinetic energy flux Γ_i within the cusp in panel c. The value of about 20 mW/m^2 is a significant energy flux in the earth's high-latitude region. As a comparison, the threshold for powering visible aurora is 1 mW/m^2. The electron kinetic energy flux (panel d) was of similar amplitude but varied in direction, which results in a negligible net energy flow across Polar. Coincide with the large upward

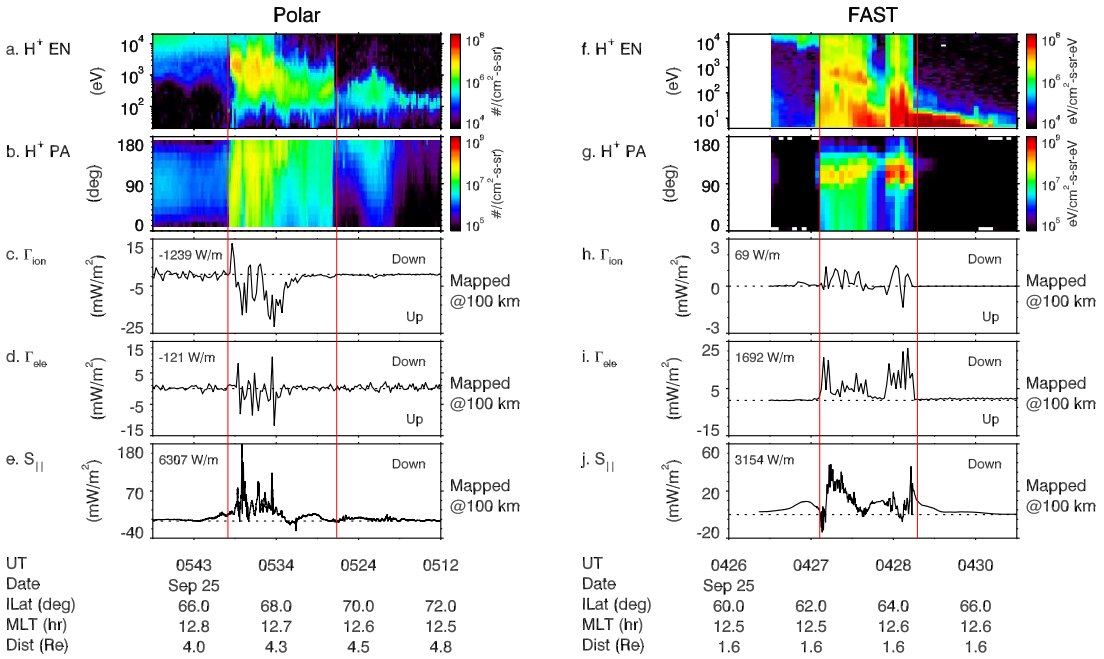

Figure 3.3: Overview of the cusp conjunction event on Sept 25, 1998. The Polar data are shown on the left and FAST on the right. Panel a is the proton energy-time spectrogram from the Hydra instrument for all pitch angle, where all the ions are assumed to be H^+. Panel b shows the H^+ pitch angle spectrogram from the TIMAS instrument, since Hydra does not provide this data product. Panel c and d show the ion and electron kinetic energy fluxes derived from Hydra. Panel e shows the parallel Poynting flux. The waveforms of the electric and magnetic fields related to the Poynting flux calculation are shown in Figure 3.5 and 3.6. The energy fluxes in panel c, d and e are mapped to 100 km altitude. Panel f to j are in similar format for FAST. The FAST particle data are all from the ESA instrument. The vertical red lines mark the cusp entry and exit. The value in the upper-left corner of the panels is the integrated energy flux within the cusp along the mapped track.

(W/m)	$\int ds\,\Gamma_i(100)$	$\int ds\,\Gamma_e(100)$	$\int ds\,S_\parallel(100)$	Total
Polar	-1162	-113	5904	4629
FAST	69	1692	3154	4915

Table 3.1: Mapped and line-integrated energy fluxes for the conjunction event on Sept 25, 1998. The unit of the quantity is W/m. Positive (negative) value is earthward (upward).

Γ_i was the large earthward Poynting flux within the cusp (panel e). The Poynting flux was mostly earthward so only the parallel component is shown. The correlation between the large earthward Poynting flux and the large upward ion kinetic energy flux is repetitively observed in mid-altitude cusp crossings, as will be shown in the second event in this section and the statistical results in Section 3.3.

To estimate the total energy flows across Polar, the mapped energy fluxes are line-integrated within the cusp along the spacecraft track at $h_0 = 100$ km altitude. The in-situ energy flux is mapped to h_0 based on the ratio of the magnetic field at spacecraft and the dipole field at h_0. The footpoint is found using the T89 model, although the mapping coefficient is insensitive to model choice. Table 3.1 lists the integrated energy fluxes at Polar and FAST. We use the notation of $\int ds\,\Gamma_i(100)$ for the mapped and line-integrated ion kinetic energy flux Γ_i. The notation indicates that the integration is a spatial integration, since the variation in Γ_i is understood as spatial as demonstrated in Trattner et al. (2002a). The quantity $\int ds\,\Gamma_i(100)$ has a unit of (W/m), whereas the energy fluxes are in (W/m^2). Comparisons among the values at Polar shows that the upward $\int ds\,\Gamma_i(100)$ was much larger than $\int ds\,\Gamma_e(100)$, which was also slightly upward. In terms of magnitude, $\int ds\,\Gamma_i(100)$ was a significant fraction (about 20%) of $\int ds\,S_\parallel(100)$, which implies that the ion energization is very efficient. On the other hand, at the low-altitude monitored by FAST, the energy partition among the ion, electron, and wave was very different. There the significant energies were $\int ds\,\Gamma_e(100)$ and $\int ds\,S_\parallel(100)$. All the integrated energy flows were downward at FAST.

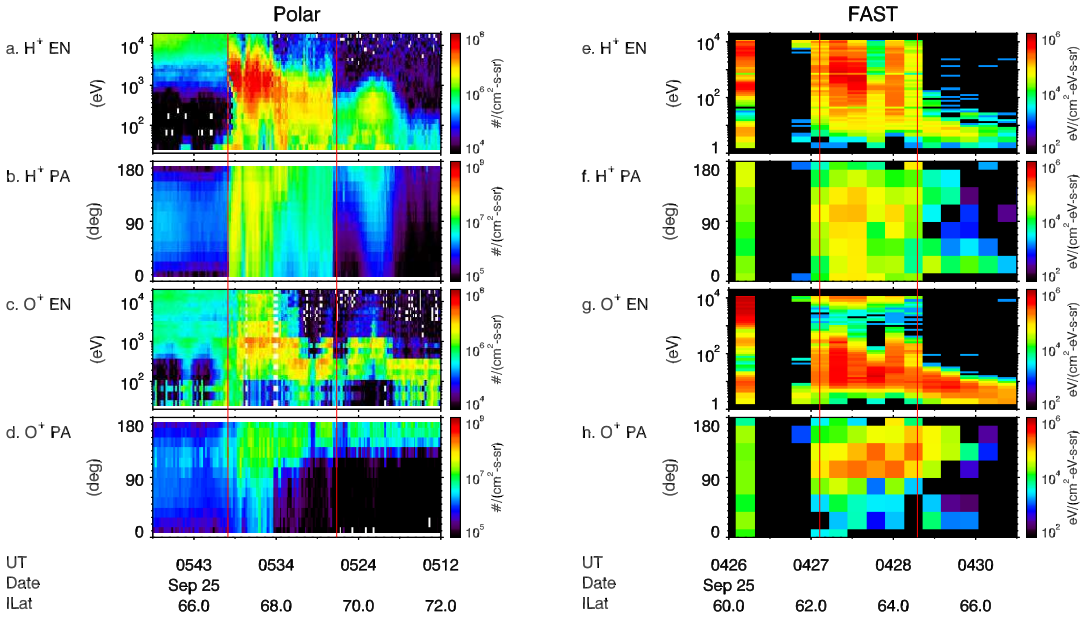

Figure 3.4: H^+ and O^+ measurements during the the conjunction event on Sept 25, 1998. The Polar TIMAS data are shown on the left and the FAST TEAMS data on the right. Panel a and b show the H^+ time-energy spectrogram and pitch angle spectrogram respectively. Panel c and d are in the same format for the O^+. Panel e to h show the same quantities for FAST.

To confirm that the ion outflows were of ionospheric origin, we present the H^+ and O^+ measurements for Polar and FAST in Figure 3.4. Panel c and d show that there was O^+ outflow from 100 eV to 1 keV. The O ions were mainly upward in the polar cap and somewhat more perpendicular in the cusp. The polar cap population was likely to be the polar wind, while the cusp population indicated perpendicular heating below Polar. Similarly at FAST, panel g and h show the existence of perpendicularly heated O^+ in the cusp and more field-aligned O^+ in the polar cap. Interestingly, the O ions within the cusp were elevated significantly in energy from FAST (about 100 eV) to Polar (about 1 keV), which suggests a significant energization below Polar but above FAST. By comparing the flux of the $H+$ and O^+, we could estimate the ratio of the number density between them R_{n_O/n_H} by integrating over all energy bins . The averaged density ratio at Polar was 1.5 in the cusp and 10 in the polar cap, showing the abundance of the O^+ ions and the clear ionospheric origin of the outflow. Similarly, the ratio at FAST was 10 inside the cusp and 30 in the polar cap.

The Poynting flux in the above table is calculated according to Equation (B.7),

$$\boldsymbol{S}(p,t) = \alpha \Re\{\boldsymbol{E}(p,t)\} \times \Re\{\boldsymbol{B}(p,t)\},$$

where α is a constant coefficient and p is the wave period. $\boldsymbol{E}(p,t)$ is the Morlet wavelet transform of the 3-D electric field time series $\boldsymbol{E}(t)$. The calculation of the Poynting flux is described in detail in Appendix B. The Morlet wavelet transform of the E/B fields and the Poynting flux of Polar are shown in Figure 3.5. Figure 3.6 is in the same format for FAST data. Panel c-1 in these two figures shows that the Poynting flux power at extremely low frequency is infected by the edge effect. For example, the constant offset in panel c-2 of Figure 3.6 is the result of the artificial power due to the edge effect. As a uniform treatment for both Polar and FAST, the frequency $f_C = 1/T_C$ corresponds to the duration of the cusp crossing T_C is used as the upper limit for filtering. Only the wave power below that frequency is included in calculating the total Poynting flux. As a comparison, the corrected Poynting flux in Figure 3.3 does not contain the artificial offset.

To further explore the wave modes carrying the earthward Poynting flux, the E/B ratio is calculated and plotted in panel c-3 in Figure 3.5 and 3.6. For the Polar data in Figure 3.5, the E/B ratio for wave period of 5-100 sec was a little below the local Alfvén speed if all ions are assumed to be protons. Thus this frequency band is most likely to be carried by Alfvén waves, which have an E/B ratio of the local Alfvén speed (Equation (3.55) in Paschmann et al., 2003; Wygant et al., 2000). The wave power below 5 sec periods is likely to be carried by the kinetic Alfvén waves (KAW). The E/B ratio of KAW is usually larger than the local Alfvén speed by a factor less than 10 (Lysak and Lotko, 1996; Wygant et al., 2002). Similarly in panel c-3 of Figure 3.6, the E/B ratio for periods between 1 to 10 sec of several 10^3 km/s is well below the local Alfvén speed even when all ions are assumed to by O^+. This power may be due to the field-aligned current and steady-state structures. These structures have an E/B ratio of $1/\mu_0\Sigma_P$ (Equation (3.45) in Paschmann et al., 2003), where μ_0 is the vacuum permeability and Σ_P is the height-integrated Pedersen conductivity. This E/B ratio is usually an order of magnitude smaller than the local Alfvén speed. However, the situation is more complicated at FAST, where at low-altitudes the reflected Alfvén wave can overlap significantly with the incident wave. The interaction of the incident and reflected Alfvén waves is known to lower the E/B ratio (Section 3.4.2 in Paschmann et al., 2003; Dombeck et al., 2005). Therefore it is also possible that the significant power at periods of 1-10 sec is due to Alfvén waves involving reflection. In addition, the local Alfvén speed may be overestimated, due to the fact that the density is usually underestimated from integrating energy bins greater than the spacecraft potential.

For the electric field data from both Polar and FAST, only spin plane data are used. In the cusp geometry, the spin-axis component is approximately along the east-west direction in the field aligned coordinate system. And the electric field is usually largest in the north-south component. Therefore the usual $\boldsymbol{E} \cdot \boldsymbol{B}$ correction cannot give the spin-axis electric field. However, for Alfvén waves and field-aligned current, the spin-axis electric field can be calculated based on $\delta\boldsymbol{E}_\perp \cdot \delta\boldsymbol{B}_\perp = 0$. By doing so, we get a correction of 30% on average to

the total power of the Poynting flux.

3.2.2 Cusp conjunction on Oct 01, 1998

As a second example, we will discuss the conjunction event on Oct 01, 1998. The event featured a quasi-conjunction between Polar and 2 successive FAST cusp crossings. We will focus on the conjunction between Polar and the first FAST orbit. The second FAST orbit provided evidence for a stable cusp over 2 hours in real time and several hours in local time. Figure 3.7 shows the spacecraft locations in the X-Z and ILat-MLT planes. The cusp in this event was at a higher latitude than the Sept 25 1998 event, because it occurred during a moderate storm, which is less capable of eroding the dayside flux tube.

Figure 3.8 is in the same format as Figure 3.3 and shows the data from Polar and the first FAST orbit. The cusp crossing was identified through the high flux around 1 keV in the ion energy-time spectrogram. The pitch angle spectrogram in panel b shows upward ions. For example, the ions around 77 deg ILat were concentrated between 90-180 deg pitch angle, and carried the large upward ion kinetic energy flux in panel c. For FAST in panel g, there were peaks around the loss cone, which suggests perpendicularly heated ions around or below the spacecraft altitude. There was significant O^+ present in the cusp and polar cap. The density ratio R_{n_O/n_H} for this event at Polar was 0.1 in the cusp and 1.6 in the polar cap and the ratio at FAST was 9 in the cusp and 11 in the polar cap (not shown). Comparing the energy fluxes, we observe the same energy partition pattern in the Sept 25 1998 event. For Polar (panel c-e) within the mid-altitude cusp, the earthward Poynting flux and the upward Γ_i are the major energy fluxes, whereas Γ_i is much less energetic. For FAST (panel h-j) at the low-altitude cusp, all energy fluxes were earthward. The downward Poynting flux and Γ_e were the main energy flux carriers. The line-integrated energy fluxes are summarized in Table 3.2.

One noteworthy feature is the shape of the Γ_i, which is related to the selection criteria of the ion outflow event. Both Polar and FAST observed downward Γ_i at the low latitude

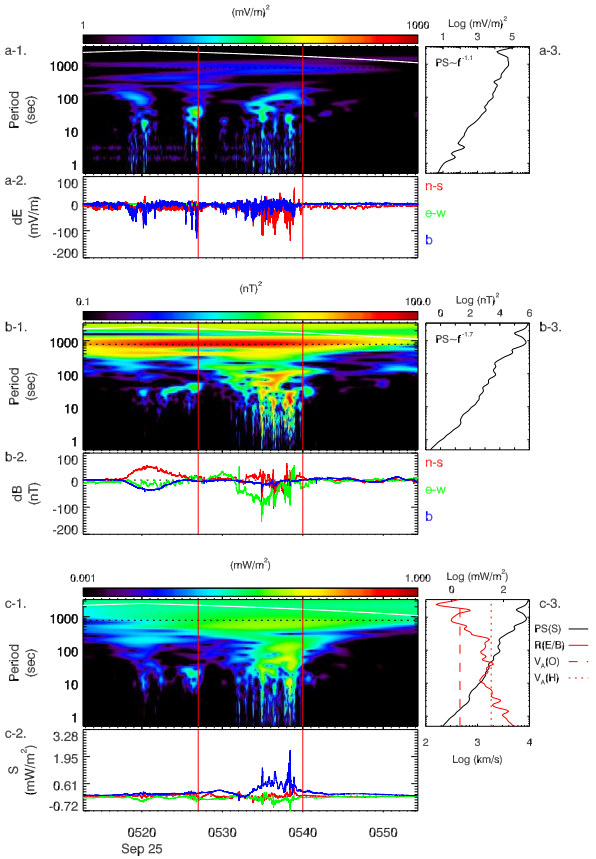

Figure 3.5: Polar waveforms and Poynting flux during the conjunction event on Sept 25, 1998.

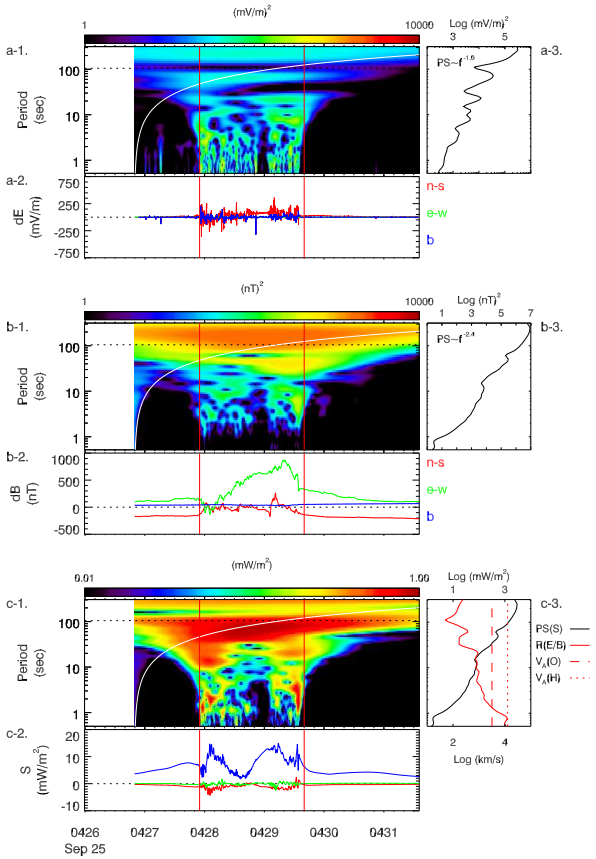

Figure 3.6: FAST waveforms and Poynting flux during the conjunction event on Sept 25, 1998.

The 3 panels are for the electric field, magnetic field and Poynting flux respectively. For example, panel a-2 shows the waveform of the electric field in field-aligned coordinates. The components are: red: north-south direction when mapped to the ionosphere; green: east-west direction; blue: parallel to the local background magnetic field. Panel a-1 shows the wavelet power spectrogram for $|\boldsymbol{E}|$. The horizontal dotted line marks the truncate period, which equals to the duration of the cusp crossing. The area above the white line is affected by boundary effect (cone of influence). Panel a-3 is the global wavelet power (which is comparable to the power spectrum in FFT). Panel b and c are in the same format, except that panel c-3 contains more information on the E/B ratio (red curve). The red dashed (dotted) line marks the local Alfvén speed V_A when all ions are O^+ (H^+).

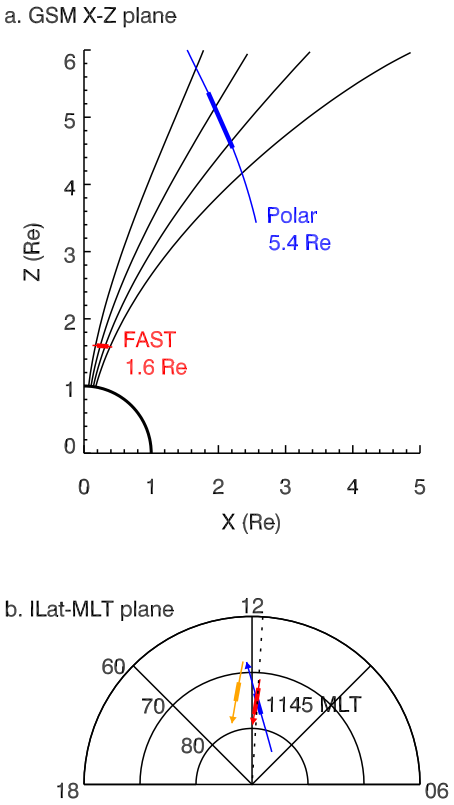

Figure 3.7: Spacecraft configuration during the conjunction event on Oct 01 1998. The format is the same as Figure 3.2. The second FAST crossing is colored by orange in panel b. The two FAST crossing shared the same track in the GSM $x - z$ plane, so only the track of the first FAST crossing is plotted in panel a.

(W/m)	$\int ds\,\Gamma_i(100)$	$\int ds\,\Gamma_e(100)$	$\int ds\,S_{\parallel}(100)$	Total
Polar	-657	-2	1980	1321
FAST 1	43	210	546	799
FAST 2	13	373	493	879

Table 3.2: Mapped and line-integrated energy fluxes for the conjunction event on Oct 01, 1998. The unit of the quantity is W/m. Positive (negative) value is earthward (upward).

boundary within the cusp (c.f. panel c and h in Figure 3.8). The downward Γ_i is due to the strong precipitation from the dayside reconnection site. At the low-altitude, the ion outflow is another population completes with the precipitation. The situation is more complicated in the mid-altitude, where there is a second upward population due to the mirrored precipitation. During a quiet time, if the spacecraft passes the mid-altitude cusp along the anti-sunward convection, a bipolar Γ_i would be observed. $\int ds\,\Gamma_i$ would be around 0 but slightly downward, since there is no outflow and only part of the precipitation is mirrored. The situation is different when ion outflows are present, as in the examples on Sept 25, 1998 and Oct 01, 1998. The ion outflow contributes significantly to the upward kinetic energy flux, so that Γ_i integrated to large value in the upward direction. Given the above observations, we define the "ion ratio" R_i to select ion outflow events.

$$R_i = \frac{\int_{\Lambda_l}^{\Lambda_h} \Gamma_i\left(\Lambda\right) ds}{\int_{\Lambda_l}^{\Lambda_h} \left|\Gamma_i\left(\Lambda\right)\right| ds}, \tag{3.1}$$

where Λ is the invariant latitude, Γ_i is the in-situ ion kinetic energy flux. Λ_l and Λ_h are the low and high latitude boundary of the cusp. The cusp boundaries are determined based on the existence of high flux of the ions from 100 eV to 1 keV and strong wave activity. R_i is close to 0 when no ion outflow is present. In this paper, ion outflow events are defined to have $R_i \leq -0.5$, i.e., the out flowing ions carry more than twice the energy flux of the downgoing ions.

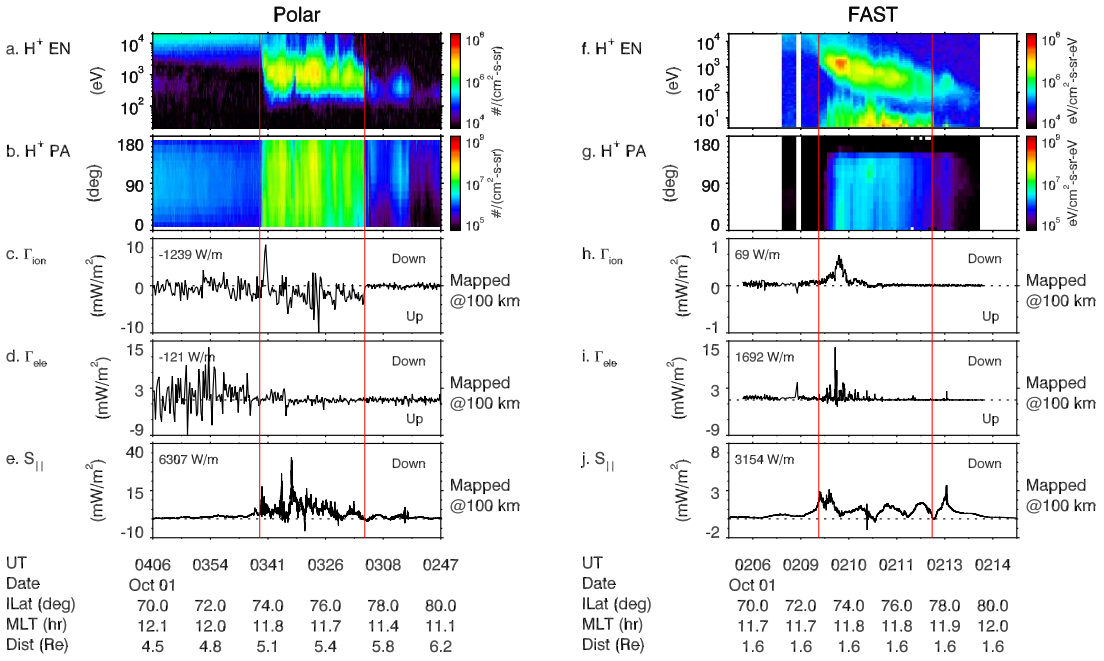

Figure 3.8: Overview of the cusp conjunction event on Oct 01, 1998. The panels are the same as Figure 3.3.

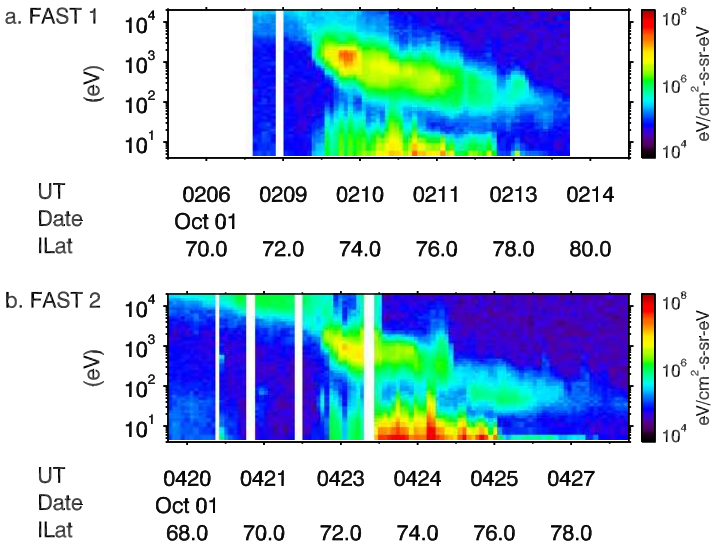

Figure 3.9: Comparisons between the two FAST cusp crossings on the conjunction event on Oct 01, 1998. Panel a shows the ion energy spectrogram integrated over all pitch angles for the first FAST orbit, which was spatially in conjunction with Polar. Panel b shows the second FAST orbit, which was about 2 hr later than the first FAST orbit. It is about 1 hr westward in local time from the first FAST orbit, according to Figure 3.7.

The conjunction between Polar and the first FAST cusp crossing was close in spatial location but separated by about 1.5 hr in real time. However, the observation during the second FAST crossing suggests that the cusp was stable during the conjunction. Figure 3.9 shows the ion energy spectrograms of the two successive FAST cusp crossings. Despite the difference in cusp location, the spectrograms are comparable in many aspects. The similar latitude-energy dispersion required similar precipitation and anti-sunward convection. Given that the solar wind condition, which determines the energy of the precipitation and the convection speed, was stable between the two FAST orbits, the comparable ion spectrograms support that the time stationary assumption is applicable and therefore the same quantity between Polar and FAST is comparable. Table 3.2 includes the integrated energy fluxes for the Polar orbit and the two FAST passes. If the quantities in the same column were compared, we observe that the main ion energization occurred above FAST, at the cost of consuming the earthward Poynting flux. The earthward Poynting flux in the mid-altitude

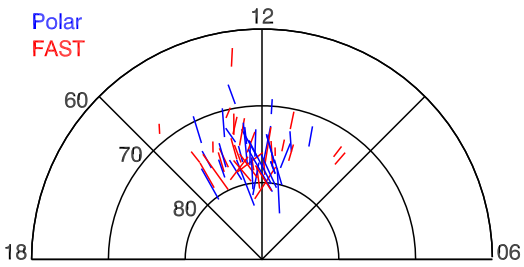

Figure 3.10: The cusp location for the south IMF events in the MLT-ILat plane. The orbits were approximately along the anti-sunward convection direction and within ±3 hr around noon. This is where the cusp is expected when IMF B_y is small compared to B_z.

cusp is the only possible energy source for the ion energization according to the conjunction measurements.

3.3 Statistical Results

In the previous section, we described two case studies during geomagnetically active times, when intense ion outflows were observed in the cusp. In order to study the energization process and determine the energy sources and sinks, we focus on the Poynting flux and the ion/electron kinetic energy flux Γ_i/Γ_e. The common features of the two events include: (1) large earthward Poynting flux and large upward Γ_i in the mid-altitude cusp; (2) slightly downward Γ_i along with significant downward Poynting flux and Γ_e in the low-altitude cusp. Combining these features, we found that the out flowing ions were energized significantly and the energization occurred above the low-altitude cusp. The Poynting flux was the energy source for the ion energization and was significantly consumed before reaching the ionosphere. The electrons were another energy sink. They were energized downward in the mid-altitude cusp.

Given the above studies, it is interesting to explore more cusp crossings to check whether the above conclusions are generally valid. To serve this purpose, we conducted an extensive search on Polar and FAST conjunctions within the cusp. The searched period is from

1996 to 2000, when both spacecraft have particle and electric and magnetic fields data. August to October are examined for two reasons. The first is to eliminate seasonal effects. The examined period is around equinox so events from both hemispheres can be treated equivalently. The second reason is that during the fall season, the orbital planes of Polar and FAST were both close to the noon-midnight meridian. It is important that the spacecraft followed the convection direction, to lower the chance of biased sampling of certain fraction of the dispersed ions.

We identified 77 Polar/FAST quasi-conjunction events, using the following criteria for a magnetic conjunction: the spacecraft were within ~ 1 hour in MLT and crossed the cusp within ~ 1 hour in UT. To simplify the discussion, we identified 35 "southward IMF events" by the following procedures. The solar wind data were manually examined to exclude events under varying IMF/dynamic pressure , northward IMF, and large B_y. The ion spectrogram was checked for the normal energy-latitude dispersion (high energy ions at low latitude). Cleft events are excluded if the event is away from noon or has low flux in the ion spectrogram. A subset of special interest is the 11 "ion outflow events". As explained in the previous section, these events have $R_i \leq -0.5$ at Polar. We will focus on the 35 southward IMF events and highlight the 11 ion outflow events in this section, and the ion outflow events are highlighted with red points in the Figures. Figure 3.10 shows the distribution of the southward IMF events in the MLT-ILat plane. As expected, most of the orbits are around the noon and between 70-80 deg ILat, roughly long convection direction. Figure 3.11 shows the ion kinetic energy flux in the GSM X-Z plane, where both the Polar and FAST data are presented in the same color scale. The plot shows that upward ion kinetic energy fluxes appear only in mid-altitude. The upward ion kinetic energy flux is usually poleward to the downward ion kinetic energy flux and more extended in latitude. In contrast, the ion kinetic energy flux in low-altitude is much smaller and around 0.

The Polar and FAST cusp crossings in the southward IMF events are grouped according to altitude. The low-altitude (mid-altitude) orbits are below 2 Re (in 3-6 Re) geocentric

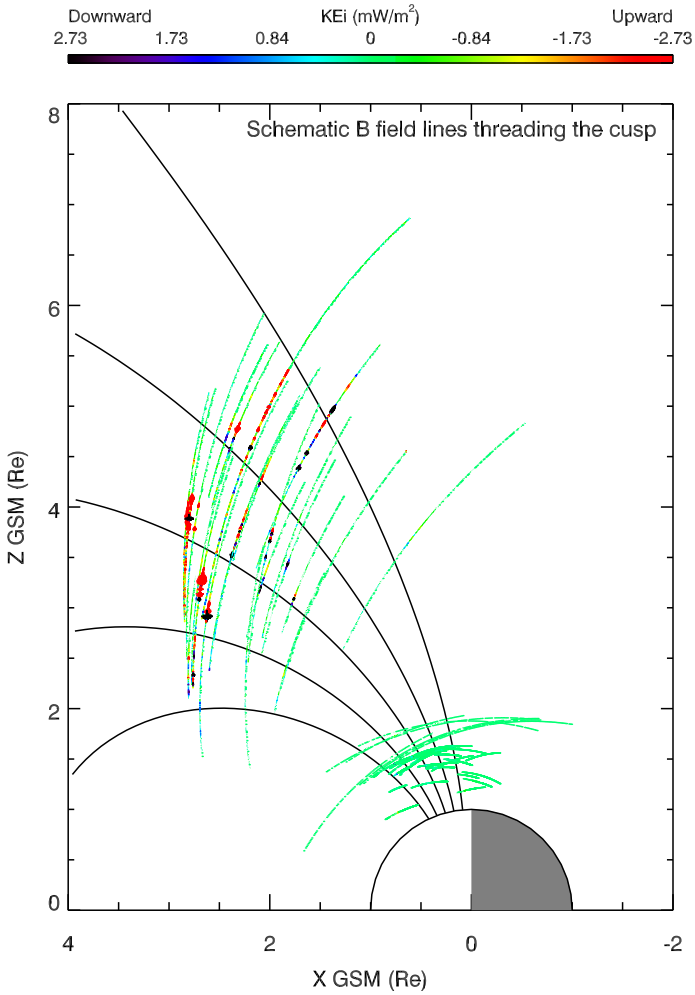

Figure 3.11: The Polar and FAST ion kinetic energy fluxes along the spacecraft tracks on the GSM X-Z plane. The Sun is to the left and the field lines are schematic. The color indicates the value of the ion kinetic energy flux in a non-linear (arctan) scale. As indicated by the color bar, red is upward, green is around 0, and dark blue is downward. The plot shows that the upward values appear only in mid-altitude. The upward kinetic energy flux is poleward to and more extended than the downward kinetic energy flux. The ion kinetic energy flux is much smaller and around 0 in low-altitude.

distance. Figure 3.12 shows the energy partition in the low- and mid-altitude cusps. First, we compare the low-altitude panels in the second row, where all the orbits observed the same energy partition pattern. Panel b shows that the integrated Γ_e is always downward or near 0. Its value is comparable to the integrated Poynting flux in most cases. Panel d shows that the integrated Γ_i is much smaller than the integrated Poynting flux. Notice that the above pattern is independent on whether ion outflow is present or not. Although the total energy input to the ionosphere varies with geomagnetic activity level, the energy partition in the low-altitude cusp does not seem to change. The energy partition pattern in the mid-altitude cusp is more complicated. The complexity arises from the ion outflow. In panel c, the integrated Γ_i for the ion outflow events is all upward and close to the magnitude of the earthward integrated Poynting flux. In the meantime, panel a shows that the integrated Γ_e is also mostly upward during the ion outflow events. Comparing the magnitudes, it is clear that $S > \Gamma_i \gg \Gamma_e$. The earthward Poynting flux is the only plausible energy source for the ion outflow and it is large enough in magnitude. The other points in panel a and c can be the orbits during quiet times, or during active times but do not meet the criteria for the ion outflow events. What is still true for these points are that the integrated Γ_i is larger in magnitude than the integrated Γ_e. The direction of them varies but the cases when the integrated Γ_i is downward may be explained as quiet time orbits.

A different perspective is to combine all the cusp crossings with southward IMF to form the altitude profiles for the energy fluxes. These cusp crossings are all under similar IMF conditions and activity levels. The altitude profiles could reveal further information on the location of the energization processes. As shown in Figure 3.13, the profiles of the integrated Γ_i and the integrated Γ_e are qualitatively different. The integrated Γ_i is downward at low altitudes and primarily upward at higher latitudes with a wider range of magnitudes. However, the points during the ion outflow events highlighted with red are upward above 3 Re and have the largest values. These points also show a monotonically increasing trend up to at least 6 Re. The magnitude of the upward values are 1 order of magnitude larger

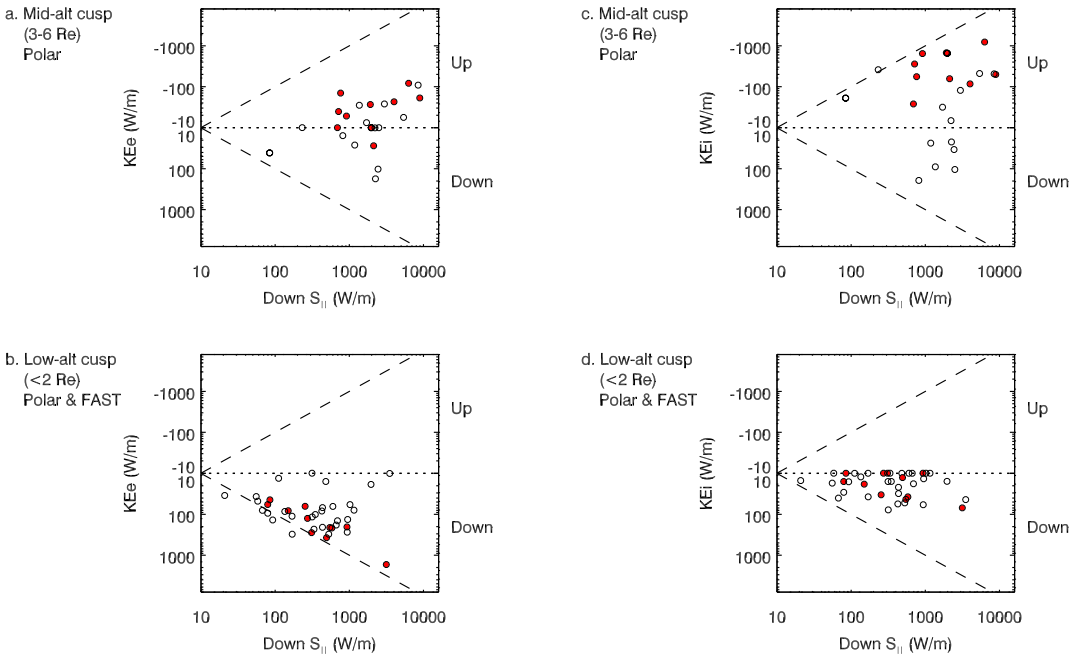

Figure 3.12: Comparisons among the integrated energy fluxes at low- and mid-altitude cusps. The bottom (top) two panels show the comparisons in the low-altitude (mid-altitude) cusp. Panel a and b show the comparison between the integrated Poynting flux and the integrated ion kinetic energy flux. Panel c and d show the comparison between the integrated Poynting flux and the integrated electron kinetic energy flux. Red symbols indicate ion outflow events as defined in the text.

than the values below 2 Re. This difference indicates the intense ion energization in the mid-altitude cusp. On the other hand, the electron profile above $\sim$ 4 Re is usually upward and decreases with altitude, but below 2 Re, it is downward and increases with altitude. The ion profile suggests that the ions are energized continuously through out the mid-altitude cusp. The electrons are energized at a limited layer somewhere between 2-4 Re. The profile of the electromagnetic energy decreases monotonically with altitude, which is consistent with the scenario that the electromagnetic energy carried by the Poynting flux is converted to the particle kinetic energy. However, caution is needed because the profile in panel c is physical only if the major Poynting fluxes are spatial[1]. With single spacecraft measurement, it is difficult to determine a spatial or temporal wave. Although Angelopoulos et al. (2001) showed that the mid-altitude cusp contains 2-D spatial turbulence by analyzing burst fields, it is in general difficult to determine whether the low frequency waves carrying the Poynting flux are temporal or spatial.

3.4 Summary and Discussions

In order to study ion energization within the cusp above the ionospheric altitudes, we have searched 4 years of Polar and FAST data and collected 35 quasi-conjunction events during intervals of southward IMF and moderately active periods (Dst $>$ -50 nT, with one event at Dst ~ -200 nT). There are 11 ion outflow events when intense ion outflows were observed. We have focused on 2 typical ion outflow events between Polar in the mid-altitude cusp and FAST in the low-altitude cusp. In the case studies, as well as the statistical results, the mid-altitude cusp has a qualitatively different energy partition pattern from the low-altitude cusp. In the mid-altitude cusp (3-6 Re), large earthward Poynting flux (greater than 200 mW/m^2 in extreme cases when mapped to the ionosphere) was frequently observed; the ion kinetic energy flux is a significant fraction (26% on average) of the earthward Poynting

[1]The upper limit for the Poynting flux is the mapped width of the cusp in the latitudinal direction. The cusps at different altitudes should map to a comparable width, since the cusp below 6 Re are well organized by the earth's magnetic field.

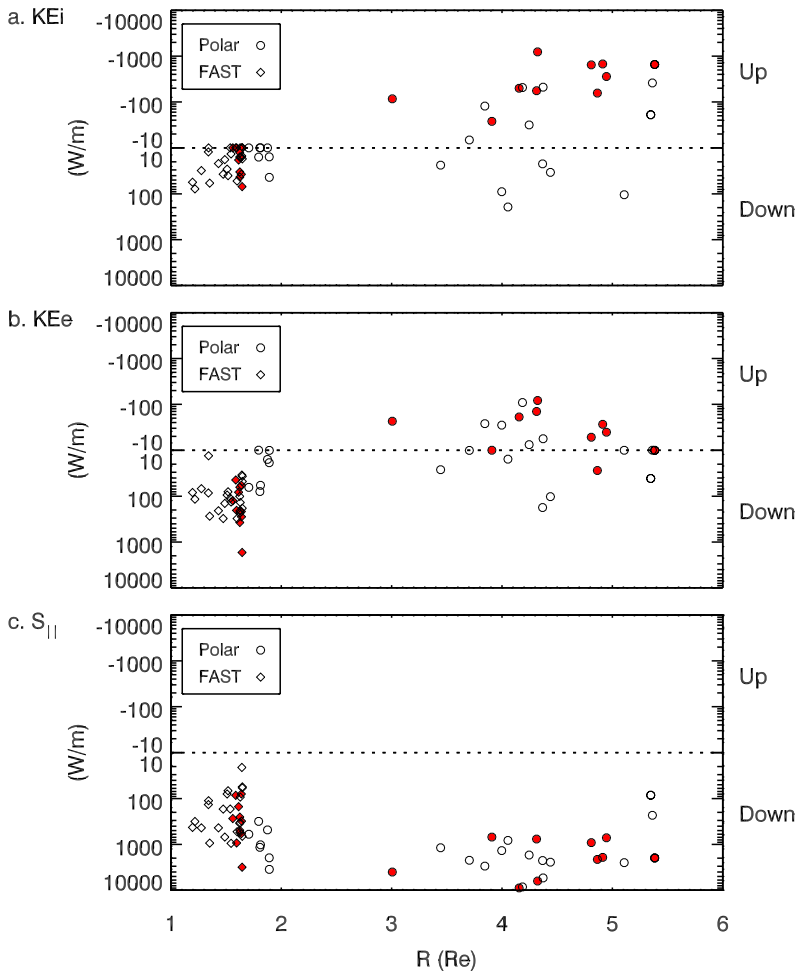

Figure 3.13: The altitude profiles of the integrated energy fluxes. The panels are: the integrated ion kinetic energy, the integrated electron kinetic energy, and the integrated parallel Poynting flux. Positive (negative) values are upward (earthward). The ion outflow events are highlighted with red. In this figure, Polar and FAST data are combined to cover the altitude range from about 1.2 Re to 5.5 Re geocentric distance, but for reference purpose the Polar and FAST orbits are labeled separately as circle and diamond respectively.

flux but in the opposite direction. The electron kinetic energy flux is much less than the other energy fluxes, and is usually upward when the ion kinetic energy flux is upward. On the other hand, all energy fluxes are earthward in the low-altitude cusp (<2 Re). The earthward Poynting flux and electron kinetic energy flux are comparable and both much greater than the ion kinetic energy flux.

The study shows direct evidence on the ion energization in the mid-altitude cusp, by examining the ion kinetic energy flux at different altitudes within the frame of the Poynting's theorem. The result is consistent with previous studies in the mid-altitude cusp. Miyake et al. (1993) studied the altitude dependence of ion conics in the dayside up to 2.5 Re geocentric distance. They found that the occurrence frequency of ion conics increases with altitude below 2 Re but is approximately constant above 2 Re. The folding of the conics is slower than expected from mirror force. These observations suggest that the ions are perpendicularly heated at least in the lower portion of the mid-altitude cusp. Bouhram et al. (2004) studied the altitude dependence of the transversely heated O^+ distributions in the cusp/cleft up to 6.6 Re geocentric distance, by combining the data from Akebono, Interball and Cluster. Although the work does not include the oxygen kinetic energy flux, it clearly shows that the upward velocity and mean energy increase with altitude, especially from 2.5-4 Re. In our study, the ion kinetic energy flux has a similar increasing profile and a sharp increase between 2-4 Re, and includes the contribution from all ions including O^+.

In this study, we approach the ion energization problem from the new perspective of the energy conservation within a meso-scale Gaussian volume comparable to the size of the cusp flux tube. The perspective is different from the micro-scale studies on the local wave-particle interactions (e.g. Chang et al., 1986; Chang, 1993; Hultqvist, 1991; Lysak et al., 1980; Temerin and Roth, 1986). However, our observations place several constraints on the possible mechanisms of local energization:

1. The only free energy source for the ion energization in the mid-altitude cusp is the electromagnetic energy carried by the Poynting flux. The precipitating electrons presum-

ably from the magnetosheath carry negligible energy flux compared to the Poynting flux.

2. The ion energization mechanism has to be very efficient since the ion kinetic energy flux is a significant portion of the earthward Poynting flux. This requires that the steps of energy cascade and conversion have to be very limited, and that the energization is likely to operate on the whole distribution instead of a portion of it.

3. The ion energization mechanism has to energize the electron as well. This requirement arises from the fact that the electron kinetic energy is often upward in the mid-altitude cusp when the ion kinetic energy flux is upward, and that although the electron kinetic energy flux is small at mid-altitude, it is downward and large at low-altitude. As shown in Figure 3.13, there seems to be a limited layer between 2-4 Re where the electron kinetic energy flux is peaked and likely to be upward.

4. The ion energization is primarily perpendicular heating, based on the observed ion distribution. Ion conics, and sometimes multiple conics are frequently observed in the mid-altitude cusp, which suggests strong perpendicular heating under the spacecraft at one or several altitudes. Simulations based on the observed distribution functions locate the perpendicular heating is around 2-4 Re, which is consistent with the peak location of the electron kinetic energy flux.

We note that the ion energization discussed above is the mid-altitude energization which gives rise to ion kinetic energy flux of several tens of mW/m^2. And it is different from the ion energization in the ionospheric altitude in the cusp, and the ion energization in the nightside aurora. In the latter two regimes, both electrons and the Poynting flux carry significant energy flux and thus are possible energy sources, and thus there are fewer constraints on the possible interactions. Another difference is that the ion energization in the ionosphere or the aurora zone is much weaker than the one in the mid-altitude cusp, in terms of the ion energy and the kinetic energy flux.

Chapter 4

Alfvénic Poynting flux at the Plasma Sheet Boundary Layer (PSBL) in Conjunction with Auroral Arcs and Dipolarization in the Inner Magnetosphere

4.1 Introduction

Auroral dynamics has been a fascinating topic for decades due to its direct connection to ionosphere-magnetosphere coupling. Although the discrete aurora is directly related to the auroral acceleration region around about 2 Re geocentric distance, the ultimate driver lies in the magnetotail. Tracing upward from the auroral acceleration region is the plasma sheet and its boundary layer. The earthward Alfvénic Poynting flux within and near the plasma sheet boundary layer (PSBL) was suggested to be the main energy source for the auroral acceleration, at least the portion of the most poleward aurora (e.g. Chapter 4 in

Paschmann et al., 2003). Case studies (Wygant et al., 2000, 2002) showed that strong earthward Poynting flux within the PSBL at altitudes of 4-6 Re was large enough to power the observed auroral. The earthward Poynting flux was mainly carried by Alfvén waves, which is efficient in transporting electromagnetic energy to the ionosphere (Wygant et al., 2000). Kinetic Alfvén waves were also present and could correspond to local dissipation through electron acceleration and ion heating (Lysak and Lotko, 1996; Wygant et al., 2002). The relationship between the aurora and Poynting flux has been further demonstrated by statistical studies (Keiling et al., 2003; Chaston et al., 2003) and simulations (Zhang et al., 2012). In this study, utilizing state-of-art ground and in-situ observations, we re-examine this relation at a much better spatial and temporal resolution than previous studies. For the first time, we show that there is a direct correlation in both time and location between the enhancement of the earthward Poynting flux within the PSBL and the auroral brightening at the footpoint of the corresponding flux tube. The event is also the first conjunction between the auroral westward traveling surge (WTS) and high-altitude spacecraft. The good correlation between the Poynting flux and aurora suggests that the WTS may represent the perpendicular propagation of the Alfvén waves in the magnetosphere.

Tracing the region where the Poynting flux is observed out from the PSBL is the mid-tail reconnection region. In the mid-tail, the high speed earthward flows of several 100 km/s were found to be essential in transporting energy, mass and magnetic flux (Baumjohann et al., 1990; Angelopoulos et al., 1992). At the leading edge of the fast flows are the dipolarizations indicated by a sharp B_z increase (e.g. Runov et al., 2009). These flows and the associated dipolarizations are thought to be an important component in auroral substorms (e.g. Sergeev et al., 2004). The earthward flows brake and diverge at about 10 Re as inferred from the sharp drop in occurrence rate of the high-speed flows (Shiokawa et al., 1997). Recently, Ergun et al. (2015) studied the large electric fields in the flow braking region using the THEMIS data and showed the observation of earthward Poynting flux in the form of Alfvén waves in the plasma sheet. However, their study did not examine the association with aurora. The

RBSP spacecraft cover a different region from THEMIS and thus provide a good complement to the THEMIS studies in the mid-tail. In this event, the RBSP spacecraft were around apogee in the inner magnetosphere. The spacecraft observed earthward Poynting flux around the PSBL, and simultaneously the aurora brightening was recorded by the ground all-sky imager.

The twin RBSP could be in conjunction with the THEMIS all-sky imager for hours around their apogees. This configuration provides an excellent opportunity to explore the relation among the plasma flow, magnetic field dipolarization, auroral motion, and the Poynting flux. In this report, we present one such event on June 07 2013. As illustrated in Figure 4.1, the two RBSP spacecraft, separated by about 0.5 Re azimuthally, observed the propagation of density structures and dipolarization signatures in the azimuthal direction (westward) in the pre-midnight sector. Direct spatial and temporal correlation was observed between the discrete aurora and the earthward Alfvénic Poynting flux. The propagation of the dipolarization matched the speed of the auroral WTS and much faster than the density structure. The Alfvén waves tend to concentrate at the density gradients in the vicinity of the PSBL, which may suggest that the phase mixing and/or mode conversion may be the wave generation mechanism(s) (e.g. Lysak et al., 2009). Clear evidence of ionospheric feedback is seen in the oxygen outflows observed several minutes after the Poynting flux enhancement. The time lag was consistent with a travel time of the outflow from around the auroral acceleration region to the RBSP spacecraft. Co-existing with the Alfvén waves are the high frequency waves including the kinetic Alfvén waves, time-domain structures, and lower hybrid waves. These waves are thought to be efficient in dissipating wave power locally (Lysak and Lotko, 1996; Ergun et al., 2009; Bryant, 1998). The inward motion of the plasma sheet is inferred from the equatorward motion of the auroral oval.

These observations suggest the following picture on how the inner magnetosphere is coupled to the ionosphere (Figure 4.1). The earthward Alfvénic Poynting flux carries the electromagnetic energy down to the auroral acceleration region, where the electromagnetic

energy is converted to the kinetic energy of the downward electrons and the ion outflows. The ion energization we are referring to is a second energization stage around the aurora acceleration region, after the initial energization at the ionospheric altitude described by Strangeway et al. (2005). Based on the observations at RBSP in this event and from THEMIS in previous studies, we propose a scenario on how the Alfvén waves around the PSBL are generated. The free energy source for the Alfvén wave may be supplied by plasma flows or directly from the reconnection region. Given the fact that Alfvén waves and the associated Poynting flux are usually concentrated at density gradients around the PSBL, a possible scenario if flow braking is assumed is that the compressional mode launched during flow braking undergoes mode conversion/phase mixing at the density gradients so that the shear mode is generated and radiate the electromagnetic energy. In addition to the above processes, local heating and acceleration are also present by dissipating the wave power locally via high frequency waves and small scale structures (kinetic Alfvén waves, time-domain structures, lower hybrid waves, etc).

4.2 Plasma Sheet Crossing on Jun 07, 2013

Both RBSP-A and RBSP-B were in conjunction with the ground aurora around 04:50 UT June 7, 2013. During the event, the RBSP spacecraft were in the pre-midnight sector in the PSBL of the northern hemisphere. In-situ observations include dipolarization signatures accompanied by large earthward Alfvénic Poynting flux and oxygen outflow. Simultaneously, the aurora observed by the THEMIS ASI brightened and expanded westward and poleward. This section includes the observations that demonstrate the above descriptions. Other observations, including dispersionless injections of energetic electrons up to 1 MeV and high frequency waves and small scale structures including kinetic Alfvén waves, time domain structures and lower hybrid waves, are out of the scope of this paper.

Figure 4.3a shows the meridian plane at 22 MLT, on which the T01 model field lines and spacecraft positions are projected. Section 4.3 will explain the reasons for choosing the

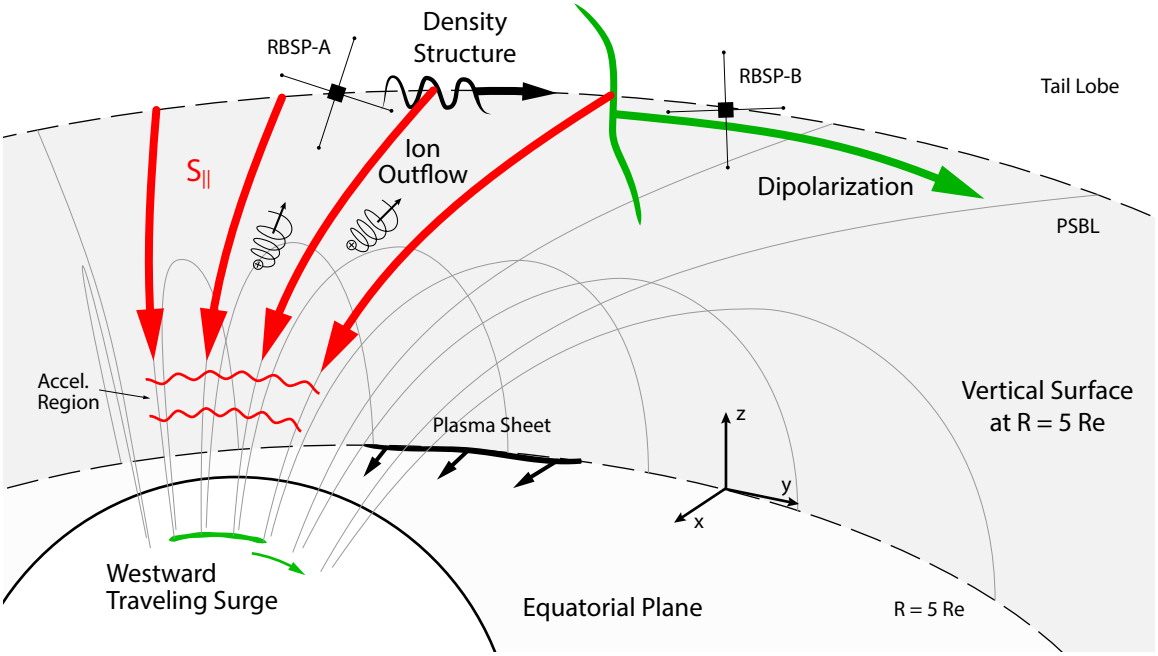

Figure 4.1: A schematic view of the coupling between the discrete aurora and the nightside magnetosphere. The gray surface is at the constant distance of $R = 5$ Re and vertical to the equatorial plane. The side view of the special is shown in panel b in Figure 4.2. The earthward Poynting flux ultimately powers both the discrete aurora and the oxygen outflow. The propagation of the dipolarization front may corresponds to the perpendicular propagation of the Alfvén wave and determine the auroral motion. The plasma flow releases its energy at the inner magnetosphere. Its kinetic energy flux is converted to the earthward Poynting flux (shear Alfvén waves) at density gradients around the PSBL through phase mixing/mode conversion.

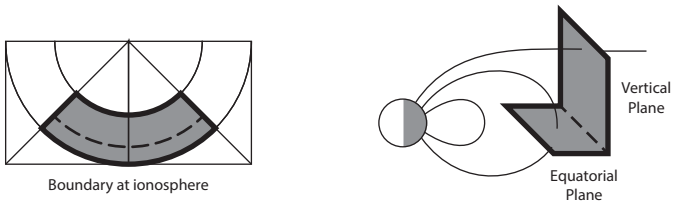

Figure 4.2: Schematic view of mapping the aurora in the ionosphere to the magnetosphere. The lower part of the auroral oval, containing the equatorial boundary and diffuse aurora, is mapped to the equatorial plane. The upper part, containing the discrete aurora, is mapped to a vertical surface at $R = \sqrt{X_{GSM}^2 + Y_{GSM}^2} \simeq 5$. The surface contained the RBSP spacecraft, and is approximated as a vertical plane for simplicity in the illustration. Mapping the discrete aurora to the vertical surface can significantly reduce the mapping error in location since the magnetic field between the ionosphere and the vertical surface is large in magnitude. On the other hand, the mapping error beyond the vertical surface scales scales with the expanding flux tube and can be significantly influenced by strong cross-tail current sheets.

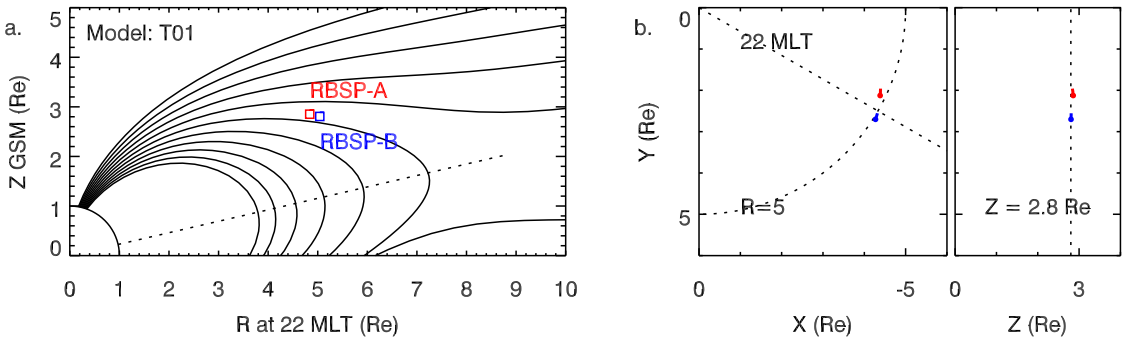

Figure 4.3: Magnetic field configuration and spacecraft position for the conjunction event on June 07 2013. Panel a shows the meridian plane at 22 MLT, in GSM coordinates. The magnetic field is calculated from the T01 model at 04:55 UT. The plot is semi-schematic, since the field lines and the spacecraft positions of RBSP-A (red) and RBSP-B (blue) are projected to this plane. The equatorial plane in SM is tilted by about 13 deg, indicated by the dotted line. Panel b shows the spacecraft positions in GSM coordinates. Only the X-Y and Z-Y planes are shown since the spacecraft were at almost the same Z GSM. Plotted are the trajectories of RBSP-A (red) and RBSP-B (blue) from 04:52 UT to 05:02 UT.

T01 model. The positions of the spacecraft in GSM are plotted in panel b. Both spacecraft were at $Z_{GSM} \simeq 2.8$ Re and $R = \sqrt{X_{GSM}^2 + Y_{GSM}^2} \simeq 5$ Re. The inter-spacecraft distance was 0.5 Re. Note that the although the spacecraft were at $R \simeq 5$ Re when projected to the GSM x-y plane, they map to a distance of 7 Re on the equatorial plane, as marked by the dotted line in Figure 4.3a. Later in the paper, the auroral oval will be mapped to the equatorial plane. The equatorward boundary of the aurora moved to as close as 5 Re in the equatorial plane, indicating an inward motion of the plasma sheet.

Figure 4.4 shows the overview of the key variables observed by RBSP and THEMIS/ASI. We will focus on the upper panels showing RBSP-A. The lower panels of RBSP-B are in the same format and show the same features. RBSP-A was sampling the PSBL before 05:07 UT and entered the CPS (central plasma sheet) afterward, as is evident from the particle signatures shown in panel a-1 and b-1. Panel a shows the electron spectrogram from HOPE, and panel b shows the electron density estimated from both HOPE (red line) and the EFW spacecraft potential (black). To estimate the density at higher cadence, the EFW spacecraft potential V_{SC} is fit to the electron density from HOPE. The fit shows that density from V_{SC} agreed with HOPE, and highlighted the density structure around 04:55-04:58 UT (there was another one around 05:06 UT, which is not further discussed since the conjunction between RBSP and the aurora was not as good). The density structure contained several fine structures which were vaguely indicated in the HOPE density. We note that the absolute density is usually underestimated in HOPE since only electrons above 200 eV are included. However, the underestimation is not important for the discussions in this paper. Detailed comparisons in Section 4.5 shows that the density structures at RBSP-A lead RBSP-B by 147 sec based on a cross correlation analysis. The time lag indicates a propagation speed of 25 km/s along the spacecraft separation, which was approximately along the westward azimuthal direction. A inward motion of the plasma sheet at 23 km/s was inferred from the equatorward motion of the auroral oval. This speed is comparable to the motion of the particle injection source in the inner magnetosphere (e.g. Moore et al., 1981; Reeves

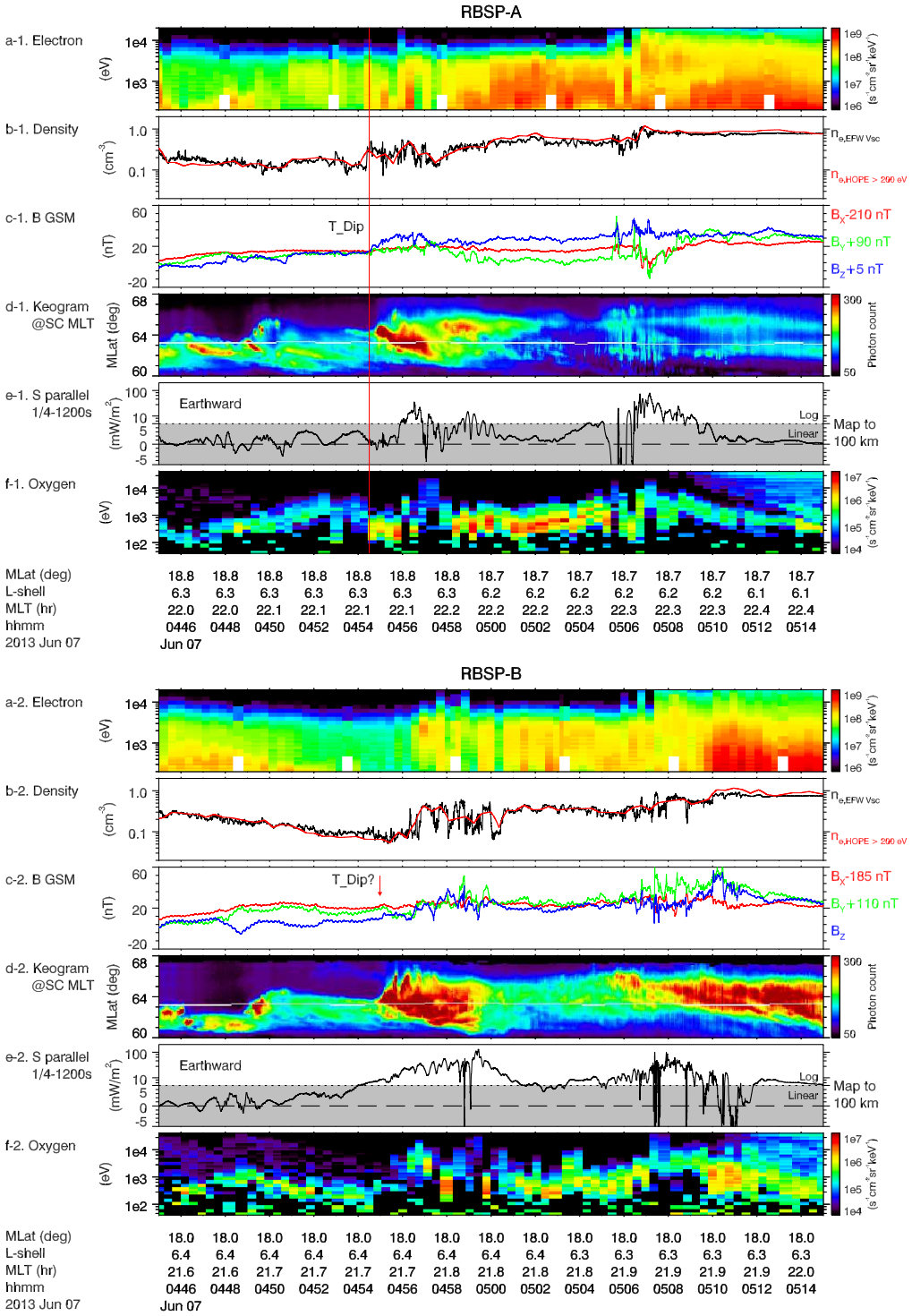

Figure 4.4: Overview on the in-situ measurements from RBSP-A and RBSP-B during the event on June . The panels are: (a-1) electron energy spectrogram; (b-1) electron density derived from HOPE and EFW; (c-1) B GSM. To emphasize the perturbations, the magnetic fields are shifted with the offset labeled on the right side of the panel; (d-1) auroral keogram at the MLT of RBSP-A's footpoint; (e-1) parallel Poynting flux mapped to the ionosphere at 100 km altitude; and (f-1) O^+ energy spectrogram. Panel (a-2) to (f-2) are in the same format for RBSP-B. The dipolarization time at RBSP-A is indicated by the vertical red line.

et al., 1996). The propagation of the density structure in the azimuthal direction may be the signature of a slow and localized plasma flow. However, since the HOPE velocity is not available at the time of writing, there is no direct evidence for the existence of a plasma flow at RBSP.

Dipolarization signatures are presented in panel c-1, which contains the 3-D magnetic field in GSM. In order to show the dynamic range of the perturbations, the components are shifted by their base values. The dipolarization time T_{dip} was identified by the initial increase in B_z. The T_{dip} was at 04:54:30 UT RBSP-A, characterized by a sharp increase in B_z about 8 nT. The total magnetic field was not shown in the panel but approximately proportional to largest component B_x. As shown in B_x, the dipolarization in the near-earth region does not cause significantly change in the magnitude and direction of the magnetic field. This is different from the dipolarizations in the mid-tail, where the background magnetic field is small. The dipolarization time at RBSP is not as clear. A possible time is the initial increase around the auroral brightening at 04:54:57 UT. The 27 sec time lag is determined based on a cross correlation analysis. However, later B_z increases from about 04:56:10 UT may be possible as well. If the time lag of 27 sec were used, a dipolarization propagation of 120 km/s along the westward azimuthal direction can be derived. Section 4.5 will discuss in detail the velocity comparisons between the auroral westward traveling surge and other velocities based on the RBSP observations, which suggests that the controller of the westward traveling surge may be in the magnetosphere, and may be the perpendicular propagation of MHD waves.

Right after the dipolarization signature, large earthward Poynting flux (panel e-1), auroral brightening and poleward expansion (panel d-1), and enhancement in the oxygen (panel f-1) were all seen. In a low beta plasma ($\beta \simeq 0.001$) like the near-earth PSBL, electromagnetic energy dominates plasma energy. The Poynting flux is the most important energy flux since it is the carrier of the electromagnetic energy. As calculated from the measured electric and magnetic fields, the Poynting flux was predominantly parallel, or earthward in

the northern hemisphere. In panel e-1, the earthward Poynting flux is mapped to 100 km altitude. As marked by the dotted line, the panel is divided into a linear part around 0 to show the small fluctuations and a logarithmic part to show the full dynamic range. The observed earthward Poynting flux is 2 orders of magnitude larger than the threshold required to power visible aurora (1 mW/m^2). Section 4.4 discusses the more properties of the Poynting flux. The Poynting flux was predominantly earthward and carried by Alfvénic structures. One interesting feature is that the earthward Poynting flux was concentrated at strong density gradients. For example, the Poynting flux peak around 04:56:30 UT coincide with the density gradient in panel b-1. This is an important clue on the Alfvén waves generation mechanism. The association with density gradient favors the non-linear mode conversion (Song and Lysak, 2013) and phase mixing (Allan and Wright, 2000; Lysak et al., 2009). The free energy source for wave growth is difficult to be unambiguously identified. But given the previous mid-tail observations (e.g. Ergun et al., 2015) and the RBSP observations in this event, flow braking in the near-earth region is a natural option. The compressional mode launched by the flow braking propagates as dipolarization and goes through mode conversion/phase mixing at the strong density gradients around the PSBL. According to the mid-tail studies, the plasma flow observed at RBSP was likely to be originated from reconnection deeper in the tail.

In the rest of the paper, we will focus on the 10 min period from 0452 to 0502 UT, when both RBSP-A and RBSP-B were in good conjunction with the ASI at PINA. The motion of the developing auroral arcs across the spacecraft footpoints is shown in Figure 4.5. Panel a shows the auroral oval before the event. The aurora brightened around 22.5 MLT and 63 deg MLat (panel b), then surged westward (panel c) and expanded poleward (panel d-f). The aurora faded afterward (panel g and h). One interesting feature is that the brightest aurora remained at the same latitude around 64 deg MLat during the westward surge and early poleward expansion. It is possible that the brightest arc corresponded to the strongest density gradient around the PSBL.

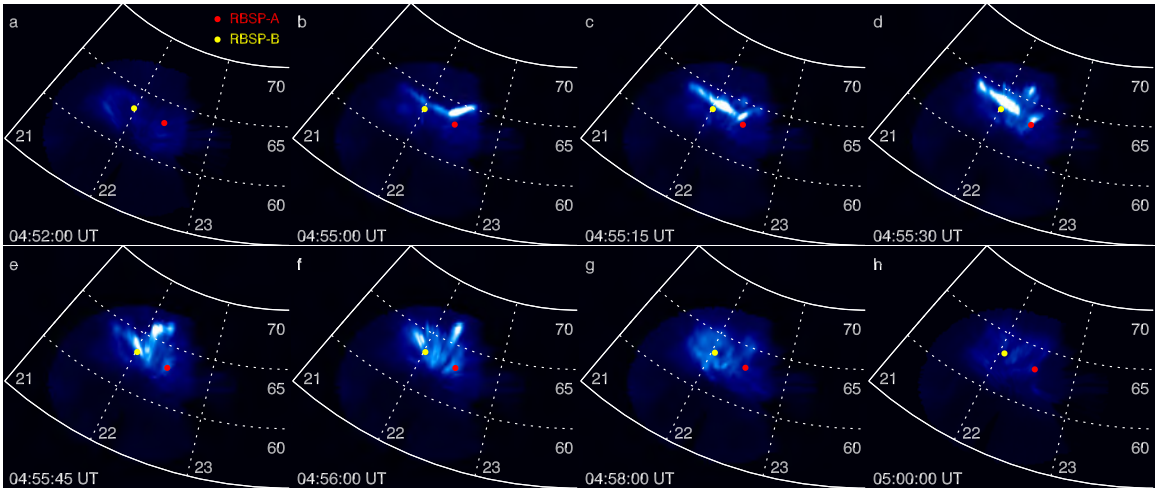

Figure 4.5: Snapshots of the aurora. The footpoints of RBSP-A (red) and RBSP-B (yellow) are plotted over the auroral image at the PINA site, in the MLT-MLat plane. Panel b show the appearance of an discrete arc. The arc traveled westward (panel c) and expanded poleward (panel d,e,f) and feinted (panel g,h).

4.3 Poynting Flux, Ion Outflow and Auroral Brightness

In this section, we show the detailed comparisons between the earthward Poynting flux, the kinetic energy of the oxygen outflow, and the auroral brightness. The Poynting flux and the kinetic energy flux were observed in-situ and mapped to the ionosphere at 100 km altitude.

Figure 4.6a-1 shows the keogram at the MLT of RBSP-A. The white line on top of the keogram is the MLat of RBSP-A according to T01 model. Panel b is the parallel Poynting flux filtered from 0.25 to 1200 sec. The frequency range is limited by the sample rate and event duration, but encloses most of the wave power in the DC fields (c.f. Figure 4.7). The two panels are the same as in Figure 4.4, but plotted over a shorter time range from 04:52 to 05:02 UT. The main feature from panel a-1 and b-1 is that the Poynting flux and photon count are correlated in both time and location. For example, panel a-1, the major brightening occurred after 0456 UT was followed by a minor brightening after 0458 UT. And simultaneously large earthward Poynting flux was observed (see panel b-1). Similarly for RBSP-B, panel a-2 and b-2 showed simultaneous increases and decreases in the auroral brightness and the earthward Poynting flux were very well correlated both spatially

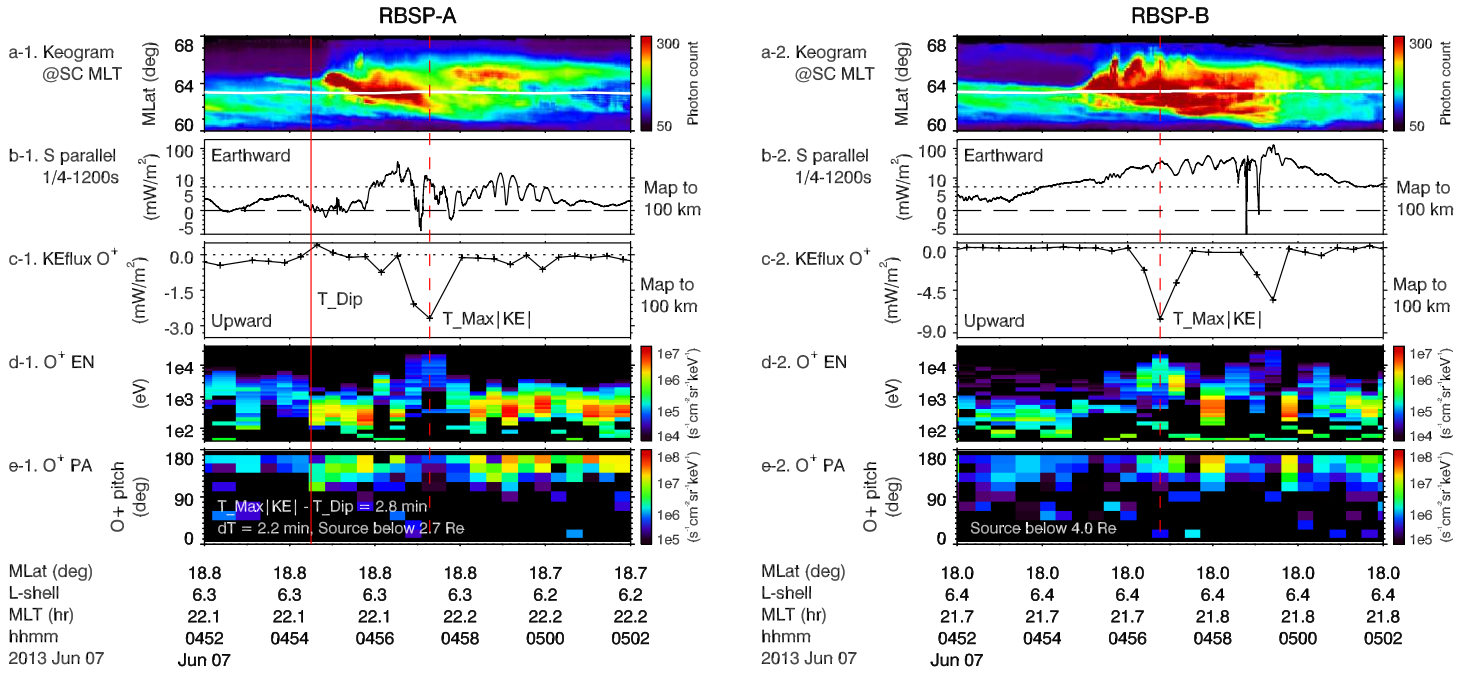

Figure 4.6: Detailed comparisons between the auroral keogram, parallel Poynting flux, and O^+ measurements. The panels for the auroral keogram, the parallel Poynting flux, and O^+ energy spectrogram are the same as in Figure 4.4. Panel c-1 shows the O^+ kinetic energy flux integrated from the measured distributions. Panel d-1 shows the O^+ pitch angle spectrogram. Panel a-2 to e-2 are in the same format for RBSP-B. The vertical red line is the dipolarization time determined from B_z increase. The vertical dashed line indicates the time of the largest upward O^+ kinetic energy flux

and temporally. The correlations seen were also spatial because the keograms were at the spacecraft footpoints. Therefore we conclude that the auroral brightness and the earthward Poynting flux are temporally and spatially correlated. We further argue that the correlation reflects causality, since the Poynting flux was predominantly earthward and large enough to power intense aurora. The earthward Poynting flux reached more than 100 mW/m^2 (panel b-2), which is 2 orders of magnitude larger than the threshold to drive visible aurora.

Although the temporal correlation between the earthward Poynting flux and the auroral brightness is good within a minute, more detailed timing is difficult due to the uncertainty in tracing, especially during a dynamic period like this event. Various empirical models are checked, including T89, T96, T01, T04s, and TS07D. The models all agree on the MLT of the footpoint (dMLT = 0.12 hr). However, the spread of the footpoint MLat predictions is large (dMlat = 4 deg). The T01 model is chosen for tracing and mapping, based on the comparisons between the measured magnetic field at the spacecraft to the modeled fields. As another independent check, we inspect the map of the correlation between the time-varying photon count and the Poynting flux. The high correlation region coincides with the MLT prediction from all the empirical models, and agrees with the MLat predictions from the T01 and T96 models. Based on these comparisons, we argue that the keograms in Figure 4.6 are reliable since all methods give a very similar footpoint MLT, and that the T01 model provides a reasonably good estimation of the spacecraft footpoints. Regardless of the uncertainties in tracing, two important quantities are model independent. The first quantity is the mapping coefficient accounting for the converging field lines. The second quantity is the velocity of the footpoint, or conversely, the auroral motion when mapped to spacecraft location. The comparisons between the aurora motion and the in-situ measurements in Section 4.5 are independent on model choice.

Panels c-1 to e-1 show the O^+ kinetic energy flux, energy spectrogram, and pitch angle spectrogram. A clear O^+ outflow can be seen in the pitch angle spectrogram, where most O^+ were within 45 degrees of the anti-parallel direction. The energy of the out flowing

oxygen ions ranged from about 100 eV up to 10 keV. The high energy suggests that they were energized significantly. The earthward Poynting flux was large enough to account for the upward O^+ kinetic energy flux (panel b-1 and c-1). The comparison hence triggers interest to investigate this possibility. One interesting feature is that for RBSP-A, the time when the kinetic energy flux peaked $T_{Max|KE|}$ was several minutes later than T_{dip}, the dipolarization time identified from B_z increase in Figure 4.4. The time delay could be explained by the travel time of O^+ from the source region of energization. If the oxygen ions were conics (beams are discussed later), we can calculate the travel time based on the in-situ measurements of energy and pitch angle. Using a simple model that includes only adiabatic folding from the mirror force without convection, the time lag ΔT for oxygen ions to reach the spacecraft is

$$\Delta T = \int_0^{\Delta s} \frac{ds}{v\cos\alpha} = \int_0^{\Delta s} \frac{ds}{v\sqrt{1 - B^2(s)/B_0^2}},$$

$$B_0 = B_{SC}/\sin^2\alpha.$$

B_0 is the magnetic field at the source location, where the O^+ were perpendicularly heated. B_{SC} and α are the magnetic field and pitch angle at the spacecraft. $v = \sqrt{2E/m_{O^+}}$ is the speed of the O^+, where E and m are the energy and mass. α is determined from the pitch angle spectrogram and E is determined from the energy spectrogram. Besides the travel time, we can also estimate the upper limit of the source region, which is limited by the pitch angle resolution of HOPE (9 degrees along the magnetic field). As shown in Figure 4.6, the timing lag is consistent with the travel time of the observed O^+, and the source location in altitude and latitude coincides with the auroral acceleration region. Both ion conics and beams could be expected in the upward current region in conjunction with the discrete arc. For those times when the oxygen ions peak at the pitch angle closest to the magnetic field, it is impossible to determine whether the ions are conics or beams. However, since beams travel faster than conics, they would either come from a source region at a lower altitude

or a later time. Neither case would contradict the picture that the earthward Poynting flux provides energy for the oxygen energization.

The HOPE proton channel showed that there was proton outflow in the energy range of several 100 eV to keV (not shown). However it is difficult to estimate the kinetic energy flux for protons Γ_H. The kinetic energy flux is the 4th order of the distribution function and therefore very sensitive to the high energy population. The high energy protons (1-10 keV) of plasma sheet origin are usually counter-streaming in the PSBL. They produce a high noise level, since HOPE does not simultaneously measure the parallel and anti-parallel protons. For the same reason, the electron kinetic energy flux cannot be well calculated neither. Given these constraints, one can only indirectly estimate the proton and electron kinetic energy fluxes. The proton kinetic energy flux is likely to be on the same order of magnitude as the oxygen, which was much smaller than the earthward Poynting flux. This is based on the comparison that the proton outflow had a similar energy dispersion to the oxygen. This is a natural result if the ion acceleration occurs in the upward current region through a parallel potential drop. In the downward current region, perpendicular heating is mostly accounted by the BBELF (broad-band extremely low frequency) waves, simulation showed that BBELF tend to heat ions of different masses to approximately the same energy (Lund et al., 2001). The ions are not broadband in energy, which rules out the possibility of Alfvénic aurora. For the electrons, in-situ passes around the PSBL showed that Γ_e is usually smaller compared to the earthward Poynting flux (e.g. Wygant et al., 2000). This is reasonable for a low-beta plasma like the PSBL, where electromagnetic energy dominates the thermal or kinetic energy of the plasma. Therefore, the earthward Poynting flux is likely to be the most significant energy flux at the PSBL powering the observed auroral acceleration processes.

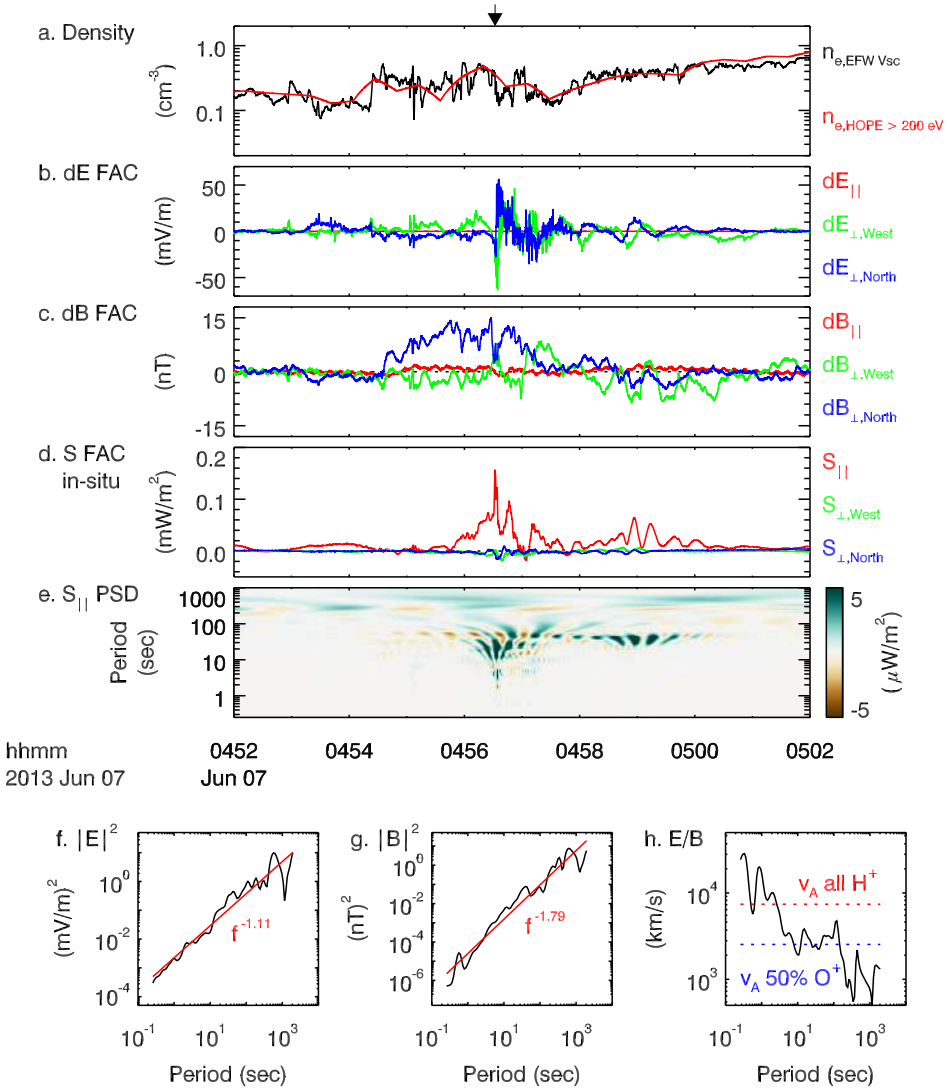

Figure 4.7: Poynting flux and the associated perturbation electromagnetic fields. Panel a is the electron density and is the same as in Figure 4.4. The arrow indicates the time of the largest earthward Poynting flux and the associated density gradient and fluctuations in the electric and magnetic fields. In panels b-d, a field-aligned coordinate system are used where the two perpendicular directions are in the sense of westward and northward in the northern hemisphere. Panel e shows the instantaneous power spectral density (PSD) of the parallel Poynting flux using Morlet wavelet. Panels f and g show the global wavelet spectrum (GWS) for the electromagnetic fields. Panel h shows the E/B ratio as a function of wave period.

4.4 Properties of the Poynting Flux

In this section, we discuss some properties of the observed Poynting flux during this event, which are similar to what is observed in other events in the PSBL. The Poynting flux is predominantly earthward, and concentrated at density gradients. The E/B ratio suggests that the Poynting flux is carried by Alfvénic structures. Most of the electromagnetic energy is transmitted in the range of 10 mHz to 1 Hz in the spacecraft frame. The power spectrum of the magnetic field suggests that the waves may due to turbulence at zero frequency in the plasma frame.

Figure 4.7 shows the Poynting flux and the associated perturbation electromagnetic fields data for RBSP-A. RBSP-B showed the same properties. Panels b and c show the perturbation electric and magnetic fields in a field-aligned coordinate (FAC) system, where the two perpendicular directions are in the sense of westward and northward in the northern hemisphere. The spin-axis electric field is calculated by assuming $\boldsymbol{E} \cdot \boldsymbol{B} = 0$, where $\boldsymbol{B}$ is the background magnetic field. The Poynting flux is calculated according to Equation (B.7),

$$\boldsymbol{S}(p,t) = \alpha \Re\{\boldsymbol{E}(p,t)\} \times \Re\{\boldsymbol{B}(p,t)\},$$

where the time-period spectrograms of the electric and magnetic fields $\boldsymbol{E}(p,t)$ and $\boldsymbol{B}(p,t)$ are obtained using the Morlet wavelet transform. p is the wave period, and $\alpha = 1/400\pi$ mW/(m-mV-nT), for E in mV/m and B in nT. Panel d shows that the Poynting flux was predominantly earthward. The largest earthward Poynting flux was around 04:56:30 UT and indicated by the arrow. The large Poynting flux coincided with the density gradient in panel a and the large fluctuations in the electric and magnetic fields in panels b and c. The spectrogram $S_{\parallel}(p,t)$ in panel e shows that the power was concentrated in the period range from 1 to 100 sec in the spacecraft frame, or equivalently from 10 mHz to 1 Hz. This is consistent with previous observations of the Alfvénic Poynting flux from the Polar spacecraft (Wygant et al., 2000; Dombeck et al., 2005).

The E/B ratio within this period range was comparable to the local Alfvén speed v_A (panel h). The Alfvén speed was about 2500 km/s, using the density from HOPE and the measured local magnetic field. The electron density was estimated as 0.3 cm^{-3} based on the HOPE density in panel b-1 in Figure 4.4, and the H^+ density was comparable to O^+ (not shown). The E/B ratio suggests that the earthward Poynting flux is mainly carried by Alfvén waves. The waves at higher frequencies have an E/B ratio larger than v_A. Thus they were likely to be kinetic Alfvén waves or electrostatic waves. These high frequency waves are efficient in dissipating the electromagnetic energy locally to energize particles (e.g. Lysak and Lotko, 1996). The waves at low frequencies have a E/B ratio of 500 km/s, much smaller than v_A. This value corresponds to a Pedersen conductance $\Sigma_P = 2$ mhos, which is consistent with the typical value of 1-10 mhos (Paschmann et al., 2003). Therefore the low-frequency waves could be due to field-aligned currents which are closed at the ionosphere. Another possibility is that these waves are still Alfvén waves, but the E/B ratio is lowered by reflection off the ionosphere.

The global wavelet spectrum for the electric and magnetic fields are plotted in panels f and h, respectively. The magnetic field spectrum follows a power law of $f_{SC}^{-1.79}$, where f_{SC} is the frequency in the spacecraft frame. A similar power law spectrum was observed along the dayside aurora field lines (Chaston et al., 2008) and the pre-midnight sector (Chaston et al., 2015). They interpreted the spectrum as a Doppler shifted Kolmogorov spectrum of $k^{-5/3}$ (Kolmogorov, 1941) from zero-frequency structures in the plasma frame, where $f_{SC} = \boldsymbol{v}_{rel} \cdot \boldsymbol{k}$ and $\boldsymbol{v}_{rel}$ is the spacecraft velocity in the plasma's rest frame. This interpretation would suggest that the PSBL was turbulent during the event, and that the turbulent cascade was important in dissipating the Alfvénic Poynting flux.

4.5 Auroral Motion and the Dipolarization Propagation

In the previous section, we showed that the earthward Alfvénic Poynting flux and the auroral brightness were directly correlated, and that the ion outflows could be powered by the

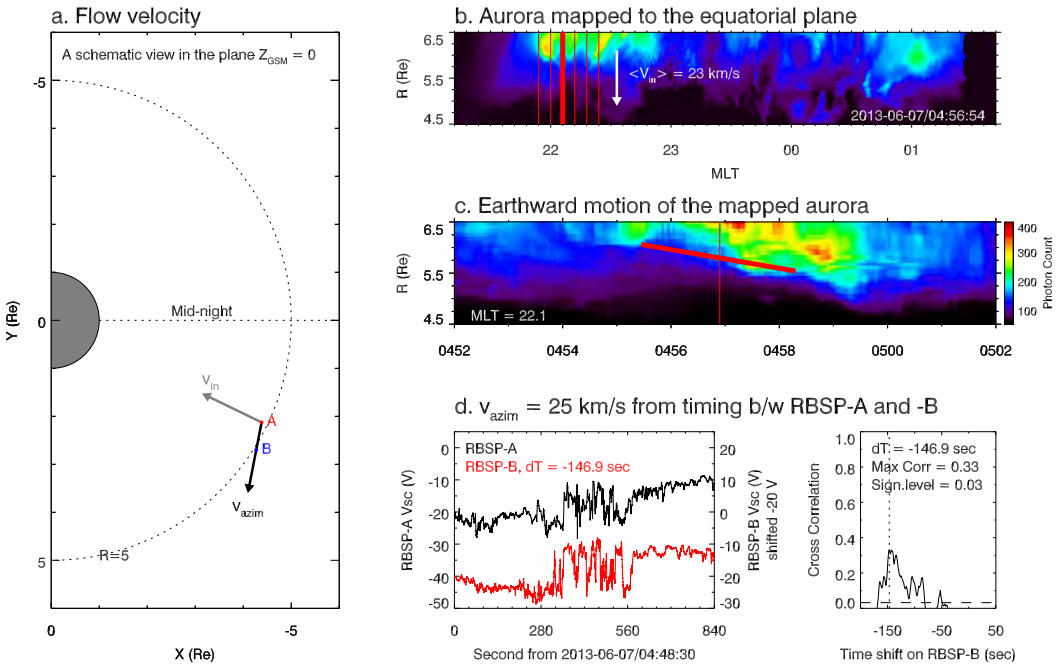

Figure 4.8: Velocities inferred from inter-spacecraft timing and aurora motion. Panel a is a schematic view of the plane of $z_{GSM} = 0$. The inferred azimuthal velocity of the density structure is indicated by the black arrow, pointing from RBSP-A to RBSP-B. The inward radial velocity of the inner edge of the plasma sheet is indicated by the gray arrow. Panel b and c shows the aurora mapped to the equatorial plane, where the equatorward motion in the ionosphere corresponds to the inward motion in the equatorial plane. Panel b shows a snapshot of the aurora at 04:56:54 UT. The vertical lines are the location where aurora motion was tracked. The average velocity was $v_{in} = 23 \pm 2.9$ km/s. Panel c shows one example of the inward motion at the location indicated by the thick line in panel b. The time of the snapshot in panel b is marked by the red vertical line in panel c. The thick red line is added as an eye-guider for the inward motion. There was a sharp jump of the auroral brightness around the photon count of 140, which is chosen to be the threshold for the equatorward boundary of the auroral oval. Panel d shows the details of the westward motion of the density structure, as demonstrated by the cross-correlation between the spacecraft potentials from RBSP-A and RBSP-B. The spacecraft potentials are aligned according to the time lag of 147 ± 10 sec determined by cross-correlation. The westward azimuthal velocity was estimated to be 25 ± 2 km/s. The uncertainty of ± 10 sec is the width of the half maximum of the cross correlation.

Poynting flux. The above results were observed at each of the RBSP spacecraft. In this section, we link the observations between the two spacecraft, to focus on the propagation of the density structure and dipolarization, and to discuss the relation between these parameters. As summarized in Table 4.1, the auroral motion was compared to various velocities derived from the in-situ measurements. Given the direct correlation between the discrete aurora and the earthward Poynting flux and that the dipolarization lead the Poynting flux, it is likely that the auroral westward traveling surge and dipolarization are connected via the earthward Poynting flux. The auroral motion represents the perpendicular propagation of the Alfvén waves. The equatorward boundary of the aurora moved equatorward during the conjunction event, which should correspond to the inward motion of the plasma sheet (Fairfield and Viñas, 1984). Mapping the lower portion of the auroral oval to the equatorial plane shows that the plasma sheet may reach as close as 5 Re from beyond 6.5 Re. The plasma sheet and the associated dipolarization penetrated very deep in the inner magnetosphere.

First, we explain the processes to determine the velocities of the density structure. In this conjunction event, timing between RBSP-A and RBSP-B determines the azimuthal component of the velocity, since the two spacecraft were azimuthally separated in the same L-shell. Specifically, similar density structures based on the spacecraft potential can be observed with a time lag of about 2 min. Panel d in Figure 4.8 shows the spacecraft potential of RBSP-A (black) and of RBSP-B (red) after the proper time shift was applied. The spacecraft potential of RBSP-B was shifted downward by -20V to separate the two curves. The time shift is determined through cross correlation, which shows a significant peak at 147$\pm$10 seconds. The corresponding velocity of the density structure was $v_{azim} = 25\pm2$ km/s along the line between the spacecraft, which was approximately in the azimuthal direction. The uncertainty is determined from the width of the cross correlation at the half maximum. The azimuthal velocity is indicated by the black arrow in panel a in Figure 4.8. The density structure at RBSP-B was slightly broader than at RBSP-A. This may be explained by the slow down of the propagation, or due to temporal changes.

Next, we explain the mapping of the aurora, as illustrated in Figure 4.2. Different from the traditional mapping which maps the whole auroral oval to the equatorial plane (e.g. Lu et al., 2000), the tracing of the upper portion of the auroral oval, which contains the discrete arcs, is stopped at the vertical surface contains the RBSP spacecraft. Therefore the auroral motion in the vertical surface can be directly compared to the in-situ observations time-lagged between RBSP-A and RBSP-B. The motions of the RBSP spacecraft were negligible, since they were near apogee, and thus almost stationary in the near-earth region to monitor the arrival of plasma and waves from deeper in the tail. Another motivation of the special mapping is to reduce the mapping error. For example in Figure 4.3a, the mapping error increases from the spacecraft position to the equatorial plane following the expanding flux tube.

The lower part of the auroral oval containing the equatorward boundary was mapped to the equatorial plane. The equatorward boundary should correspond to the inward boundary of the plasma sheet (Fairfield and Viñas, 1984). Panel b shows a snapshot of the aurora mapped to the equatorial plane, and panel c shows an example of the inward motion of the mapped aurora at a selected MLT. The radial velocity of the plasma sheet is determined to be $v_{in} = 23$ km/s, indicated by the gray arrow in panel a. This velocity is consistent with the velocity of injection sources from previous studies in the inner-magnetosphere (e.g. Moore et al., 1981; Reeves et al., 1996). Panel be also shows that the inner boundary of the plasma sheet penetrated very deep in the inner magnetosphere, from beyond 6.5 Re to as close as 5 Re.

Figure 4.9 plots the upper part of the aurora oval mapped to the vertical surface. The poleward motion of the aurora in the ionosphere corresponds to the upward motion in the vertical surface. The westward motion was $u_{\text{west}} = 148 \pm 20$ km/s, based on the ewograms at the horizontal lines in panel a. An example of the ewogram is shown in panel c, which shows the westward motion along one of the horizontal lines. Note that we focus on the motion of the most westward boundary. The motion of the fine structures eastward to the

	V_{az} (km/s)	Comments
Aurora	148 ± 20	Based on the ewogram mapped to SC location
Dipolarization	120 ± 31 or slower	Time lag of the initial increase in B_z between SC
Density structure	25 ± 2	Time lag of the density structure between SC
E_z/B	about -100	E cross B velocity
$\delta E/\delta B$ 1	about 2500	E/B ratio of the Alfvén wave
$\delta E/\delta B$ 2	about 500	E/B ratio of the FAC
Ionospheric flow	< 10	Typical flow speed mapped to SC location

Table 4.1: Comparisons of various azimuthal velocities. Positive (negative) value represents westward (eastward) motion. See text for details on how the velocities are determined.

boundary (panel c) are out of the scope of this paper. Similarly the upward motion of the most upward (poleward in the ionosphere) boundary was $u_{\rm up} = 132 \pm 14$ km/s based on the keogram at the vertical lines in panel b. Panel d shows an example at the location of 22.9 MLT, marked by the thick vertical line in panel b. Note that the westward and upward velocities are determined for the boundary of the most poleward aurora (panel a and b). There were fine structures equatorward of the boundary moving at different velocities (panel c and d), but they are out of the scope of this paper. One interesting feature is that the most bright aurora was stable around $Z_{GSM} = 3$ Re. Given the observations that the most intense Poynting flux was concentrated at the density gradients and that the Poynting flux and the aurora brightness were very well correlated, the location of the brightest aurora may reflect a density gradient around $Z_{GSM} = 3$ Re with the width of about 0.3 Re in the vertical surface.

Based on the velocity comparisons in Table 4.1, we suggest that the auroral westward traveling surge may be controlled by sources in the magnetosphere, possibly by the propagation of the slow mode or the perpendicular propagation of the shear mode. The auroral motion was much faster than the ionospheric flows and therefore is unlikely to be driven by low-altitude sources. The Alfvén wave had a faster parallel phase velocity, but the perpen-

dicular phase velocity could be relevant if $k_\perp \gg k_\parallel$. Another possibility is the slow mode, which has a much slower velocity than the Alfvén waves in the PSBL. In the MHD simulation by Ebihara and Tanaka (2015), the slow mode is about 150 km/s at the PSBL. The dipolarization may represent the propagation of the MHD waves. As shown in Figure 4.4, if the initial increase in B_z at RBSP-B is assumed as the dipolarization signature, the cross correlation analysis gives a time lag of 27 ± 7 sec, which corresponds to an azimuthal velocity of $w_{\mathrm{west}} = 120 \pm 31$ km/s. However, if the second increase in B_z at RBSP-B is used, the dipolarization propagation speed is comparable to the density structure and therefore too slow to explain the auroral motion. Wavelets of the electric and magnetic field waveforms (Figure 4.7) were utilized to determine the phase velocity as a function of period. The MHD Alfvén waves had an E/B ratio of about 2500 km/s. These waves were the primary carrier of the earthward Poynting flux. At larger periods, the E/B ratio fluctuated around 500 km/s. As discussed in Section 4.4, the value represents either field-aligned current or reflected Alfvén waves. Furthermore, if the electric field were interpreted to be due to convection, the azimuthal velocity due to $\boldsymbol{E} \times \boldsymbol{B}$ would be eastward and smaller than 100 km/s for 04:55 to 04:56 UT, when the auroral westward surge was identified. Finally, typical ionospheric flows are 0.1-1 km/s, which is less than 10 km/s when mapped to the spacecraft locations.

The auroral westward traveling surge (WTS) has been extensively studied at ionospheric and low altitudes (e.g. Opgenoorth et al., 1983; Marklund et al., 1998). However, to our knowledge, this paper is the first conjunction between the WTS and multiple high-altitude. Previous studies have shown that typical WTS velocities are 1-10 km/s at the ionosphere (Paschmann et al., 2003). Based on ground and low-altitude observations (Opgenoorth et al., 1983; Marklund et al., 1998), WTS are usually associated with strong upward field-aligned currents. In the classical picture of the auroral physics, the upward field-aligned currents are associated with the quasi-static potential drop (McFadden et al., 1999b,a), which resulted in the so-called inverted-V aurora. However, the generation and propagation mechanisms of WTS are still not well determined (Sato et al., 2015), and the free energy source for

establishing the quasi-static potential drop has not been identified. The WTS observed in the conjunction event reported in this paper was among the fastest ones, at 15.6 km/s at the ionosphere. The WTS is usually propagating significantly faster than the surrounding plasma drift velocities, and therefore (Opgenoorth et al., 1983) inferred based on a velocity argument that the WTS may be related to the perpendicular propagation of magnetosonic waves in the magnetosphere. In this paper, we provide the some evidence on the relationship between the WTS and the possible drivers in the magnetosphere. In addition, the correlation between the auroral brightness and the Alfvénic Poynting flux implies that the WTS and the associated quasi-static potential drop may be powered by Alfvén waves. Therefore the observation suggests that the Alfvén waves may play a more important role than previously thought. In addition to the previously established relation between Alfvén waves and the Alfvénic aurora (Wygant et al., 2000, 2002; Chaston et al., 2002), Alfvén waves may also power the quasi-static potential drop and therefore the inverted-V aurora. Theoretical studies on establishing inverted-V structures through Alfvén waves include Lysak (1985, 1990). In the case of current-driven system at small scales, quasi-static potential drop can arise due to the reflection of Alfvén waves. Goertz (1984); Lysak (1998) suggested that the so-called electrostatic shocks can be the signatures of narrow scale inertial Alfvén waves.

4.6 Discussions and Conclusions

During the event on June 07 2013, both RBSP spacecraft were in conjunction with the THEMIS all-sky imager at the PINA site. At each RBSP spacecraft, a good temporal and spatial correlation was observed between the in-situ Poynting flux and the ground auroral brightness. The Poynting flux was predominantly earthward and on the order of 100 mW/m^2 mapped to 100 km altitude, which is large enough to power the brightest aurora. These observations provide strong evidence for the causality that the discrete aurora in this event was powered by the earthward Poynting flux. Further inspections show that the earthward Poynting flux was carried by Alfvén waves in the frequency range of 1 mHz-1Hz in the

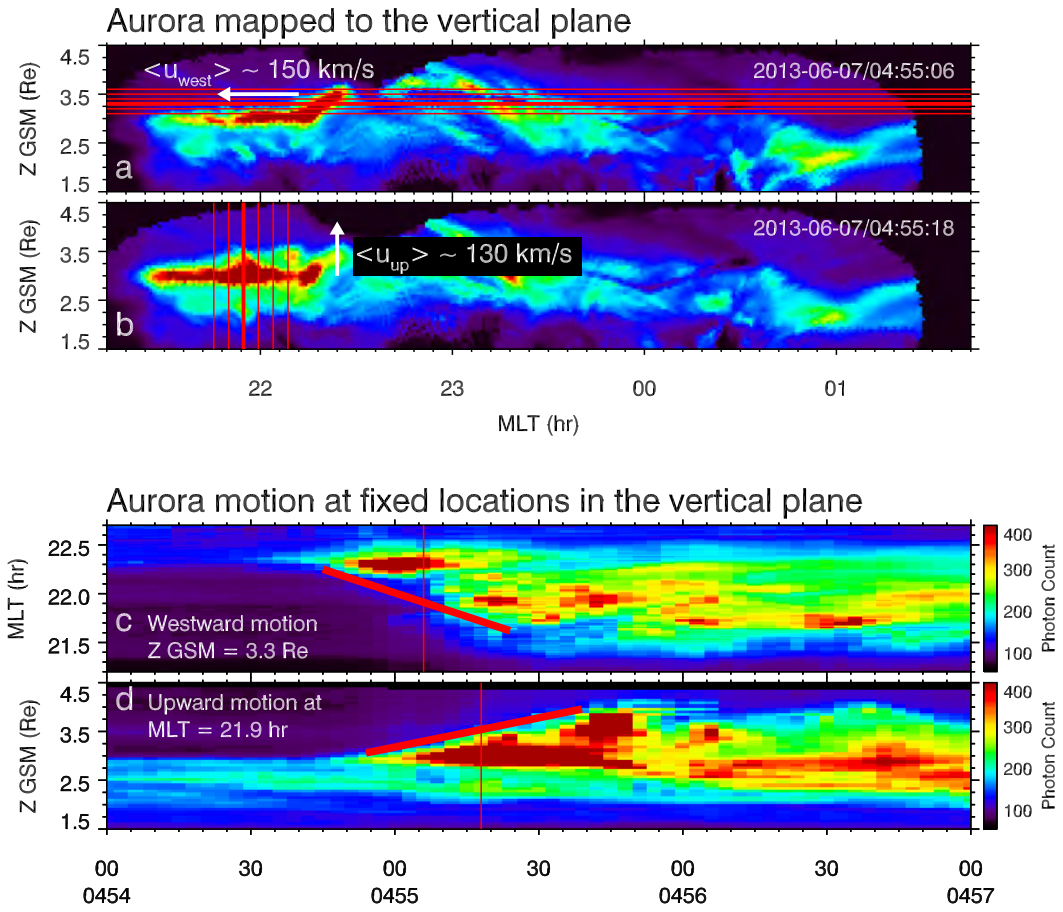

Figure 4.9: The poleward and westward motions of the most poleward aurora mapped to the vertical surface at the constant distance of $R \simeq 5$. These motions correspond to the upward and westward motions in the vertical surface. The threshold for the most poleward boundary is the photon count of 140, the same as the value used to determine the equatorward boundary. Panel a and b show two snapshots of the aurora mapped to the vertical plane. The westward motion of $u_{west} = 148 \pm 20$ km/s is calculated from the aurora motion at the horizontal lines in panel a. Similarly the $u_{up} = 132 \pm 14$ km/s is calculated from the aurora motion at the vertical lines in panel b. The westward motion is determined from 04:54:45 to 04:55:24 UT. The upward motion is determined from 04:54:54 to 04:55:39 UT. Panel c shows the ewogram at the location of the thick horizontal line in panel a. The ewogram shows the east-west auroral motion along certain latitude. In panel c, the thick line serves as the guide for eye on the westward motion of the most westward aurora. There were fine structures eastward to the most westward boundary and moved at different velocities. These motions are out of the scope of this paper, because we focus on the westward propagation of the aurora, which is the propagation of the westward edge of the fine structures. Similarly, the poleward motion of the most poleward aurora is shown in panel d. This kind of plot is called the keogram, which focuses on the north-south auroral motion along certain local time.

spacecraft frame. The Poynting flux was concentrated at the density gradients around the PSBL. The direct correlation between the auroral brightness and the Alfvénic Poynting flux and velocity comparisons suggest that the WTS may represent the propagation of MHD waves. There was also a density structure propagated westward at about 30 km/s, which may be the signature of a localized plasma flow or surface waves around the PSBL. As the ionospheric feedback, oxygen outflows were observed at the RBSP spacecraft after the dipolarization. Timing and energy balance analysis suggest that the outflows were likely to be powered by the earthward Poynting flux from below the auroral acceleration region. Implied from the equatorward motion of the auroral oval, the plasma sheet moved inward at about 30 km/s from beyond 6.5 Re to as deep as 5 Re in the equatorial plane.

These results are very interesting because it connects the low-altitude auroral observations and the mid-tail observations. The low-altitude studies have established that the WTS is associated with strong upward FAC (Opgenoorth et al., 1983; Marklund et al., 1998), and therefore the quasi-static potential drop (McFadden et al., 1999b,a). On the other hand, the localized BBFs (bursty bulk flows) are shown to be the most important transportation mechanism in the mid-tail (Baumjohann et al., 1990; Angelopoulos et al., 1992, 1994). At the position of the RBSP, we established the connection between the Alfvénic Poynting flux and the discrete aurora in the inner magnetosphere. The aurora brightness and the Poynting flux are correlated and the propagation speeds match. Therefore, we propose two future studies to explore the causal chain of the auroral physics. The first study is the conjunction between RBSP in the inner magnetosphere and THEMIS in the mid-tail, when all the spacecraft were in conjunction with the ground aurora and magnetic field observations. The purpose of the study is to examine the role of plasma flow and its braking and the Alfvén waves generation mechanism. A possible scenario based on previous studies and the observations in this paper is that the flow braking occurring in the inner magnetosphere releases energy and launches compressional mode waves, which propagate as dipolarization and undergo mode conversion/phase mixing at the density gradients around the PSBL. The

shear mode waves are generated and radiate electromagnetic energy in the form of earthward Poynting flux. Another possible scenario is that the Poynting flux and the Alfvénic Poynting flux are generated directly from the reconnection site (Dai, 2009; Dai et al., 2011; Duan et al., 2016). They propagate earthward mainly in the PSBL and carry surface waves which may appear as density structures to in-situ spacecraft. The proposed conjunction study between RBSP and THEMIS can therefore evaluate the contribution of the different possibilities from direct observations and provide more information on the Alfvén wave generation mechanism. The second study is the conjunction between the RBSP, low-altitude spacecraft, and the ground aurora. Previous studies have shown that the Alfvénic aurora is powered by the Alfvénic Poynting flux. However, the free energy source for establishing the quasi-static potential drop is unclear. Although the observations in this study show the connection between the WTS and the Alfvén wave, the details in the auroral acceleration is missing. Given the previous studies on that the auroral WTS is associated with the upward FAC (Opgenoorth et al., 1983; Marklund et al., 1998) and that the upward FAC is associated with the quasi-static potential drop (inverted-V aurora) (McFadden et al., 1999b,a), it is likely that the WTS is in conjunction with the quasi-static potential drop, and therefore the quasi-static potential drop may also be powered by the Alfvén wave. With the help of low-altitude spacecraft, direct observations on the electron distribution can determine whether the aurora arc associated with WTS is Alfvénic or inverted-V, and the local magnetic field can be used to infer the FAC. Such information would be crucial in discussing the acceleration mechanism through which the Alfvén waves are dissipated. In addition, the Poynting flux may also power other auroral forms. For example, in some of the RBSP events, there were dipolarizations associated with Poynting flux propagated eastward which may correspond to the eastward propagating auroras (Nakamura et al., 1993).

Chapter 5

Conclusions

In this thesis, we focused on the dayside cusp and the nightside auroral region, where enhanced Poynting flux flows earthward during geomagnetic active periods Keiling et al. (2003). For the dayside cusp, we combine the measurements from the Polar and FAST spacecraft to cover the altitude range of 1.3 to about 6 Re geocentric distance. By comparing the energy fluxes including the Poynting flux, electron kinetic energy flux and ion kinetic energy flux in both quasi-conjunction cases and statistical survey, we reached the following conclusions:

1. A surprisingly energetic wind is observed in the mid-altitude cusp (about 3-6 Re) during geomagnetic active times. The ion kinetic energy flux is upward and can be several 10 mW/m^2 and more than 100 mW/m^2 in extreme cases. These values are comparable to the energy flux which causes the most bright aurora and much larger than those observed on the night side.

2. The ion outflow carries almost all the kinetic energy of the energetic wind, in the sense that the ion kinetic energy flux is much larger than the electron kinetic energy flux. The ion outflow in the mid-altitude cusp usually consists of ions in the energy range from several 100 eV to several 1 keV. O^+ ions are usually a significant in terms of mass density and sometimes number density, suggesting an ionospheric origin of the wind.

3. Comparisons between the ion kinetic energy flux at low-altitude and mid-altitude show that the main ion energization occur in the mid-altitude. Strangeway et al. (2005) studied the driving of ion outflows in the low-altitude cusp and showed that the number flux of the ion outflow is correlated with the Poynting flux and precipitating electrons. This is the first stage for creating the energetic wind. Our observations show that at low-altitude, the ion kinetic energy flux is small even when the number flux of the ion outflow is large. Therefore the intense ion energization is required as the second stage.

4. Comparisons between all the energy fluxes suggest that the earthward Poynting flux flowing into the mid-altitude cusp is the only possible energy source for the ion energization. The electron kinetic energy flux in the mid-altitude cusp is much smaller than the Poynting flux and usually upward when intense ion outflow is observed. Therefore the electron is excluded as an energy source. Comparisons between the electron kinetic energy in mid-altitude and low-altitude implies that the electrons are accelerated earthward in the mid-altitude cusp. The altitude profile of the Poynting flux is consistent with the scenario where the electromagnetic energy of the Poynting flux is converted to energize ions upward and electrons downward. The remaining Poynting flux and the downward electrons flow into the ionosphere, where they drive the ion outflow as suggested by Strangeway et al. (2005).

5. Various ion energization mechanisms have been suggested in the literature. Although our study is not directly related to these previous studies, we are able to place several constraints on the possible mechanisms based on our observations. The ultimate free energy source is the Poynting flux. The energy conversion has to be efficient and electrons are energized along with the ions. The ion energization is primarily perpendicular heating.

In the second part, we studied the connection between the nightside aurora and the Poynting

flux. In the conjunction event on June 07 2013, both RBSP spacecraft were in conjunction with a discrete aurora arc in the pre-midnight sector. We found the following results and conclusions:

1. At each of the RBSP spacecraft, we found a good temporal and spatial correlation between the Poynting flux and the auroral brightness around the footpoint of the spacecraft. We argue that the correlation implies causality since the Poynting flux is predominantly earthward and large enough to power the brightest aurora. Oxygen outflows were observed. The oxygen kinetic energy flux was on the order of 1% of the earthward Poynting flux and is likely to be powered by the Poynting flux.

2. The Poynting flux was predominantly earthward and concentrated at density gradients around the plasma sheet boundary layer (PSBL). The Poynting flux was transmitted in the frequency range from 10 mHz to 1 Hz in the form of Alfvén waves. The associated magnetic field perturbation had a Kolmogorov-like spectrum with the index of 5/3.

3. Dipolarization signatures (about 8 nT increase in GSM B_z) were observed at both spacecraft right before the Poynting flux enhancement. Inter-spacecraft timing suggests that the dipolarization propagated a the speed of 120 ± 31 km/s (or slower) along the spacecraft separation, which was approximately in the westward azimuthal direction. Similarly, a density structure was identified to propagate westward at 25 ± 2 km/s.

4. To compare the aurora motion to the in-situ measurements, we map the aurora to a vertical surface at the distance of 5 Re containing the RBSP spacecraft. On this surface, the auroral poleward expansion corresponds to an northward motion (along GSM Z) and the auroral westward traveling surge (WTS) corresponds to a westward motion. By following these motions around the spacecraft location, we determined that the poleward motion was 132 ± 14 km/s and the westward motion was 148 ± 20 km/s. In addition, the equatorward motion of the aurora indicated the inward motion of the plasma sheet at 23 ± 3 km/s from beyond 6.5 Re to as close as 5 Re in the equatorial

plane.

5. We report the first conjunction between the WTS and high-altitude spacecraft. Based on the correlation between the Poynting flux and the auroral brightness and comparisons between the velocities of WTS and various possible sources, we suggest that the WTS may represent the propagation of MHD waves in the magnetosphere, in the form of perpendicular propagation of the Alfvén waves or the propagation of slow mode.

References

Abe, T., Whalen, B. A., Yau, A. W., Horita, R. E., Watanabe, S., and Sagawa, E. (1993). EXOS D (Akebono) suprathermal mass spectrometer observations of the polar wind. *Journal of Geophysical Research: Space Physics*, 98(A7):11191–11203.

Akasofu, S.-I. (1964). The development of the auroral substorm. *Planetary and Space Science*, 12(4):273 – 282.

Allan, W. and Wright, A. N. (2000). Magnetotail waveguide: Fast and Alfvén waves in the plasma sheet boundary layer and lobe. *Journal of Geophysical Research: Space Physics*, 105(A1):317–328.

André, M., Crew, G. B., Peterson, W. K., Persoon, A. M., Pollock, C. J., and Engebretson, M. J. (1990). Ion heating by broadband low-frequency waves in the cusp/cleft. *Journal of Geophysical Research: Space Physics*, 95(A12):20809–20823.

Angelopoulos, V., Baumjohann, W., Kennel, C. F., Coroniti, F. V., Kivelson, M. G., Pellat, R., Walker, R. J., Lühr, H., and Paschmann, G. (1992). Bursty bulk flows in the inner central plasma sheet. *Journal of Geophysical Research: Space Physics*, 97(A4):4027–4039.

Angelopoulos, V., Kennel, C. F., Coroniti, F. V., Pellat, R., Kivelson, M. G., Walker, R. J., Russell, C. T., Baumjohann, W., Feldman, W. C., and Gosling, J. T. (1994). Statistical characteristics of bursty bulk flow events. *Journal of Geophysical Research: Space Physics*, 99(A11):21257–21280.

Angelopoulos, V., Mozer, F. S., Bonnell, J., Temerin, M., Somoza, M., Peterson, W. K., Collin, H. L., and Giles, B. (2001). Wave power studies of cusp crossings with the Polar satellite. *Journal of Geophysical Research: Space Physics*, 106(A4):5987–6006.

Baumjohann, W., Paschmann, G., and Lühr, H. (1990). Characteristics of high-speed ion flows in the plasma sheet. *Journal of Geophysical Research: Space Physics*, 95(A4):3801–3809.

Baumjohann, W. and Treumann, R. A. (1997). *Basic Space Plasma Physics*. Imperial College Press.

Bellan, P. (2008). *Fundamentals of Plasma Physics*. Cambridge University Press.

Bouhram, M., Klecker, B., Miyake, W., Rème, H., Sauvaud, J.-A., Malingre, M., Kistler, L., and Blagau, A. (2004). On the altitude dependence of transversely heated O+ distributions in the cusp/cleft. *Annales Geophysicae*, 22(5):1787–1798.

Bryant, D. (1998). *Electron Acceleration in the Aurora and Beyond*. Taylor & Francis.

Burch, J. L. (1973). Rate of erosion of dayside magnetic flux based on a quantitative study of the dependence of polar cusp latitude on the interplanetary magnetic field. *Radio Science*, 8(11):955–961.

Burch, J. L. (2000). IMAGE mission overview. *Space Science Reviews*, 91(1):1–14.

Cargill, P. J., Lavraud, B., Owen, C. J., Grison, B., Dunlop, M. W., Cornilleau-Wehrlin, N., Escoubet, C. P., Paschmann, G., Phan, T. D., Rezeau, L., Bogdanova, Y., and Nykyri, K. (2005). Cluster at the Magnetospheric Cusps. volume 20 of *Space Sciences Series of ISSI*, pages 321–366. Springer Netherlands.

Carlson, C. W., McFadden, J. P., Turin, P., Curtis, D. W., and Magoncelli, A. (2001). The Electron and ion Plasma Experiment for Fast. *Space Science Reviews*, 98(1):33–66.

Chang, T. (1993). Lower-hybrid collapse, caviton turbulence, and charged particle energization in the topside auroral ionosphere and magnetosphere. *Physics of Fluids B: Plasma Physics*, 5(7):2646–2656.

Chang, T., Crew, G. B., Hershkowitz, N., Jasperse, J. R., Retterer, J. M., and Winningham, J. D. (1986). Transverse acceleration of oxygen ions by electromagnetic ion cyclotron resonance with broad band left-hand polarized waves. *Geophysical Research Letters*, 13(7):636–639.

Chappell, C. R., Giles, B. L., Moore, T. E., Delcourt, D. C., Craven, P. D., and Chandler, M. O. (2000). The adequacy of the ionospheric source in supplying magnetospheric plasma. *Journal of Atmospheric and Solar-Terrestrial Physics*, 62(6):421–436.

Chaston, C. C., Bonnell, J. W., Carlson, C. W., McFadden, J. P., Ergun, R. E., and Strangeway, R. J. (2003). Properties of small-scale Alfvén waves and accelerated electrons from FAST. *Journal of Geophysical Research: Space Physics*, 108(A4):8003.

Chaston, C. C., Bonnell, J. W., Kletzing, C. A., Hospodarsky, G. B., Wygant, J. R., and Smith, C. W. (2015). Broadband low-frequency electromagnetic waves in the inner magnetosphere. *Journal of Geophysical Research: Space Physics*, 120(10):8603–8615.

Chaston, C. C., Bonnell, J. W., Peticolas, L. M., Carlson, C. W., McFadden, J. P., and Ergun, R. E. (2002). Driven Alfven waves and electron acceleration: A FAST case study. *Geophysical Research Letters*, 29(11):30–34.

Chaston, C. C., Salem, C., Bonnell, J. W., Carlson, C. W., Ergun, R. E., Strangeway, R. J., and McFadden, J. P. (2008). The Turbulent Alfvénic Aurora. *Phys. Rev. Lett.*, 100(17):175003.

Crooker, N. U., Berchem, J., and Russell, C. T. (1987). Cusp displacement at the magnetopause for large IMF Y component. *Journal of Geophysical Research: Space Physics*, 92(A12):13467–13471.

Daglis, I. A., Thorne, R. M., Baumjohann, W., and Orsini, S. (1999). The terrestrial ring current: Origin, formation, and decay. *Reviews of Geophysics*, 37(4):407–438.

Dai, L. (2009). Collisionless Magnetic Reconnection via Alfvén Eigenmodes. *Phys. Rev. Lett.*, 102(24):245003.

Dai, L., Wygant, J. R., Cattell, C., Dombeck, J., Thaller, S., Mouikis, C., Balogh, A., and Rème, H. (2011). Cluster observations of surface waves in the ion jets from magnetotail reconnection. *Journal of Geophysical Research: Space Physics*, 116(A12):n/a—-n/a.

Dombeck, J., Cattell, C. A., Wygant, J. R., Keiling, A., and Scudder, J. (2005). Alfvén waves and Poynting flux observed simultaneously by Polar and FAST in the plasma sheet boundary layer. *J. Geophys. Res.*, 110(A12):A12S90.

Duan, S. P., Dai, L., Wang, C., Liang, J., Lui, A. T. Y., Chen, L. J., He, Z. H., Zhang, Y. C., and Angelopoulos, V. (2016). Evidence of kinetic Alfvén eigenmode in the near-Earth magnetotail during substorm expansion phase. *Journal of Geophysical Research: Space Physics*, pages n/a—-n/a.

Dungey, J. W. (1961). Interplanetary Magnetic Field and the Auroral Zones. *Phys. Rev. Lett.*, 6(2):47–48.

Eastman, T. E., Frank, L. A., Peterson, W. K., and Lennartsson, W. (1984). The plasma sheet boundary layer. *Journal of Geophysical Research: Space Physics*, 89(A3):1553–1572.

Eastman, T. E., Hones, E. W., Bame, S. J., and Asbridge, J. R. (1976). The magnetospheric boundary layer: Site of plasma, momentum and energy transfer from the magnetosheath into the magnetosphere. *Geophysical Research Letters*, 3(11):685–688.

Ebihara, Y. and Tanaka, T. (2015). Substorm simulation: Formation of westward traveling surge. *Journal of Geophysical Research: Space Physics*, 120(12):10,410–466,484.

Elphic, R. C., Means, J. D., Snare, R. C., Strangeway, R. J., Kepko, L., and Ergun, R. E. (2001). Magnetic field instruments for the Fast Auroral Snapshot explorer. *Space Science Reviews*, 98(1-2):151–168.

Ergun, R. E., Andersson, L., Tao, J., Angelopoulos, V., Bonnell, J., McFadden, J. P., Larson, D. E., Eriksson, S., Johansson, T., Cully, C. M., Newman, D. N., Goldman, M. V., Roux, A., LeContel, O., Glassmeier, K.-H., and Baumjohann, W. (2009). Observations of Double Layers in Earth's Plasma Sheet. *Phys. Rev. Lett.*, 102(15):155002.

Ergun, R. E., Carlson, C. W., Mozer, F. S., Delory, G. T., Temerin, M., McFadden, J. P., Pankow, D., Abiad, R., Harvey, P., Wilkes, R., Primbsch, H., Elphic, R., Strangeway, R., Pfaff, R., and Cattell, C. A. (2001). The FAST Satellite Fields Instrument. *Space Science Reviews*, 98(1):67–91.

Ergun, R. E., Goodrich, K. A., Stawarz, J. E., Andersson, L., and Angelopoulos, V. (2015). Large-amplitude electric fields associated with bursty bulk flow braking in the Earth's plasma sheet. *Journal of Geophysical Research: Space Physics*, 120(3):1832–1844.

Fairfield, D. H. and Viñas, A. F. (1984). The inner edge of the plasma sheet and the diffuse aurora. *Journal of Geophysical Research: Space Physics*, 89(A2):841–854.

Frank, L. A. (1971). Plasma in the Earth's Polar Magnetosphere. *J. Geophys. Res.*, 76(22):5202–5219.

Frank, L. A., Sigwarth, J. B., Craven, J. D., Cravens, J. P., Dolan, J. S., Dvorsky, M. R., Hardebeck, P. K., Harvey, J. D., and Muller, D. W. (1995). The visible imaging system (VIS) for the polar spacecraft. *Space Science Reviews*, 71(1):297–328.

Goertz, C. K. (1984). Kinetic Alfvén waves on auroral field lines. *Planetary and Space Science*, 32(11):1387 – 1392.

Harvey, P., Mozer, F. S., Pankow, D., Wygant, J. R., Maynard, N. C., Singer, H., Sullivan, W., Anderson, P. B., Pfaff, R., Aggson, T., Pedersen, A., Fälthammar, C.-G., and

Tanskannen, P. (1995). The electric field instrument on the polar satellite. *Space Science Reviews*, 71(1-4):583–596.

Heikkila, W. J. and Winningham, J. D. (1971). Penetration of Magnetosheath Plasma to Low Altitudes through the Dayside Magnetospheric Cusps. *J. Geophys. Res.*, 76(4):883–891.

Hultqvist, B. (1991). On the motion of electrons in the slow electric field fluctuations observed by Viking. *Journal of Geophysical Research: Space Physics*, 96(A11):19513–19519.

Jackson, J. D. (1999). *Classical electrodynamics*. Wiley, New York, {NY}, 3rd ed. edition.

Jones, D. L. and Baraniuk, R. G. (1991). Efficient approximation of continuous wavelet transforms. *Electronics Letters*, 27(9):748–750.

Keiling, A., Wygant, J. R., Cattell, C. A., Mozer, F. S., and Russell, C. T. (2003). The Global Morphology of Wave Poynting Flux: Powering the Aurora. *Science*, 299(5605):383–386.

Kistler, L. M., Mouikis, C., Möbius, E., Klecker, B., Sauvaud, J. A., Réme, H., Korth, A., Marcucci, M. F., Lundin, R., Parks, G. K., and Balogh, A. (2005). Contribution of nonadiabatic ions to the cross-tail current in an O+ dominated thin current sheet. *Journal of Geophysical Research: Space Physics*, 110(A6):n/a—-n/a.

Klumpar, D. M., Möbius, E., Kistler, L. M., Popecki, M., Hertzberg, E., Crocker, K., Granoff, M., Tang, L., Carlson, C. W., McFadden, J., Klecker, B., Eberl, F., Künneth, E., Kästle, H., Ertl, M., Peterson, W. K., Shelly, E. G., and Hovestadt, D. (2001). *The Time-of-Flight Energy, Angle, Mass Spectrograph (Teams) Experiment for Fast*, pages 197–219. Springer Netherlands, Dordrecht.

Kolmogorov, A. N. (1941). Dissipation of energy in locally isotropic turbulence. In *Dokl. Akad. Nauk SSSR*, volume 32, pages 16–18.

Lavraud, B. and Cargill, P. J. (2005). Cluster reveals the magnetospheric cusps. *Astronomy & Geophysics*, 46(1):1.32–1.35.

Lavraud, B., Fedorov, A., Budnik, E., Thomsen, M. F., Grigoriev, A., Cargill, P. J., Dunlop, M. W., Rème, H., Dandouras, I., and Balogh, A. (2005). High-altitude cusp flow dependence on IMF orientation: A 3-year Cluster statistical study. *J. Geophys. Res.*, 110(A2):A02209.

Liu, Y., Liang, X. S., and Weisberg, R. H. (2007). Rectification of the Bias in the Wavelet Power Spectrum. *Journal of Atmospheric and Oceanic Technology*, 24(12):2093–2102.

Lockwood, M., Chandler, M. O., Horwitz, J. L., Waite, J. H., Moore, T. E., and Chappell, C. R. (1985a). The cleft ion fountain. *Journal of Geophysical Research: Space Physics*, 90(A10):9736–9748.

Lockwood, M., Moore, T. E., Waite, J. H., Chappell, C. R., Horwitz, J. L., and Heelis, R. A. (1985b). The geomagnetic mass spectrometer—mass and energy dispersions of ionospheric ion flows into the magnetosphere. *Nature*, 316:612–613.

Lu, G., Brittnacher, M., Parks, G., and Lummerzheim, D. (2000). On the magnetospheric source regions of substorm-related field-aligned currents and auroral precipitation. *Journal of Geophysical Research: Space Physics*, 105(A8):18483–18493.

Lund, E. J., Möbius, E., Lynch, K. A., Klumpar, D. M., Peterson, W. K., Ergun, R. E., and Carlson, C. W. (2001). On the mass dependence of transverse ion acceleration by broad-band extremely low frequency waves. *Physics and Chemistry of the Earth, Part C: Solar, Terrestrial & Planetary Science*, 26(1):161–163.

Lundin, R. and Hultqvist, B. (1989). Ionospheric plasma escape by high-altitude electric fields: Magnetic moment "pumping". *Journal of Geophysical Research: Space Physics*, 94(A6):6665–6680.

Lysak, R. L. (1985). Auroral electrodynamics with current and voltage generators. *Journal of Geophysical Research: Space Physics*, 90(A5):4178–4190.

Lysak, R. L. (1990). Electrodynamic coupling of the magnetosphere and ionosphere. *Space Science Reviews*, 52(1-2):33–87.

Lysak, R. L. (1998). The relationship between electrostatic shocks and kinetic Alfvén waves. *Geophys. Res. Lett.*, 25(12):2089–2092.

Lysak, R. L., Hudson, M. K., and Temerin, M. (1980). Ion heating by strong electrostatic ion cyclotron turbulence. *Journal of Geophysical Research: Space Physics*, 85(A2):678–686.

Lysak, R. L. and Lotko, W. (1996). On the kinetic dispersion relation for shear Alfvén waves. *J. Geophys. Res.*, 101(A3):5085–5094.

Lysak, R. L., Song, Y., and Jones, T. W. (2009). Propagation of Alfvén waves in the magnetotail during substorms. *Annales Geophysicae*, 27(5):2237–2246.

Marklund, G. T., Karlsson, T., Blomberg, L. G., Lindqvist, P.-A., Fälthammar, C.-G., Johnson, M. L., Murphree, J. S., Andersson, L., Eliasson, L., Opgenoorth, H. J., and Zanetti, L. J. (1998). Observations of the electric field fine structure associated with the westward traveling surge and large-scale auroral spirals. *Journal of Geophysical Research: Space Physics*, 103(A3):4125–4144.

McFadden, J. P., Carlson, C. W., and Ergun, R. E. (1999a). Microstructure of the auroral acceleration region as observed by FAST. *Journal of Geophysical Research: Space Physics*, 104(A7):14453–14480.

McFadden, J. P., Carlson, C. W., Ergun, R. E., Klumpar, D. M., and Moebius, E. (1999b). Ion and electron characteristics in auroral density cavities associated with ion beams: No evidence for cold ionospheric plasma. *Journal of Geophysical Research: Space Physics*, 104(A7):14671–14682.

Mende, S. B., Harris, S. E., Frey, H. U., Angelopoulos, V., Russell, C. T., Donovan, E., Jackel, B., Greffen, M., and Peticolas, L. M. (2008). The THEMIS Array of Ground-based Observatories for the Study of Auroral Substorms. *Space Science Reviews*, 141(1):357.

Mende, S. B., Heetderks, H., Frey, H. U., Lampton, M., Geller, S. P., Abiad, R., Siegmund, O. H. W., Tremsin, A. S., Spann, J., Dougani, H., Fuselier, S. A., Magoncelli, A. L., Bumala, M. B., Murphree, S., and Trondsen, T. (2000). Far ultraviolet imaging from the IMAGE spacecraft. 2. Wideband FUV imaging. *Space Science Reviews*, 91(1):271–285.

Meng, C.-I. (1982). Latitudinal variation of the polar cusp during a geomagnetic storm. *Geophysical Research Letters*, 9(1):60–63.

Miyake, W., Mukai, T., and Kaya, N. (1993). On the evolution of ion conics along the field line from EXOS D observations. *Journal of Geophysical Research: Space Physics*, 98(A7):11127–11134.

Moore, T. E., Arnoldy, R. L., Feynman, J., and Hardy, D. A. (1981). Propagating substorm injection fronts. *Journal of Geophysical Research: Space Physics*, 86(A8):6713–6726.

Moore, T. E., Lundin, R., Alcaydé, D., André, M., Ganguli, S. B., Temerin, M., and Yau, A. W. (1999). Source processes in the high-latitude ionosphere. *Space Science Reviews*, 88(1):7–84.

Nakamura, R., Oguti, T., Yamamoto, T., and Kokubun, S. (1993). Equatorward and poleward expansion of the auroras during auroral substorms. *Journal of Geophysical Research: Space Physics*, 98(A4):5743–5759.

Newell, P. T. and Meng, C.-I. (1988). The Cusp and the Cleft/Boundary Layer: Low-Altitude Identification and Statistical Local Time Variation. *J. Geophys. Res.*, 93(A12):14549–14556.

Newell, P. T. and Meng, C.-I. (1989). Dipole Tilt Angle Effects on the Latitude of the Cusp and Cleft/Low-Latitude Boundary Layer. *J. Geophys. Res.*, 94(A6):6949–6953.

Newell, P. T. and Meng, C.-I. (1994). Comment on "Unexpected Features of the Ion Precipitation in the So-Called Cleft/Low-Latitude Boundary Layer Region: Association with Sunward Convection and Occurrence on Open Field Lines" by A. Nishida, T. Mukai, H. Hayakawa, A. Matsuoka, K. Tsuruda, N. K. *J. Geophys. Res.*, 99(A10):19609–19614.

Newell, P. T., Meng, C.-I., Sibeck, D. G., and Lepping, R. (1989). Some Low-Altitude Cusp Dependencies on the Interplanetary Magnetic Field. *J. Geophys. Res.*, 94(A7):8921–8927.

Opgenoorth, H. J., Pellinen, R. J., Baumjohann, W., Nielsen, E., Marklund, G., and Eliasson, L. (1983). Three-dimensional current flow and particle precipitation in a westward travelling surge (observed during the Barium-Geos Rocket Experiment). *Journal of Geophysical Research: Space Physics*, 88(A4):3138–3152.

Paschmann, G., Håland, S., and Treumann, R. (2003). *Auroral Plasma Physics*. Space Science Series of ISSI, V. 15. Kluwer Academic Pub.

Pfaff, R., Clemmons, J., Carlson, C., Ergun, R., McFadden, J., Mozer, F., Temerin, M., Klumpar, D., Peterson, W., Shelley, E., Mœbius, E., Kistler, L., Strangeway, R., Elphic, R., and Cattell, C. A. (1998). Initial FAST observations of acceleration processes in the cusp. *Geophysical Research Letters*, 25(12):2037–2040.

Reeves, G., Henderson, M., McLachlan, P., Belian, R., Friedel, R., and Korth, A. (1996). Radial propagation of substorm injections. In Rolfe, E. and Kaldeich, B., editors, *International Conference on Substorms*, volume 389 of *ESA Special Publication*, page 579.

Runov, A., Angelopoulos, V., Sitnov, M. I., Sergeev, V. A., Bonnell, J., McFadden, J. P., Larson, D., Glassmeier, K.-H., and Auster, U. (2009). THEMIS observations of an earthward-propagating dipolarization front. *Geophysical Research Letters*, 36(14).

Russell, C. T. (2000). The polar cusp. *Advances in Space Research*, 25(7-8):1413 – 1424.

Russell, C. T., Snare, R. C., Means, J. D., Pierce, D., Dearborn, D., Larson, M., Barr,

G., and Le, G. (1995). The GGS/POLAR magnetic fields investigation. *Space Science Reviews*, 71(1-4):563–582.

Sato, N., Kadokura, A., Motoba, T., Hosokawa, K., Björnsson, G., and Saemundsson, T. (2015). Interhemispheric Symmetries and Asymmetries of Aurora from Ground-Based Conjugate Observations. In *Auroral {Dynamics} and {Space} {Weather}*, pages 145–161. John Wiley & Sons, Inc.

Savin, S., Skalsky, A., Zelenyi, L., Avanov, L., Borodkova, N., Klimov, S., Lutsenko, V., Panov, E., Romanov, S., Smirnov, V., Yermolaev, Y., Song, P., Amata, E., Consolini, G., Fritz, T. A., Buechner, J., Nikutowski, B., Blecki, J., Farrugia, C., Maynard, N., Pickett, J., Sauvaud, J. A., Rauch, J. L., Trotignon, J. G., Khotyaintsev, Y., and Stasiewicz, K. (2005). Magnetosheath Interaction with the High Latitude Magnetopause. *Surveys in Geophysics*, 26(1-3):95–133.

Scudder, J., Hunsacker, F., Miller, G., Lobell, J., Zawistowski, T., Ogilvie, K., Keller, J., Chornay, D., Herrero, F., Fitzenreiter, R., Fairfield, D., Needell, J., Bodet, D., Googins, J., Kletzing, C., Torbert, R., Vandiver, J., Bentley, R., Fillius, W., McIlwain, C., Whipple, E., and Korth, A. (1995). Hydra — A 3-dimensional electron and ion hot plasma instrument for the POLAR spacecraft of the GGS mission. *Space Science Reviews*, 71(1-4):459–495.

Sergeev, V. A., Liou, K., Newell, P. T., Ohtani, S.-I., Hairston, M. R., and Rich, F. (2004). Auroral streamers: characteristics of associated precipitation,convection and field-aligned currents. *Annales Geophysicae*, 22(2):537–548.

Shelley, E. G., Ghielmetti, A. G., Balsiger, H., Black, R. K., Bowles, J. A., Bowman, R. P., Bratschi, O., Burch, J. L., Carlson, C. W., Coker, A. J., Drake, J. F., Fischer, J., Geiss, J., Johnstone, A., Kloza, D. L., Lennartsson, O. W., Magoncelli, A. L., Paschmann, G., Peterson, W. K., Rosenbauer, H., Sanders, T. C., Steinacher, M., Walton, D. M., Whalen, B. A., and Young, D. T. (1995). The Toroidal Imaging Mass-Angle Spectrograph (TIMAS) for the polar mission. *Space Science Reviews*, 71(1):497–530.

Shiokawa, K., Baumjohann, W., and Haerendel, G. (1997). Braking of high-speed flows in the near-Earth tail. *Geophysical Research Letters*, 24(10):1179–1182.

Smith, J. O. (2008). *Introduction to Digital Filters: With Audio Applications*. Music signal processing series. W3K.

Song, Y. and Lysak, R. L. (2013). Paradigm Transition in Cosmic Plasma Physics, Magnetic Reconnection and the Generation of Field-Aligned Current. In *Magnetospheric {Current} {Systems}*, pages 11–19. American Geophysical Union.

Strangeway, R. J., Ergun, R. E., Su, Y.-J., Carlson, C. W., and Elphic, R. C. (2005). Factors controlling ionospheric outflows as observed at intermediate altitudes. *J. Geophys. Res.*, 110(A3):A03221.

Su, Y.-J., Ergun, R. E., Peterson, W. K., Onsager, T. G., Pfaff, R., Carlson, C. W., and Strangeway, R. J. (2001). Fast Auroral Snapshot observations of cusp electron and ion structures. *Journal of Geophysical Research: Space Physics*, 106(A11):25595–25600.

Temerin, M. and Roth, I. (1986). Ion heating by waves with frequencies below the ion gyrofrequency. *Geophysical Research Letters*, 13(11):1109–1112.

Torrence, C. and Compo, G. P. (1998). A Practical Guide to Wavelet Analysis. *Bulletin of the American Meteorological Society*, 79(1):61–78.

Trattner, K. J., Fuselier, S. A., Peterson, W. K., Boehm, M., Klumpar, D., Carlson, C. W., and Yeoman, T. K. (2002a). Temporal versus spatial interpretation of cusp ion structures observed by two spacecraft. *J. Geophys. Res.*, 107(A10):1287.

Trattner, K. J., Fuselier, S. A., Peterson, W. K., and Carlson, C. W. (2002b). Spatial features observed in the cusp under steady solar wind conditions. *J. Geophys. Res.*, 107(A10):1288.

Wahlund, J. E., Opgenoorth, H. J., Häggström, I., Winser, K. J., and Jones, G. O. L.

(1992). EISCAT observations of topside ionospheric ion outflows during auroral activity: Revisited. *Journal of Geophysical Research: Space Physics*, 97(A3):3019–3037.

Wiltberger, M., Lotko, W., Lyon, J. G., Damiano, P., and Merkin, V. (2010). Influence of cusp O+ outflow on magnetotail dynamics in a multifluid MHD model of the magnetosphere. *Journal of Geophysical Research: Space Physics*, 115(A10):n/a–n/a.

Wygant, J. R., Bonnell, J. W., Goetz, K., Ergun, R. E., Mozer, F. S., Bale, S. D., Ludlam, M., Turin, P., Harvey, P. R., Hochmann, R., Harps, K., Dalton, G., McCauley, J., Rachelson, W., Gordon, D., Donakowski, B., Shultz, C., Smith, C., Diaz-Aguado, M., Fischer, J., Heavner, S., Berg, P., Malsapina, D. M., Bolton, M. K., Hudson, M., Strangeway, R. J., Baker, D. N., Li, X., Albert, J., Foster, J. C., Chaston, C. C., Mann, I., Donovan, E., Cully, C. M., Cattell, C. A., Krasnoselskikh, V., Kersten, K., Brenneman, A., and Tao, J. B. (2013). The Electric Field and Waves Instruments on the Radiation Belt Storm Probes Mission. *Space Science Reviews*, 179(1):183–220.

Wygant, J. R., Cattell, C. A., Lysak, R. L., Song, Y., Dombeck, J., McFadden, J., Mozer, F. S., Carlson, C. W., Parks, G., Lucek, E. A., Balogh, A., André, M., Reme, H., Hesse, M., and Mouikis, C. (2005). Cluster observations of an intense normal component of the electric field at a thin reconnecting current sheet in the tail and its role in the shock-like acceleration of the ion fluid into the separatrix region. *Journal of Geophysical Research: Space Physics*, 110(A9):n/a–n/a.

Wygant, J. R., Keiling, A., Cattell, C. A., Johnson, M., Lysak, R. L., Temerin, M., Mozer, F. S., Kletzing, C. A., Scudder, J. D., Peterson, W., Russell, C. T., Parks, G., Brittnacher, M., Germany, G., and Spann, J. (2000). Polar spacecraft based comparisons of intense electric fields and Poynting flux near and within the plasma sheet-tail lobe boundary to UVI images: An energy source for the aurora. *J. Geophys. Res.*, 105(A8):18675–18692.

Wygant, J. R., Keiling, A., Cattell, C. A., Lysak, R. L., Temerin, M., Mozer, F. S., Kletzing, C. A., Scudder, J. D., Streltsov, V., Lotko, W., and Russell, C. T. (2002). Evidence for

kinetic Alfvén waves and parallel electron energization at 4-6 RE altitudes in the plasma sheet boundary layer. *J. Geophys. Res.*, 107(A8):1201.

Zhang, B., Lotko, W., Brambles, O., Damiano, P., Wiltberger, M., and Lyon, J. (2012). Magnetotail origins of auroral Alfvénic power. *Journal of Geophysical Research: Space Physics*, 117(A9).

Appendix A

The Moving Average Transform

Traditionally, moving average (or smoothing) is used in removing high frequency noises. As its companion operation, detrending removes the low frequency background and retains the high frequency signals. Therefore combining smoothing and detrending can achieve crude bandpass effect. For example, a signal $f_0 = f_l + f + f_h$ consists of a low-frequency background f_l, a high frequency noise f_h, and the main signal f at a mediocre frequency. The main signal f can be extracted by smoothing and detrending, which removes f_h and f_l respectively. Because smoothing and detrending are extremely simple to implement, they are widely used in data preprocessing.

However, in this chapter, we show that the moving average transform (MAT), which is merely a special combination of smoothing and detrending, could achieve time and frequency resolution which is comparable to the wavelet analysis. While preserving the simplicity of smoothing/detrending, MAT has the following advantages: (1) The algorithm is real-valued and directly operates on waveforms. In many cases, there is no interesting in quantities like power or phase, which involves in complex-valued spectrum. (2) Easy to implement and fast to run. We will show that the time complexity is $\mathcal{O}(N)$ per scale, where N is the length of the time series. In comparison, the time complexity of the wavelet transform is $\mathcal{O}(N \log_2 N)$ per scale (Jones and Baraniuk, 1991). In the sections, we show the basic definition of the

moving transform transform, and apply it to both analytical and real-world examples.

A.1 Basics

For a time series of a generic quantity $x(t)$, its moving average transform at certain scale p is defined to be

$$M_p(t) = x(t) - \frac{1}{p}\int_{t-p/2}^{t+p/2} x\left(t'\right) dt'. \tag{A.1}$$

Note that the last term is the moving average (smoothing) of the original signal, and this is where the algorithm got its name. The next section will show that the scale p simply means the wave period. In other words, a moving average transform at p will extract the wave at the period of p. If there is no wave power at that period, then $M_p(t)$ will be ~ 0. Otherwise if the signal is monochromatic at the period of p, then it is $\sim 100\%$ extracted by $M_p(t)$.

From Equation (A.1), we derive that the time complexity of the transform is $\mathcal{O}(N)$. As the basic calculation, an s-point moving average $\sum_{i=1}^{s} x_i$ costs $s-1$ additions. The most part can be re-used since the next moving average costs 2 additions, $\sum_{i=2}^{s+1} x_i = \sum_{i=1}^{s} x_i + x_{s+1} - x_1$. Therefore the second term in Equation (A.1) costs $(s-1) + 2(N-s) = 2N - s - 1$ additions, and 1 multiplication to account for the common factor $\delta t/p$, where δt is the data rate. N additions are needed to subtract the second term from the first. So the total operations are $3N - s$, which is of $\mathcal{O}(N)$.

from Equation (A.1), we can also study the effect of boundary condition. For a scale p, information over $\pm p/2$ around the current time is needed. Therefore the moving average transform is only reliably defined for the time between $[p/2, T - p/2]$, where T is the duration. As a comparison, the Morlet wavelet has a boundary effect of $\sqrt{2}p \simeq 1.4p$. We will show later that high order moving average transform can achieve fine resolution in the frequency (period) domain The transform defined in Equation (A.1) is of order 1. The boundary effect is kp for the k-th order moving average transform, which is recursively

defined as

$$M_p^k(t) = M_p^{k-1}(t) - \frac{1}{p}\int_{t-p/2}^{t+p/2} M_p^{k-1}\left(t'\right) dt'. \tag{A.2}$$

A.2 Monochromatic Wave

As the simplest example, we apply the moving average transform to a general sinusoidal wave

$$x_p(t) = A\sin\left(2\pi t/p + \phi\right).$$

According to the definition in Equation (A.1), the moving average transform for $x_p(t)$ at certain scale p' is

$$\begin{aligned} M_p\left(t, p'\right) &= \left[1 - \frac{\sin\left(\pi p'/p\right)}{\pi p'/p}\right] \cdot x_p(t), \\ m_{p,p'} &\equiv 1 - \frac{\sin\left(\pi p'/p\right)}{\pi p'/p}. \end{aligned} \tag{A.3}$$

There are several points to be discussed on the above results. First of all, the moving average transform preserves phase. This is consistent with the fact that zero-phase filters cannot be causal (Smith, 2008). The moving average transform is non-causal since the output requires both past, present, and future inputs. Equation (A.3) shows that the only effect of the transform is an amplitude modulation, as represented by the amplitude coefficient $m_{p,p'}$. The second point is about the properties of this coefficient. As can be seen in Figure A.1, the black curve plots the amplitude coefficient in Equation (A.3). For a wave at the period p, the curve can be understood as the frequency response to the moving average transform at different scales p'. The respond is 1 when the scale approaches the wave period $p' \simeq p$. On the other hand, if $p' \ll p$, the amplitude coefficient is 0, i.e., the wave does not response to small scales at all. Figure A.1 also shows the frequency response of higher order moving average transforms. The curve becomes sharper at the cut-off frequency, which means better resolution in the frequency domain.

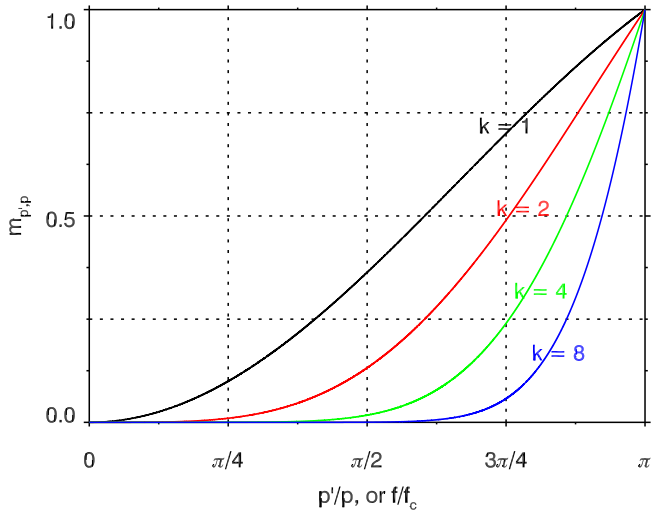

Figure A.1: The amplitude coefficient $m_{p',p}$ as a function of p'/p, where p' is the scale of the transform and p is the wave period. The amplitude coefficient approaches a delta function $\delta(p - p')$ as the order k increases.

A.3 Step Function

The second test is on the step function $f_s(t)$, with which we illustrate the meaning of the MAT time-period spectrogram and the effect of high order transforms. The step function is defined as

$$f_s(t) = \begin{cases} 1 & t \in [-\pi, 0) \\ 0 & t \in [0, \pi] \end{cases}, \quad f_s(t + 2\pi) = f_s(t).$$

It is a classic example for Fourier series expansion,

$$f_s(t) = \frac{4}{\pi}\left\{\sin(t) + \frac{\sin(3t)}{3} + \frac{\sin(5t)}{5} + \cdots\right\},$$

or in a shorter notation,

$$f_s(t) = \sum_{m=1}^{odd} f_m(t), \quad \text{where } f_m(t) = \frac{4\sin(mt)}{m\pi}.$$

The first 4 terms in the Fourier series are plotted in Figure A.2. It is important to note that the color of the spectrogram represents the value of waveform. Each row in the spectrogram is the waveform around the corresponding period (frequency). The spectrogram is a decomposed view of the original waveform.

Suppose we approximate the step function using the first 2 Fourier series

$$f_s(t) = f_1 + f_3.$$

From the previous section, we saw that to extract f_3, we should consider the moving average at the scale $p = p_3 = 2\pi/3$. Following Equation (A.1) we get[1]

$$M_p(t) = 0.173 f_1 + f_3.$$

f_3 is completely extracted as intended, but with a small fraction of f_1 due to the finite width of the amplitude coefficient in the frequency domain. A trick to improve the extraction is to perform a second moving average transform to $M_p(t)$,

$$M_p^2(t) = 0.173^2 f_1 + f_3 = 0.003 f_1 + f_3.$$

Now the second order moving average transform only contains 0.3% of f_1. Higher order will always improve frequency resolution, since the amplitude coefficient is ensured to be ≤ 1 by the algorithm in the next section. Except for the waves with period close to the scale p, all other waves disappear exponentially as the order $k$increases (c.f. panel b in Figure A.1). The cost of higher order transform is the decreasing time resolution, obeying the "uncertainty principle" $\delta f \delta t > 1$.

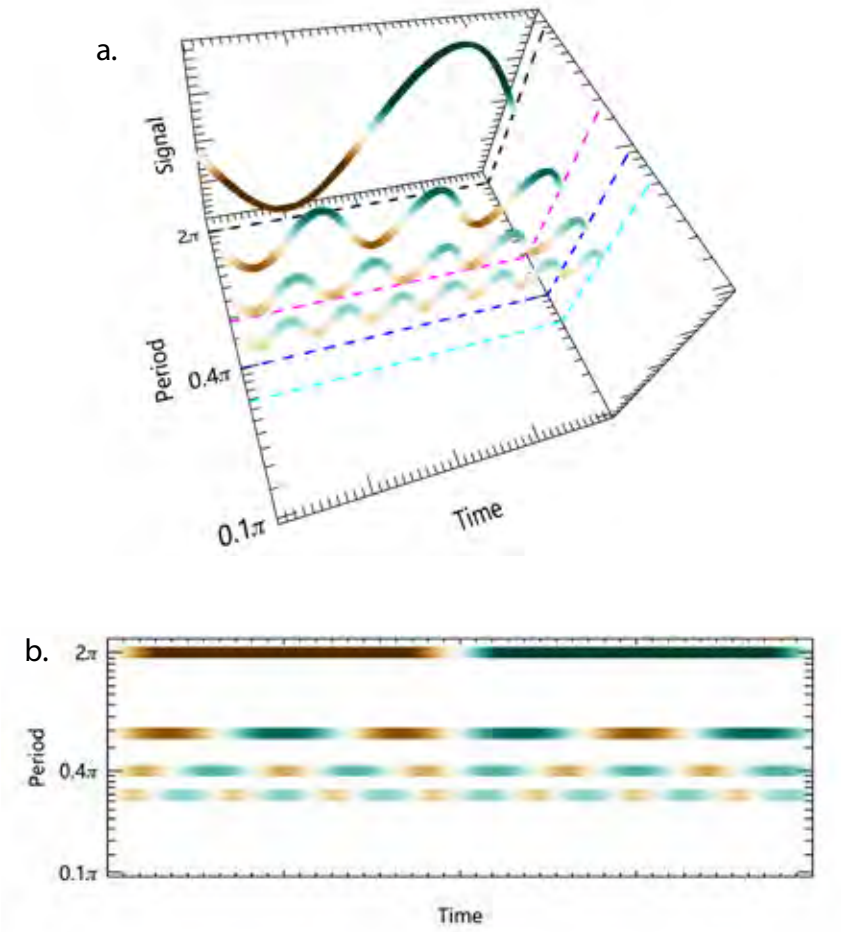

Figure A.2: The Fourier series of the step function. Only the first 4 terms are included: f_1, f_3, f_5, and f_7. Panel b shows the 4 components in the time-period space, where color indicates the value of the waveform. Panel a shows the same data but in the 3-D space, to emphasize the mapping between waveform and color.

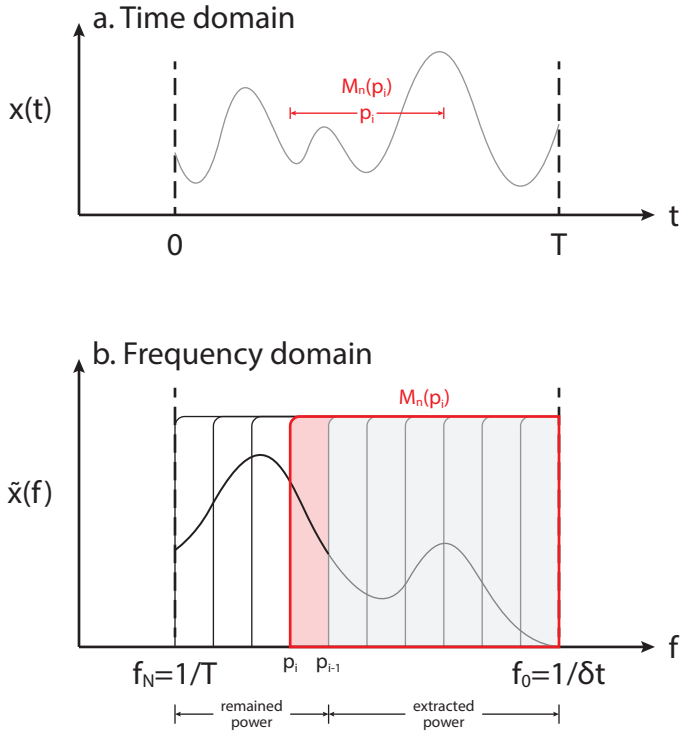

Figure A.3: Schematic view of how the moving average transform works for predefined scales.

A.4 General Procedure

We showed that increasing the order k effectively sharpens the frequency response (Figure A.1). The part around around the cut-off frequency $f_c = 1/p'$ is the most important. The frequency response can be approximated as a step function, assuming no wave power at higher frequencies $f > f_c$. The assumption can be achieved by working from the small scales to larger ones. The smallest scale always exist since the time series is measured below the Nyquist frequency. Figure A.3 shows the schematic view of how to apply a series of moving average transform to cover all measured frequency domain. Expressed in word is the following procedure:

1. For a time series $x_0(t)$ at the data rate of δt and the duration of T, establish a set of test scales $\{p_i\}$, $i = 0, 1, \ldots, m$. It is recommended to set $p_0 \geq 2\delta t$ and $p_M \leq T/2$.

2. Determine the order k. The optimum setting is $k \in [2, 4]$, based on tests among various signals.

3. Calculate the moving average for all scales. The order is important: from small scale to larger ones. The order ensures that the amplitude coefficient $m_{p,p'}$ can be approximated as a step function, and that increasing order will increase frequency resolution.

   (a) At the first scale p_1, the transform $M^k_{p_1}(t)$ should extract all waves with periods $\lesssim p_1$. Then $M^k_{p_1}(t)$ is saved elsewhere and removed from the original signal $x_1(t) = x_0(t) - M^k_{p_1}(t)$.

   (b) In general, for an arbitrary scale p_i $(i = 1, 2, \ldots, m-1)$, the input is $x_{i-1}(t)$, where all waves that have periods smaller than p_i have been extracted by previous transforms and removed from the original signal (Figure A.3). The transform $M^k_{p_i}(t)$ extracts the waves with period around p_i. It is saved elsewhere and removed from the original signal $x_i(t) = x_{i-1}(t) - M^k_{p_i}(t)$.

[1] $m_{p_1,p} = 0.173$ and $m_{p_3,p} = 1$.

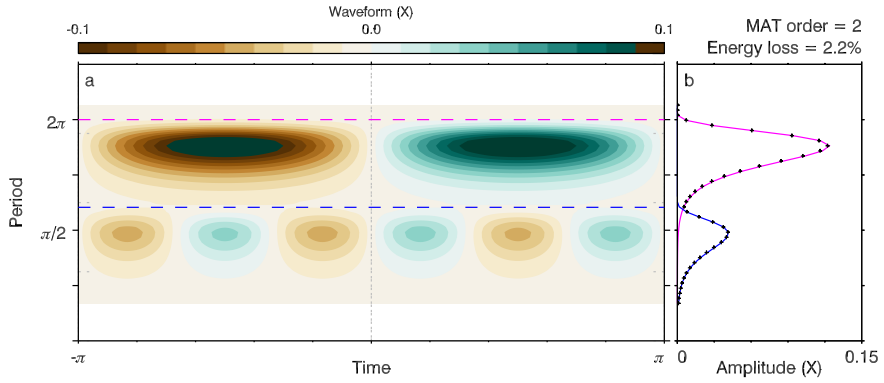

Figure A.4: Moving average transform applied on the step function approximation $f_s(t) \simeq f_1 + f_3$. Panel a shows the time-period spectrogram. Panel b shows the amplitude profile as a function of period. The black crosses are the results from the algorithm. The purple and blue curves are the theoretical predictions from the altitude coefficient.

(c) For the last scale p_m, $M^k_{p_m}(t)$ directly saves $x_{m-1}(t)$, which is the leftover from the previous operations, i.e., the background signal.

(d) In the end, all the extracted waves form a time-period spectrogram $M^k_{p_i}(t)$. They add up to the original signal $x_0(t) = \sum_{i=1}^{m} M^k_{p_i}(t)$.

To further illustrate the above procedure, we show the test results on the Fourier series of the step function, and append the IDL code for the moving average transform algorithm. Figure A.4 shows when only the first two terms of the Fourier series are included. The figure shows that the two bands f_1 and f_3 are well separated. As a test of the Parseval's theorem, the energy loss is 2.2 %. The error is due to the small overlap of the power of f_1 and f_3 (the crossover of the blue and purple curves in panel b).

In the rest of the section, we explain the altitude profile in panel b, which shows that the algorithm behaves as predicted by the amplitude coefficient $m_{p',p}$ in Equation (A.3). Phenomenologically, one important property of the MAT spectrogram is the following: For certain frequency band, the amplitude profile peaks near but below the true period. In other word, the upper boundary of the color blocks marks the period. This feature is a result of

the competition between extraction at the current scale and the subtraction due to previous scales. Take the purple curve of f_1 in panel b as an example, the algorithm starts from the smallest scale, where the amplitude coefficient is small. As the algorithm works towards the true period p_1, the extraction becomes more effective. However, the left-over amplitude is smaller due to previous extractions. When the scale reaches the true period, the wave band has been completely extracted. Bellow shows the IDL codes for the moving average transform algorithm.

```
; n: # of records, m: # of scales.
mspec = dblarr(n,m)      ; save the extracted waves.
fi = f0                  ; f0 is the original input signal.
for i=0, m-2 do begin
    ; do order 1 transform. ps are the scales.
    ma = smooth(fi,ps[i],/nan,/edge_truncate)
    mspec[*,i] = fi-ma   ; extract the wave.
    fi = ma              ; update the input signal.
    ; do higher order transforms.
    for j=0, k-1 do begin
        ma = smooth(mspec[*,i],ps[i],/nan,/edge_truncate)
        mspec[*,i] -= ma ; update the extracted wave.
        fi += ma         ; update the input signal.
    endfor
endfor
mspec[*,m-1] = fi   ; save the background signal.
```

A.5 Real Data

This section show examples when the moving average transform is applied on real data. The first example is on the time series of the El Nino-Southern Oscillation (ENSO) data, which is used in many wavelet related papers (Torrence and Compo, 1998, and references therein). Figure A.5 shows the original data in panel a. Its moving average transform is plotted in panel c, where the color represents the real-valued waveform. For comparison, panel b shows the spectrogram from the wavelet transform using the Morlet wavelet, which plots the real part of the wavelet transform. The figure shows that both methods can resolve the local power in time and frequency at comparable resolution. For example, there are

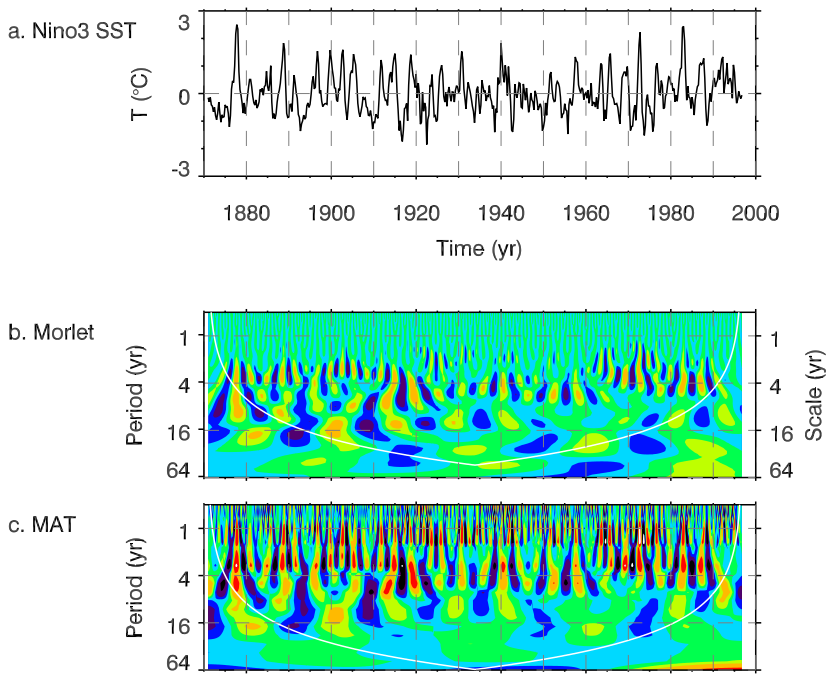

Figure A.5: Analyzing the El Nino-Southern Oscillation data using the moving average transform and the Morlet wavelet. Panel a shows the original time series. Panel b shows the real part of the Morlet wavelet transform. We note that the two y-axes are different by a factor close to 1. The wavelet transform is calculated based on the scales. The periods are derived from the scales based on the conversion factor (Torrence and Compo, 1998). Panel c shows the moving average transform at order 2.

hotspots of wave power in the 2-4 yr band from 1880 to 1910. The power around 16 yr at 1880 gradually decreased to about 10 yr at 1920. As a major difference, the moving average transform showed the power in the 1-2 yr band, which is missing in the wavelet result. In general, high frequency signals are not well resolved in wavelet transform, as explained in the end of this section. Another difference lies in the cone of influence (COI), marked by the white lines in panel b and c. The region below COI are affected by the boundary effect. Under comparable time and frequency resolution, smaller COI is preferred since the boundary effect is smaller.

As a second example, we apply the above two methods to the waves measured by RBSP-A during the main phase of a geomagnetic storm (Figure A.6). Panel a shows the waveform of the wave electric field in one of the spin plane direction, where the E vector is mainly along this direction. To perform the comparison from a different perspective, wave power is plotted in this example, since it is more commonly used in the literature. In panel c, the MAT waveform is converted to wave power. Overall, the same features appear in both panel b and c. For example, the wave around 100 Hz is well resolved by both methods.

The main difference of the two spectrograms is that the wavelet spectrogram emphasizes the power at low frequency but misses the high frequency power. This is true for both the wave power spectrogram in Figure A.6 and the waveform spectrogram in Figure A.5. The reason for the difference is that the wavelet transform is biased by scales (Liu et al., 2007). The bias arises from the fact that the wave power at certain wavelet scale s_i is the integration over the frequency it spans: $W_n(s_i)\, df_i \simeq W_n(s_i)/s_i$, where $W_n(s_i)$ is the wavelet spectrogram. The integration works as a correction, which cancels the bias towards the low frequency (or large scale) power. On the other hand, the moving average transform is not biased. As shown in Figure A.3, MAT spectrogram reflects the waveform or wave power between adjacent scales p_i and p_{i-1}. Therefore it is usually more convenient to use the moving average transform when waveform is the main focus in data analysis. Because MAT operates the waveform directly and the quantities are not biased as in wavelet analysis.

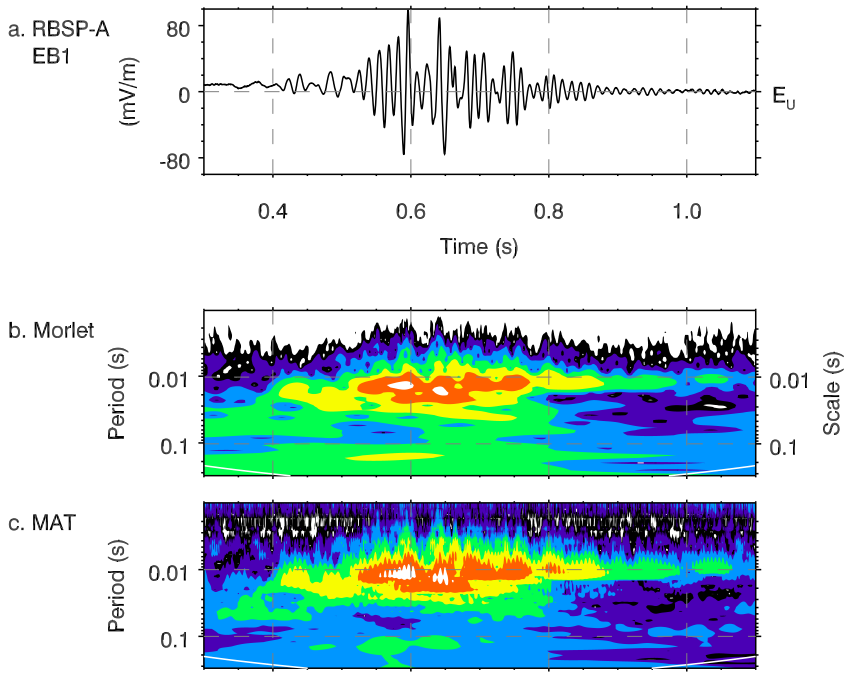

Figure A.6: Analyzing the waves in electric field measured by RBSP-A. Panels are in the same format as in Figure A.5. The only difference is that the spectrograms in panel b and c are wave power instead of waveform. The data are padded on both sides to (almost) eliminate the cone of influence due to the boundary effect.

Appendix B

Methods of Calculating the Poynting Flux

The Poynting flux $\boldsymbol{S}$ is a key quantity in estimating the energy circulation in the space plasma. However, it is not straightforward to obtain the correct waveform of the Poynting flux when the wave power is broadband. In this section, we discuss two methods to calculate the Poynting flux based on in-situ measurements of the electromagnetic wave. One method is based on the wavelet analysis using the Morlet wavelet. The second method uses the moving averaged transform explained in Appendix A. Both methods could resolve Poynting flux power in both the time t and the frequency domains. Besides the time-frequency spectrogram $\boldsymbol{S}(t,p)$, other important quantities could be readily calculated, including the power spectrum $\boldsymbol{S}(p)$, the total Poynting flux in the time domain $\boldsymbol{S}(t)$, and the Poynting flux in certain frequency range $\boldsymbol{S}_{[f_1,f_2]}(t)$.

Plasma can hold normal-mode waves at various frequencies. The Poynting flux carried by these waves can be calculated from

$$\boldsymbol{S} = \alpha \boldsymbol{E} \times \boldsymbol{B}^*, \tag{B.1}$$

for real-valued electric and magnetic waveforms (c.f. Equation (6.109) in Jackson (1999)), or from

$$\boldsymbol{S} = \frac{\alpha}{2} \left(\boldsymbol{E} \times \boldsymbol{B}^* \right), \tag{B.2}$$

where the quantities are in the complex notation (c.f. Equation (6.132) in Jackson (1999)). The coefficient α is $\frac{1}{400\pi} \simeq 0.08$ mW/(m-mV-nT)., following the conventional units in the space physics, where the electric field $\boldsymbol{E}$ is in mV/m, the magnetic field $\boldsymbol{B}$ is in nT, and the Poynting flux is in mW/m^2.

To illustrate the general procedure of calculating the Poynting flux, we begin with a simple case of an artificial electromagnetic wave has power at the period p_1 and p_2. To be simple, we assume that the electric field is along the x-axis and the magnetic field is along the y-axis. Thus the Poynting flux will be along the z-axis.

$$E_x(t) = E_{x1}(t) + E_{x2}(t) = E_1 \sin(2\pi t/p_1) + E_2 \sin(2\pi t/p_2) \tag{B.3}$$

$$B_y(t) = B_{y1}(t) + B_{y2}(t) = B_1 \sin(2\pi t/p_1) + B_2 \sin(2\pi t/p_2). \tag{B.4}$$

Panel a and b in Figure B.1 shows the waveforms of the electric and magnetic fields for $p_1 = 23$ sec , $E_1 = 10$ mV/m, $B_1 = 10$ nT; and $p_2 = 7$ sec , $E_2 = 20$ mV/m, $B_2 = 5$ nT. The spectrogram (real part) of the Morlet wavelet transform of E_x, B_y are shown below their waveforms.

B.1 Instantaneous Versus Time-Averaged

When calculating the Poynting flux, it is important to notice the difference between the *instantaneous* Poynting flux and the *time-averaged* Poynting flux.

Instantaneous Poynting flux Using Equation (B.1), the instantaneous Poynting flux is calculated from the electric and magnetic fields in the time domain in Equation (B.3) and

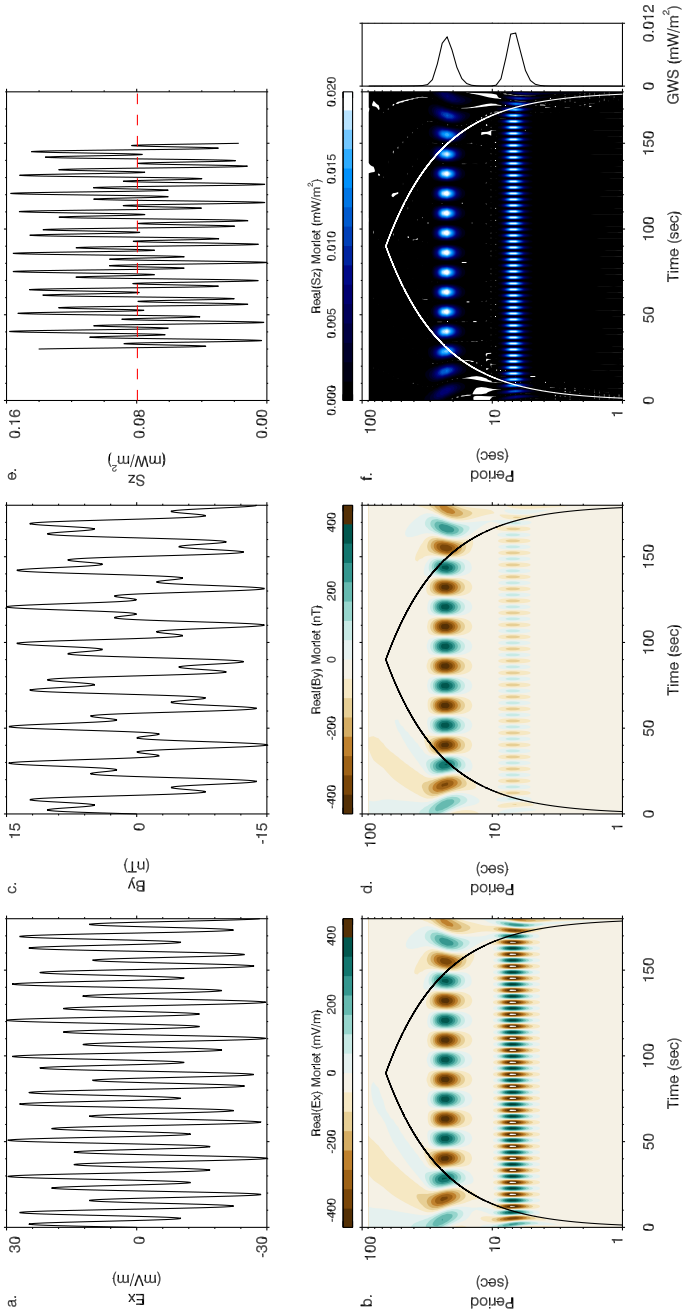

Figure B.1: Poynting flux calculation for an artificial electromagnetic wave.

(B.4)

$$S_z(t) = S_{z1}(t) + S_{z2}(t) = \alpha E_{x1}(t) \times B_{y1}(t) + \alpha E_{x2}(t) \times B_{y2}(t).$$

The calculation is completely done in the time domain. The theoretical Poynting flux and its spectrogram are shown in panel e and f in Figure B.1. Since people directly use the maximum Poynting flux quite often, we emphasize that it is incorrect to directly multiply the electric and magnetic fields,

$$S_z^{wrong}(t) = \alpha E_x(t) \times B_y(t) = \alpha[E_{x1}(t) + E_{x2}(t)] \times [B_{y1}(t) + B_{y2}(t)].$$

The wrong Poynting flux tends to over estimate the amplitude, because the cross-frequency terms are included. The error is even larger if the background magnetic field is not properly removed. For example, the correct maximum instantaneous Poynting flux is 0.16 $\mathrm{mW/m^2}$ in Figure B.1, while the wrong maximum is 0.36 if we were to multiply the electric and magnetic fields.

Time-averaged Poynting flux The above results can be tested from the Fourier analysis. In this paper, we follow the normalization convention

$$\tilde{x}(f) = \frac{1}{T}\int_0^T dt\ x(t)e^{-2\pi i f t}$$
$$x(t) = T\int_{-\infty}^{\infty} df\ \tilde{x}(f)e^{2\pi i f t},$$

where $x(t)$ is a generic quantity in the unit of X and $\tilde{x}(f)$ is its Fourier coefficient at frequency f. The two quantities $x(t)$ and $\tilde{x}(f)$ have the same unit X. Following this normalization, the Parseval's theorem is in the form of

$$\frac{1}{T}\int_0^T dt\ x^2(t) = \int_{-\infty}^{\infty} df\ \tilde{x}^2(f) = 2\int_0^{\infty} df\ \tilde{x}^2(f),$$

where the reality condition $\tilde{x}(-f) = \tilde{x}^*(f)$ has been invoked. The factor of 2 in the last term accounts for the contribution from negative frequencies. The rational of this normalization is that the total energy consists of contribution from all frequencies $\tilde{x}^2(f)\,df$. The `fft` function in IDL follows the above normalization (`https://www.harrisgeospatial.com/docs/FFT.html`).

The Fourier transforms of the electric and magnetic fields in the above example are

$$\tilde{E}_x(f) = \tilde{E}_{x1}(f_1) + \tilde{E}_{x1}(f_1) \qquad \text{where} \quad \tilde{E}_{x1}(f_1) = E_1/2 \quad \text{and} \quad \tilde{E}_{x2}(f_2) = E_2/2$$
$$\tilde{B}_y(f) = \tilde{B}_{y1}(f_1) + \tilde{B}_{y1}(f_1) \qquad \text{where} \quad \tilde{B}_{y1}(f_1) = B_1/2 \quad \text{and} \quad \tilde{B}_{y2}(f_2) = B_2/2.$$

Using Equation (B.2), the Poynting flux in the frequency domain is

$$\tilde{S}_z = \sum_{i=1,2} \tilde{S}_{zi}(f_i) \quad \text{where } \tilde{S}_{zi}(f_i) = 2\alpha \tilde{E}_{xi}(f_i) \times \tilde{B}^*_{yi}(f_i).$$

Specifically, $\tilde{S}_{z1} = \tilde{S}_{z2} = 0.04$ mW/m^2 and so $\tilde{S}_z = \tilde{S}_{z1} + \tilde{S}_{z2} = 0.08$ mW/m^2. In the example, the power of the Poynting flux is time independent, thus the time-averaged Poynting flux $\bar{S}_z(t)$ is a constant $\bar{S}_z(t) \equiv \tilde{S}_z$. The red dashed line marks $\tilde{S}_z(t)$ in panel e in Figure B.1.

Instantaneous versus time-averaged In general, the time-averaged Poynting flux $\bar{S}(t)$ at certain frequency f can be calculated by smoothing the instantaneous Poynting flux $S(t)$ at the corresponding period $T = 1/f$,

$$\bar{S}(t) = \frac{1}{T} \int_{t'-T/2}^{t'+T/2} dt'\; S\left(t'\right).$$

Conversely, twice of the time-averaged Poynting flux $2\bar{S}(t)$ approximately tracks the envelope of the instantaneous Poynting flux $S(t)$. Similar to the Poynting flux (energy flux), the energy density also has the two flavors. For instance, the electric field

$E_{x1}(t) = E_1 \sin(2\pi t/p_1)$ in the above example has an instantaneous energy density $w_E(t) = |E_{x1}(t)|^2 = E_1^2 \sin^2(2\pi t/p_1)$, which fluctuating at $f = 2f_1$ in the amplitude range $\left[0, E_1^2\right]$. On the other hand, the time-averaged energy density is time-independent, $\bar{w}_E(t) \equiv \tilde{w}_E(f_1) = 2|\tilde{E}_{x1}(f_1)|^2 = E_1^2/2$.

The instantaneous quantity emphasizes the real-time fluctuations on the wave power at twice the wave frequency, while the time-averaged one only contains the temporal change of the envelope (or amplitude). One simple but important consequence is that the two flavors are different in amplitude. In this paper, the term "maximum Poynting flux" refers to the instantaneous Poynting flux, which is usually twice of the maximum time-averaged Poynting flux. Regardless of the amplitude difference, the two flavors give the same averaged power $\bar{P}$,

$$\bar{P} = \frac{1}{T}\int_0^T dt\ S_z\left(t\right) = \frac{1}{T}\int_0^T dt\ \bar{S}_z\left(t\right),$$

where T is the duration of the signal. This is a natural result from the Parseval's theorem, and effectively means the area under the curve is the same (panel e in Figure B.1).

B.2 Procedure to Calculate the Poynting Flux

The simple example of artificial wave shows that some frequency analysis is needed to obtain the correct Poynting flux. To emphasize the importance role of frequency analysis, we briefly re-visit the discussion on the wrong instantaneous Poynting flux $S_z^{wrong}\left(t\right)$. It over estimates the maximum amplitude due to the cross-frequency terms, and here we show that it also gives the wrong averaged power $\bar{P}^{wrong}$. The error still comes from the cross-frequency terms. Although in theory the sine waves at different frequencies are orthogonal, the integral for $E_i \times B_j$ when $i \neq j$ is in general non-zero for a finite duration, unless the duration is the common multiple for the wave periods p_i and p_j. In the above example, the error of $\bar{P}^{wrong}/\bar{P} = 0.994$, where the duration $T = 180$ sec and the two periods are $p_1 = 7$ sec and $p_2 = 23$ sec. The error is in general non-zero and could be positive or negative. The error

is more significant if there exists a wave at a period comparable to the duration of the time series.

Therefore, it is crucial to separate or decompose the waves at different frequencies to eliminate the error from the cross-frequency terms. The error affects both the wave amplitude and power. In the next section, we show two methods for wave decomposition. The first method is to use the moving average transform, which decomposes the waves directly in the time domain. The method is suitable to calculate the instantaneous Poynting flux. The method is very intuitive since it works with waveforms in the time domain. The second method uses the Morlet wavelet to perform decomposition in the frequency domain and to reconstruct waveforms in the time domain. This method is more widely accepted but slower and more complicated than the first method. The method can calculate either the instantaneous or the time-averaged Poynting flux directly. We will show that the two methods give similar Poynting flux estimations.

Procedure to calculate the Poynting flux Based on the above discussions, we summarize the proper procedure to obtain the Poynting flux:

1. Use frequency analysis tools to decompose the original electric and magnetic fields in the frequency (period) domain. From $\boldsymbol{E} \rightarrow \{\boldsymbol{E}_{p_i}\}$ and $\boldsymbol{B} \rightarrow \{\boldsymbol{B}_{p_i}\}$.

2. Calculate the Poynting flux in each frequency band.

   (a) For the time-averaged Poynting flux, $\bar{\boldsymbol{S}}_{p_i}(t) = \frac{\alpha}{2}\boldsymbol{E}_{p_i} \times \boldsymbol{B}^*_{p_i}$, where the electric fields are understood as the complex notation. The time dependence shows the temporal change of the power of the time-averaged Poynting flux.

   (b) For the instantaneous Poynting flux, $\boldsymbol{S}_{p_i}(t) = \alpha\boldsymbol{E}_{p_i} \times \boldsymbol{B}_{p_i}$, where the electric fields are in time domain. There is a factor of 2 difference due to the contribution from the complex conjugate term, c.f. (6.109) and (6.132) in Jackson (1999).

3. The total Poynting flux can be calculated by summing the Poynting fluxes over all

frequency bands in Step 2. $\boldsymbol{S}(t) = \sum_i \boldsymbol{S}_{p_i}(t)$ for the instantaneous Poynting flux, $\bar{\boldsymbol{S}}(t) = \sum_i \bar{\boldsymbol{S}}_{p_i}(t)$ for the time-averaged Poynting flux.

4. Other Quantities.

   (a) Given the time averaged Poynting flux, $2\bar{\boldsymbol{S}}(t)$ provides an estimation of the envelope of $S(t)$ and therefore the proper maximum amplitude.

   (b) Given the instantaneous Poynting flux, the time-averaged Poynting flux can be calculated by smoothing over the wave periods, $\bar{\boldsymbol{S}}_{p_i}(t) = \frac{1}{p_i}\int_{t-p_i/2}^{t+p_i/2} dt'\ \boldsymbol{S}_{p_i}(t')$.

   (c) The frequency spectrum for the Poynting flux can be obtained by averaging the time-averaged Poynting flux $\left\{\int_0^T dt\ \bar{\boldsymbol{S}}_{p_i}(t)\right\}$. The set depends on the wave periods $\{p_i\}$ or frequencies $\{f_i = 1/p_i\}$.

B.3 Using the Moving Average Transform

Since all in-situ data are discrete, we will express the time series of a generic quantity x in the explicit discrete notation x_n instead of a continuous function of time $x(t)$. We will assume that the measured electric field E_n and magnetic field B_n are at uniformly spaced time records t_n, where $n = 1, 2, \ldots, N$. The time spacing is δt, so the duration is $T = N\delta t$ and the frequency spacing is $\delta f = 1/T$. For simplicity, we assume that the electric field is in the $x-$direction and the magnetic field is in the $y-$direction, so that the Poynting flux is in the $z-$direction.

First, we calculate the moving average transform (MAT) for the given electric and magnetic fields,

$$E_n \to E_n^M(p_m),$$
$$B_n \to B_n^M(p_m),$$

where the superscript M stands for the moving average transform. p_m's are the periods

where the transforms are calculated, $m = 0, 1, \ldots, J$. Usually, the periods are logarithmically spaced. Appendix A includes explains how the transform operates. At each period p_i, $E_n^M(p_i)$ and $B_n^M(p_i)$ represents the instantaneous, real-valued waveforms of the original data at the period. Hence, the summation over all periods reconstructs the original data,

$$E_n = \sum_{m=0}^{J} E_n^M(p_m),$$
$$B_n = \sum_{m=0}^{J} B_n^M(p_m).$$

Filtering can be achieved by summing over a limited periods between the filters. Following Equation (B.1), the time-period spectrogram for the Poynting flux is (in 3-D)

$$\boldsymbol{S}_n^M(p_m) = \alpha \boldsymbol{E}_n^M(p_m) \times \boldsymbol{E}_n^M(p_m).$$

The above Poynting flux is the instantaneous Poynting flux, since the electric and magnetic data are real-valued and instantaneous. The total Poynting flux is obtained by summing over all periods

$$\boldsymbol{S}_n^M = \sum_{m=0}^{J} \boldsymbol{S}_n^M(p_m).$$

B.4 Using the Morlet Wavelet

The general wavelet transform of a time sequence x_n is

$$X_n^W(s_m) = \sum_{n'=1}^{N} x_{n'} \Psi^*\left[\left(n' - n\right)\delta t / s_m\right],$$

where the superscript W stands for wavelet, and $\Psi(z)$ is the "mother wavelet". Specifically, we will use the Morlet mother wavelet

$$\Psi(z) = \pi^{-1/4} e^{i\omega_0 z} e^{-z^2/2},$$

where the parameter $\omega_0 = 6$ (Torrence and Compo, 1998). The mother function is properly normalized to ensure it contains unit energy and satisfies the Parseval's theorem. The wavelet transform is complex and in the unit of X. $s_m = s_0 2^{j\delta j}$ are scales, where $m = 0, 1, \ldots, J$. For the Morlet wavelet, δj should be smaller than 0.5, and s_0 should be greater than $2\delta t$. The scales s_m can be transformed into wave period p_m linearly

$$p_m = \frac{4\pi}{\omega_0 + \sqrt{2 + \omega_0^2}} s_m, \quad \text{for all } m.$$

After all the quantities are defined, the Morlet wavelet transform of the electric and magnetic fields are

$$E_n^W(s_m) = \sum_{n'=1}^{N} E_{n'} \Psi^* \left[\left(n' - n \right) \delta t / s_m \right],$$
$$B_n^W(s_m) = \sum_{n'=1}^{N} E_{n'} \Psi^* \left[\left(n' - n \right) \delta t / s_m \right].$$

Following Equation (B.2), the Poynting flux in the time-scale space is

$$\bar{S}_n^{W'}(s_m) = \frac{\alpha}{2} E_n^W(s_m) \times B_n^{W*}(s_m). \tag{B.5}$$

Note that the above Poynting flux is the time-averaged Poynting flux, which is similar to the time-averaged energy density $\bar{w}_E \propto \tilde{E}_n \cdot \tilde{E}_n^*$. We add a prime for the Poynting flux because it is not the final result we want for two reasons. First, the above Poynting flux is complex. The measurable Poynting flux is the real part. Second, the true time-averaged Poynting flux equals to twice of the real part, due to the contribution of the complex conjugate part. To account for these two operations, we re-write Equation (B.5) as

$$\bar{\boldsymbol{S}}_n^W(s_m) = \Re \left\{ \alpha \boldsymbol{E}_n^W(s_m) \times \boldsymbol{B}_n^{W*}(s_m) \right\}, \tag{B.6}$$

in the full 3-D vector form.

Alternatively, we can also calculate the instantaneous Poynting flux. For this purpose, we get the electric and magnetic waveforms in the time-scale domain by taking the real-part of their wavelet transforms

$$E_n(s_m) = \Re\left\{E_n^W(s_m)\right\},$$
$$B_n(s_m) = \Re\left\{B_n^W(s_m)\right\}.$$

To get the true waveform, a special summation is invoked (Torrence and Compo, 1998)

$$E_n = \frac{\delta j \delta t^{1/2}}{C_\delta \Psi_0(0)} \sum_{m=0}^{J} \frac{\Re\{E_n(s_m)\}}{s_m^{1/2}},$$

where the reconstruction factor $C_\delta = 0.776$ for $\omega_0 = 6$. Similarly, the waveform between a given filter can be calculated. As a comparison, the MAT spectrogram is more intuitive since the MAT values already represent the true waveform. Following Equation (B.1), the instantaneous Poynting flux is

$$\boldsymbol{S}_n^W(s_m) = \alpha \Re\left\{\boldsymbol{E}_n^W(s_m)\right\} \times \Re\left\{\boldsymbol{B}_n^W(s_m)\right\}, \tag{B.7}$$

in the full 3-D vector form. The total instantaneous or time-averaged Poynting flux is obtained by a special summation over all the scales (Torrence and Compo, 1998),

$$\boldsymbol{S}_n^W = \frac{\delta j \delta t}{C_\delta N} \sum_{m=0}^{J} \frac{\boldsymbol{S}_n^W(s_m)}{s_m},$$
$$\bar{\boldsymbol{S}}_n^W = \frac{\delta j \delta t}{C_\delta N} \sum_{m=0}^{J} \frac{\bar{\boldsymbol{S}}_n^W(s_m)}{s_m}.$$

Similarly, the Poynting flux within certain filter can be summed over by the scales between the given filter.

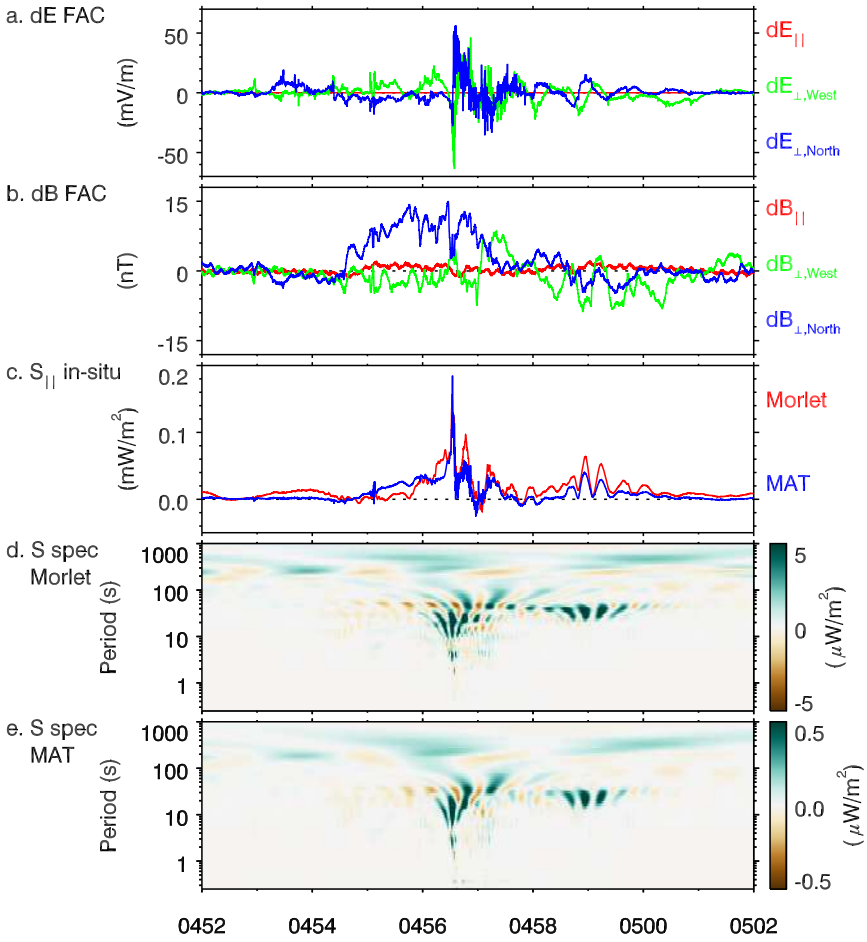

Figure B.2: Comparisons of the different methods of calculating the Poynting flux. Panel a and b show the perturbation electric and magnetic fields based by the RBSP-A measurement on June 07, 2013. Panel c shows the parallel Poynting flux calculated from the Morlet wavelet and the moving average transform. Panel d and e show the time-period spectrograms of the parallel Poynting flux from the two methods. The color range is different due to difference in normalization.

B.5 A Real-Data Example

Good agreement on Poynting flux has been reached when the Morlet wavelet and MAT are applied to the same wave electric fields. Figure B.2 shows one of our tests, where the electric and magnetic fields are measured by RBSP-A on June 07, 2013 during the main phase of a geomagnetic storm. During the event, there was a good temporal correlation between the Poynting flux enhancement and the aurora brightening. To further explore if the correlation indicates causation, it is important to determine the correct waveform of the Poynting flux, and to check whether the Poynting flux is large enough to power the aurora activities. In panel c of Figure B.2, it is clear that the waveform from the Morlet wavelet transform agrees with the moving average transform. Furthermore, panel d and e demonstrate that the time-period spectrograms from the two methods also agree. Based on the in-situ Poynting flux calculation, the earthward Poynting flux reached almost 100 mW/m^2 when mapped to the ionosphere at 100 km. This value is two orders of magnitude larger than the threshold for exiting visible aurora. Therefore the Poynting flux calculation prefers a causal relation where the aurora activities were powered by the earthward Poynting flux.

Appendix C

Auroral Arc in All-Sky Imager

The aurora images recorded by the ground All-Sky Imager (ASI) are at a much higher time resolution (3 sec) than the aurora captured by cameras on-board in-situ spacecraft like Polar and IMAGE (Frank et al., 1995; Mende et al., 2000; Burch, 2000). However, the ground aurora images are significantly distorted at small elevation angles due to the observing geometry. In this section, we describe the algorithm for correcting the distortion and its limitation.

Figure C.1 shows the geometry between the camera and the aurora arc. For now, we assume aurora has 0 height, which is a good assumption for the brightest aurora. In the end of the section, we will discuss the finite height case. As illustrated in the figure, the camera can only capture the angular diameter, as measured by the elevation. Distortion arises since the aurora altitude is concentric to the earth rather than the camera. Along the dashed curve marks the aurora altitude, the same apparent width corresponds to a much larger true width near the horizon. As discussed in Mende et al. (2008), both forward and backward projections are proposed to correct the distortion. The forward projection maps a uniform grid at the aurora altitude to the camera's CCD grid, while the backward projection does the opposite mapping. The forward projection algorithm is adopted based on the test in Mende et al. (2008) (also shown in Figure C.2).

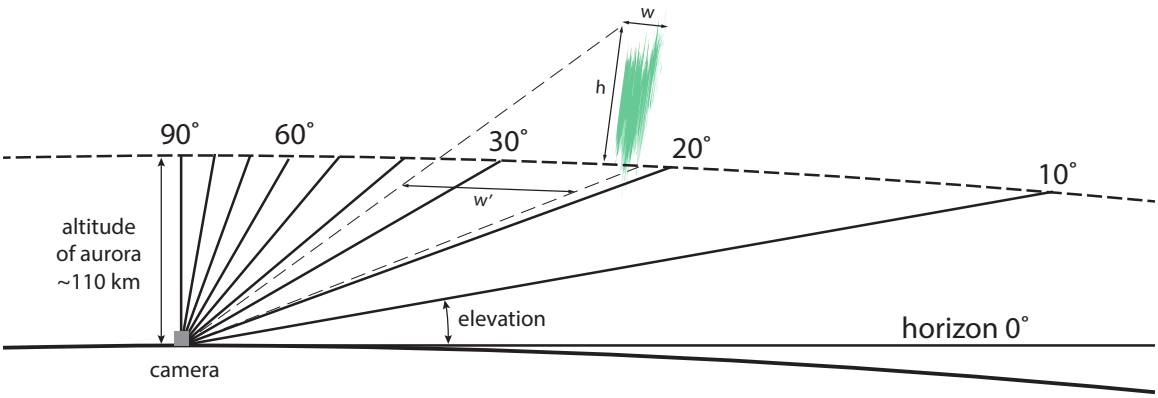

Figure C.1: Geometry between the all-sky imager and the aurora arc.

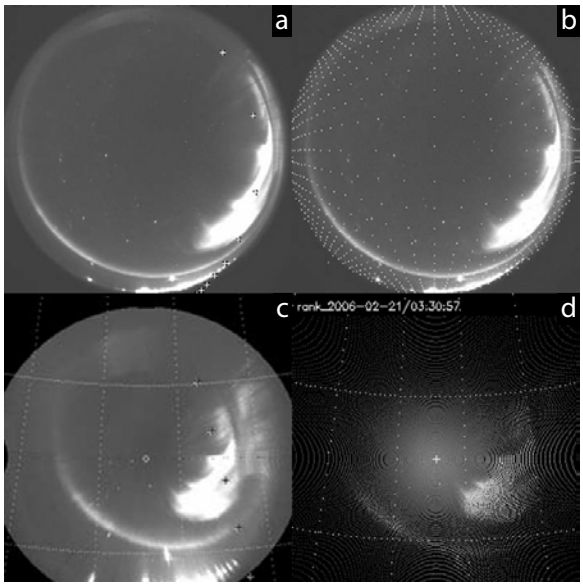

Figure C.2: The forward and backward projections, from Figure 7 and Figure 8 in Mende et al. (2008). Panel a shows an aurora image at site RANK at 2006-02-21/03:30:57 UT. Panel b over-plots the uniform grid at the aurora altitude on the aurora image (camera grid). Panel c shows the result from the forward projection, while panel d shows the backward projection. The backward projection suffers from artificial patterns.

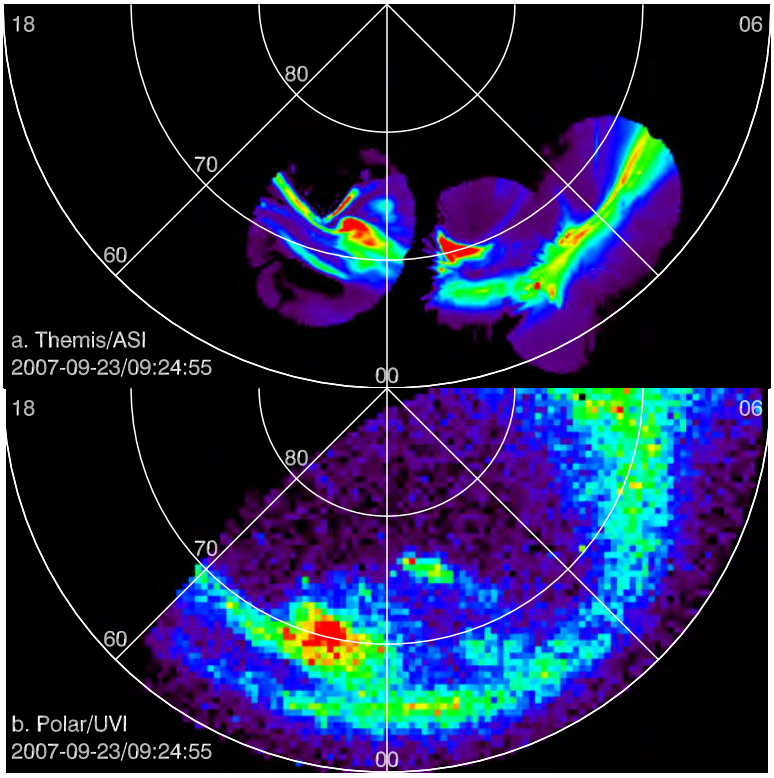

Figure C.3: Comparisons between the aurora from the THEMIS ground all-sky imager (panel a) and the Polar in-situ ultra-violet imager (panel b).

The above algorithm returns the aurora image mapped to the uniform grid at the aurora altitude (usually 110 km) in the geographical coordinate. We further convert the pixels into the plane of magnetic latitude (MLat) and magnetic local time (MLT). The MLat-MLT plane is widely used in presenting the global aurora images from in-situ cameras. Furthermore, as needed in many events, we merge the aurora images from adjacent ASI sites on the common MLat-MLT plane, based on the merging algorithm of the backward projection coded in the SPEDAS software package (`http://spedas.org/wiki/index.php?title=Main_Page`). After the re-mapping and merging, the ground aurora images are compared to spacecraft-measured aurora. The example in Figure C.3 shows that despite of the general comparable aurora forms, the ground aurora could resolve more fine structures due to its high spatial resolution.

Although the ground-based aurora imager has high time and spatial resolution, one limitation is that the finite height of aurora arc show up on the edge of the camera view (e.g. the radial rays of arcs in the bottom of panel c in Figure C.2). Figure C.1 illustrates the arc geometry: the arc has a true width w but appears to have an apparent width w' due to its finite height h. As a result, the arc is elongated towards the vanishing point, which is determined by the direction of the local dipole field. However, the arc width perpendicular to the paper is unaffected by the elongation. So far, there is no good method to fix the elongation. One possible fix is to increase the number of ground imagers, so that the edge area can be covered by nearby imagers, or to use triangulation when at least two imagers captured the same arc.